

AD _____

Award Number: W81XWH-11-1-0769

TITLE: Quantitative Analysis of Bone Microstructure Using Tomosynthesis

PRINCIPAL INVESTIGATOR: Yener N. Yeni, Ph.D.

CONTRACTING ORGANIZATION: Henry Ford Health System
DETROIT MI 4822-3450

REPORT DATE: October 2013

TYPE OF REPORT: Final

PREPARED FOR: U.S. Army Medical Research and Materiel Command
Fort Detrick, Maryland 21702-5012

DISTRIBUTION STATEMENT: Approved for Public Release;
Distribution Unlimited

The views, opinions and/or findings contained in this report are those of the author(s) and should not be construed as an official Department of the Army position, policy or decision unless so designated by other documentation.

REPORT DOCUMENTATION PAGE				Form Approved OMB No. 0704-0188	
Public reporting burden for this collection of information is estimated to average 1 hour per response, including the time for reviewing instructions, searching existing data sources, gathering and maintaining the data needed, and completing and reviewing this collection of information. Send comments regarding this burden estimate or any other aspect of this collection of information, including suggestions for reducing this burden to Department of Defense, Washington Headquarters Services, Directorate for Information Operations and Reports (0704-0188), 1215 Jefferson Davis Highway, Suite 1204, Arlington, VA 22202-4302. Respondents should be aware that notwithstanding any other provision of law, no person shall be subject to any penalty for failing to comply with a collection of information if it does not display a currently valid OMB control number. PLEASE DO NOT RETURN YOUR FORM TO THE ABOVE ADDRESS.					
1. REPORT DATE October 2013		2. REPORT TYPE Final		3. DATES COVERED 30September2011 – 29September2013	
4. TITLE AND SUBTITLE Quantitative Analysis of Bone Microstructure Using Tomosynthesis				5a. CONTRACT NUMBER	
				5b. GRANT NUMBER W81XWH-11-1-0769	
				5c. PROGRAM ELEMENT NUMBER	
6. AUTHOR(S) Yener N. Yeni E-Mail: yeni@bjc.hfh.edu				5d. PROJECT NUMBER	
				5e. TASK NUMBER	
				5f. WORK UNIT NUMBER	
7. PERFORMING ORGANIZATION NAME(S) AND ADDRESS(ES) HENRY FORD HEALTH SYSTEM 1 FORD PL ST E5F DETROIT MI 4822-3450				8. PERFORMING ORGANIZATION REPORT NUMBER	
9. SPONSORING / MONITORING AGENCY NAME(S) AND ADDRESS(ES) U.S. Army Medical Research and Materiel Command Fort Detrick, Maryland 21702-5012				10. SPONSOR/MONITOR'S ACRONYM(S)	
				11. SPONSOR/MONITOR'S REPORT NUMBER(S)	
12. DISTRIBUTION / AVAILABILITY STATEMENT Approved for Public Release; Distribution Unlimited					
13. SUPPLEMENTARY NOTES					
14. ABSTRACT <p>The purpose of the project is to determine the potential of Digital Tomosynthesis (DTS) for quantitative analysis of vertebral bone quality and for predicting vertebral bone fragility. The current scope, as a proof of concept study, is to compare parameters derived from DTS to those measured from microCT and test their ability to predict in vitro vertebral strength by a set of destructive tests on vertebrae from human cadavers. We characterized the DTS system for its ability to resolve features, shapes and densities using a number of man-made reference materials. We have noted that a single best scan is obtained in a scan direction oblique to the major orientation of the structure of interest but multiple orthogonal scans can provide complementary information. We noted that zero angle view of the scans provides density information complementary to the structural information obtained through the synthesis of all views. By correlating DTS-based parameters of cancellous microstructure (fractal dimension, lacunarity, mean intercept length and line fraction deviation) to those derived from microCT (distribution properties of bone volume fraction, trabecular thickness, number and separation, and degree of anisotropy) and to bone stiffness estimated from large scale finite element analysis, we demonstrated that parameters of cancellous bone microstructure derived from DTS correlate with those derived from microCT and increase prediction accuracy of bone stiffness over bone mass alone. The importance of analysis volume and image pre-processing were assessed and determined to be important factors in correlational models between DTS-based parameters of cancellous microstructure and microCT-based stereology and finite element parameters. Mixed multiple regression models indicated that combinations of DTS texture parameters measured at a single scanning orientation can predict vertebral fracture strength, with highest explanatory capability from images scanned perpendicular to the spine axis. As such, we produced strong evidence that DTS can not only be used to provide quantitative information on bone quality and cancellous bone microstructure, but can also contribute towards prediction of bone strength.</p>					
15. SUBJECT TERMS Vertebral fracture, digital tomosynthesis, image analysis, cancellous bone texture, microstructural heterogeneity, osteoporosis					
16. SECURITY CLASSIFICATION OF:			17. LIMITATION OF ABSTRACT	18. NUMBER OF PAGES	19a. NAME OF RESPONSIBLE PERSON
a. REPORT U	b. ABSTRACT U	c. THIS PAGE U			19b. TELEPHONE NUMBER (include area code)
			UU	81	

TABLE OF CONTENTS

	<u>Page</u>
Introduction.....	4
Body.....	4
Key Research Accomplishments.....	48
Reportable Outcomes.....	49
Conclusion.....	51
References.....	51
Appendices.....	53

INTRODUCTION

Accuracy in the prediction of osteoporotic fracture risk using bone mineral density alone is limited. Experiments using microcomputed tomography (μ CT), a laboratory scale imaging device, on cadaver bones show that parameters that quantify the heterogeneity of the cancellous bone microstructure are especially useful for predicting vertebral strength. However, measurement of bone microstructure in a clinical setting is difficult and, when possible, is generally limited to easily accessible extremities. Digital tomosynthesis (DTS) is a clinically available imaging technique that can produce multiple planar images of an object with high resolution, as if the object was physically sliced before imaging. The objective of the current project is to determine the potential of DTS for quantitative analysis of vertebral bone quality and for predicting vertebral bone fragility. As a part of this evaluation, parameters derived from DTS are compared to those measured from μ CT and their ability to predict in vitro vertebral strength is examined by a set of destructive tests on vertebrae from human cadavers. Methods of fractal, lacunarity, mean intercept length and line fraction deviation analyses are used to quantify cancellous microstructure from DTS images. The strength of the vertebrae will be measured using a loading mode that will generate a wedge-shaped fracture as seen in clinical vertebral fractures. If DTS provides structural information sufficiently detailed compared to the μ CT gold standard or that significantly correlates with the strength, the development of this concept into a clinical screening process will be pursued through further refining and testing.

BODY

Task 1. *Retrieval of 20 cadaveric human fresh-frozen thoraco-lumbar vertebrae from tissue banks and body donation programs (Months 1-4):*

1a. Review and activation of tissue collection protocols by the donation program (Months 1-2).

1b. Collection and shipment of the vertebrae (Months 2-4)

Approval of the institutional review board (IRB 6688) for the project was obtained and submitted to the USAMRMC Office of Research Protections (ORP), Human Research Protection Office (HRPO) for review along with a claim of exemption from review to use preexisting cadaveric vertebrae. The statement that the project may proceed with no further requirement for review by the HRPO was received prior to the beginning of the supported period. In accordance with this notification (HRPO Log Number A-16751), newly retrieved vertebrae as well as previously existing deidentified cadaveric vertebrae are used.

We identified 40 fresh-frozen thoraco-lumbar vertebrae from 10 subjects previously collected through approved protocols and allocated them to the project. In addition, we established tissue collection protocols with the National Disease Research Interchange (NDRI), the Anatomical Donations Program of the University of Michigan and Platinum Training. Seven spines were supplied by NDRI and nine by Platinum Training (total 16 new spines).

Vertebrae were separated from spines, stripped of surrounding soft tissue, and posterior elements were resected flush with the posterior aspect of the vertebral body. Following preparation, vertebral bodies were wrapped in saline-soaked towels and preserved at -20 degrees Celsius until scanning and mechanical testing were performed.

This task is complete.

Task 2. *Refinement of Digital Tomosynthesis (DTS) scan parameters (Months 1-4):*

2a. In order to have reference materials that resemble cancellous bone but with estimated properties, prepare wire-mesh references with a wire thickness of 50 μ m and varying mesh density with wire separation in the order of 1mm and varying out-of-plane separation. (Month 1)

2b. Perform a series of DTS scans on these references using variations of tube angle, number of projection images, number of reconstructed planes and the incident exposure for each projection. (Months 1-3)

2c. Perform μ CT on reference materials. (Months 1-3)

2d. Determine scan parameters that produce the best agreement between μ CT and DTS. (Month 4)

In order to refine DTS scanning parameters, custom phantoms were created to assess the accuracy of DTS in resolution of separation, thickness, distances, in-plane and out-of-plane geometric distortion, and density linearity.

To assess the minimum spacing which may be resolved by DTS, six phantoms were created comprised of equally spaced stacked squares of radiopaque aluminum and radiolucent acrylic at 350, 300, 250, 200, 150, and 100 μm nominal spacing, as measured by micrometer during phantom preparation (Figure 1a). The squares were clamped and bound at the edges using epoxy to create a solid construct. The resulting cross-sectional banding pattern thickness and frequency is comparable to human trabecular bone. To assess the minimum thickness which may be resolved by DTS, another set of six phantoms was created with thin radiopaque aluminum layers (nominally 25, 60, 75, 90, 115 and 120 μm as manually measured from μCT images) bound between thick (1.5 mm) layers of radiolucent acrylic (Figure 1b).

Density linearity phantoms were created using serial dilutions of 28.2% (282 mg/ml) organically bound iodine in the form of iohalamate meglumine, an ionic contrast agent. Nominal concentrations of 282, 141, 70.5, 35.25, 17.63, and 8.81 mg/ml organically bound iodine, as well as air and water, were placed in a sealed well plate (Figure 1c).

For demonstration of anisotropic and edge-enhanced characteristics of DTS, a nylon sphere (Figure 1d) and cylinder (Figure 1e) were included in the phantom tray. To aid in measuring true voxel size in the reconstructed volume, a geometric accuracy phantom was created using four 1 mm beads, placed in four corners at 35 mm apart (Figure 1f). An embedded human vertebra was also included in the phantom as a realistic reference material (Figure 1g).

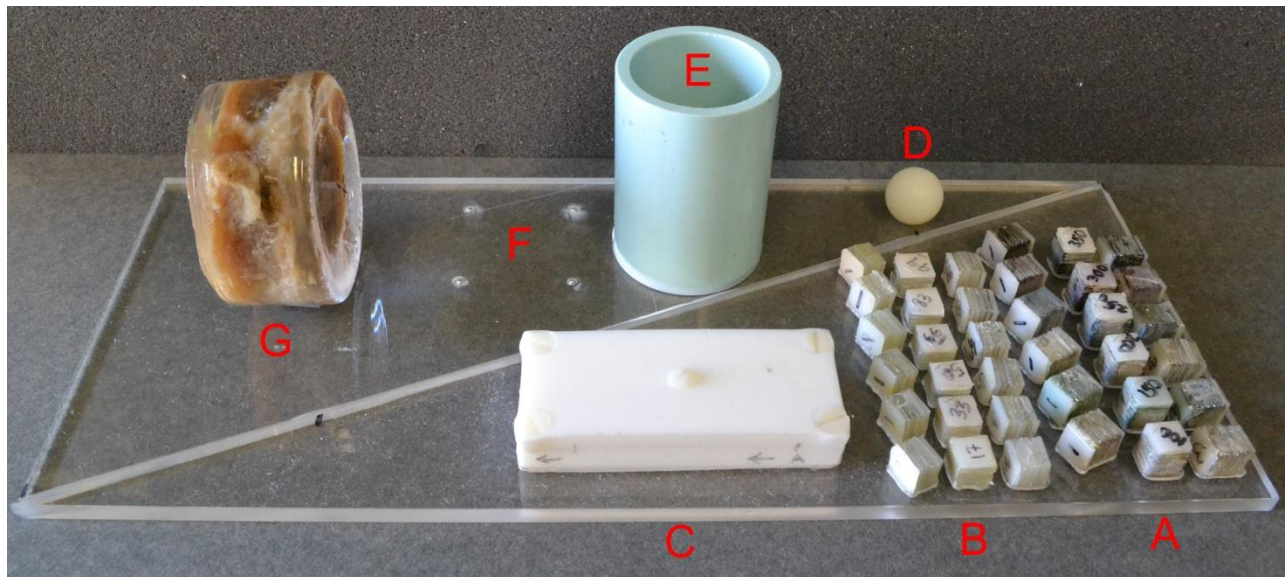


Figure 1: Tray of phantoms to assess DTS resolution, geometric distortion, and density linearity.

An aluminum grid panel with hollow evenly spaced cells with known dimensions (12.7 x 12.7 x 12.7 mm, Figure 2) was used to examine geometric distortion and uneven signal distribution within the reconstructed DTS images.

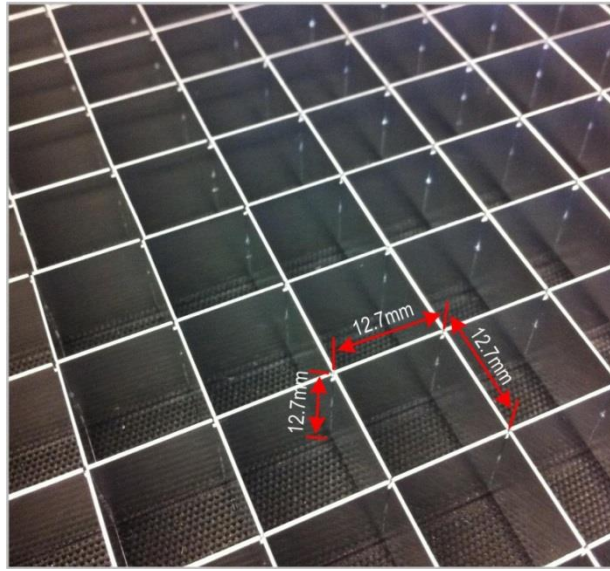


Figure 2: Aluminum grid panel phantom to assess geometric distortion in x, y and z directions.

Density linearity phantoms

In each of 5 scanning sessions, DTS scans and planar digital radiographs were performed on the sealed wells containing serial dilutions of iodine solution. As DTS scans were performed with the phantom tray oriented in 3 directions, the density phantoms were scanned a total of 3 times per session, allowing assessment of session-to-session variability as well as within-session variability. A single radiograph was taken in each session.

Images were inverted for white on black presentation, and a cylindrical selection was drawn at the center of each well. Average gray value was measured for each well at a single orientation for each session. Only the central 8 mm of each well was analyzed to avoid a darker region of edge enhancement at the perimeter of each 10 mm diameter well, which is due to a high-pass filter applied in the direction of tomographic acquisition. To assess within-session variability, measurements were repeated at three orientations per session. Radiographs were similarly analyzed by recording average gray values within an 8 mm circle for each well.

Spacing phantoms

Spacing phantoms were scanned using μ CT and reconstructed at 22 μ m isotropic voxel size. These images were cropped to include only the phantom, and were resliced to expose a central cross section representing the phantom's banding pattern. DTS scans were performed on the phantom tray oriented in 3 directions: parallel, perpendicular, and at 22.5° oblique to the scanning direction (Figure 3). As there were 2 sets of spacing phantoms (oriented in line and at 22.5° to length of the tray) for in-plane assessment, the 3 scanning directions allowed the phantoms to be scanned a total of 4 different angles relative to the scanning direction (0°, 22.5°, 67.5° and 90° to the scanning direction).

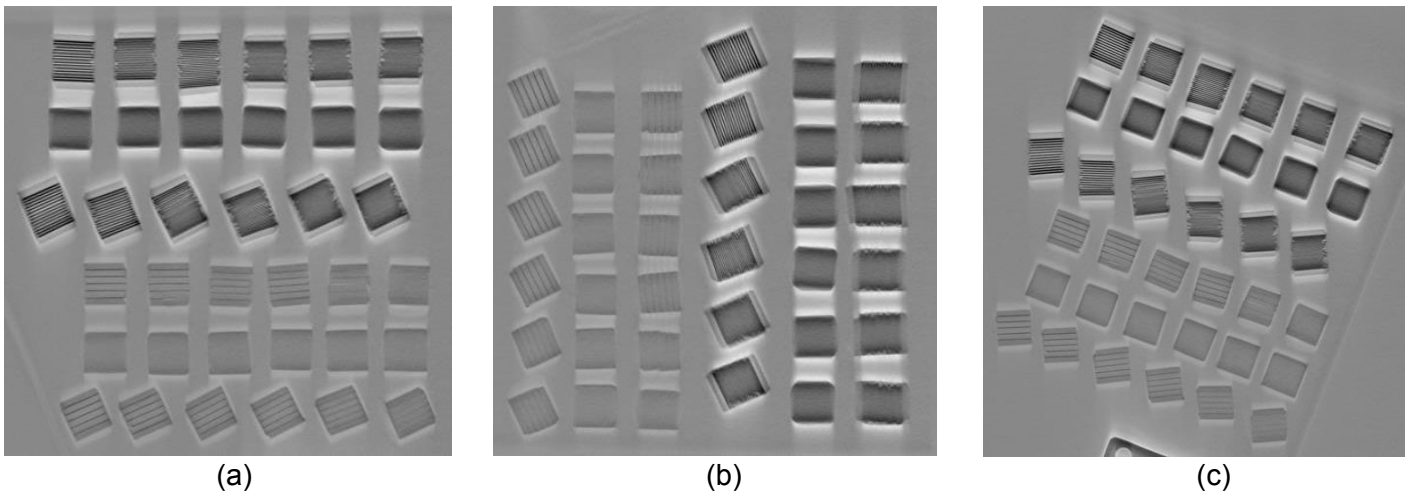


Figure 3: DTS reconstructions of spacing and thickness phantoms oriented parallel (a), perpendicular (b), and 22.5° (c) to the scanning direction

Visual Analysis of DTS Spacing Phantom Images

DTS images of spacing phantoms were visually assessed for presence of a banding pattern. A central cross-sectional slice from each phantom was viewed at 200% magnification with display range set to the full pixel value range of the image.

Quantitative Analysis of Microcomputed Tomography and DTS Spacing Phantom Images

A vertical line with thickness of approximately 2 mm was drawn between the top aluminum layer and the bottom aluminum layer (Figure 4). A mild median filter with a kernel of 2 was applied to the image to reduce noise. A gray value profile was plotted along the vertical line, which was processed using a Fast Fourier Transform (FFT) to assess frequency of the banding pattern.

The resulting frequency-domain plot was assessed to identify maximum peaks representing frequency magnitude of the banding pattern. Average layer thickness was calculated as $0.5 \times (1/\text{frequency})$ at the maximum peak. The peak location and thickness was considered a gold standard by which to compare subsequent analyses of DTS images. The same procedure was performed on DTS phantom scans from a single, randomly-chosen scanning session.

Textural information was visually present in phantoms 250 μm and below which was not identified in FFT analysis, so mean intercept length (MIL) and line fraction deviation (LFD) analyses were performed. A single cross-section from the six phantoms at the 0° angle was cropped from the DTS reconstruction. MIL and LFD analyses were performed using a custom MATLAB script (Sander and Barocas, 2009). From MIL analysis, maximum MIL (MIL.Max) and its angle (MIL.MaxAngle) were recorded, as well as average MIL (MIL.Av), degree of MIL anisotropy (ratio of maximum to minimum MIL, MIL.DA), and standard deviation of MIL (MIL.SD). From LFD analysis, maximum LFD (LFD.Max) and its angle (LFD.MaxAngle), minimum LFD (LFD.Min), average LFD (LFD.Av), degree of LFD anisotropy (ratio of maximum to minimum LFD, LFD.DA), and standard deviation of LFD (LFD.SD) were recorded. In addition, similar parameters were recorded when an ellipse was fit to LFD measurements (LFD.EllipseMax, LFD.EllipseMin, and LFD.EllipseMaxAngle). LFD and MIL parameters allow quantification of pattern directionality in the phantom images. LFD is typically more sensitive to anisotropy than MIL, as the method calculates the fraction of bright pixels in a grayscale image along many closely packed lines at various angles, rather than counting intersections at various angles in a binarized image (Geraets, 1998).

Fractal dimension and lacunarity were calculated from the same images using FracLac (Karperien, 2007). The box counting method (Fazzalari and Parkinson, 1996; Plotnick et al., 1996) was used to assess fractal dimension, a measure of image complexity which uses the difference between maximum and minimum gray values to describe how a pattern's details change with scale. Lacunarity, a measure of translational invariance, was also calculated. Both methods work together to characterize the existence of patterns within an image.

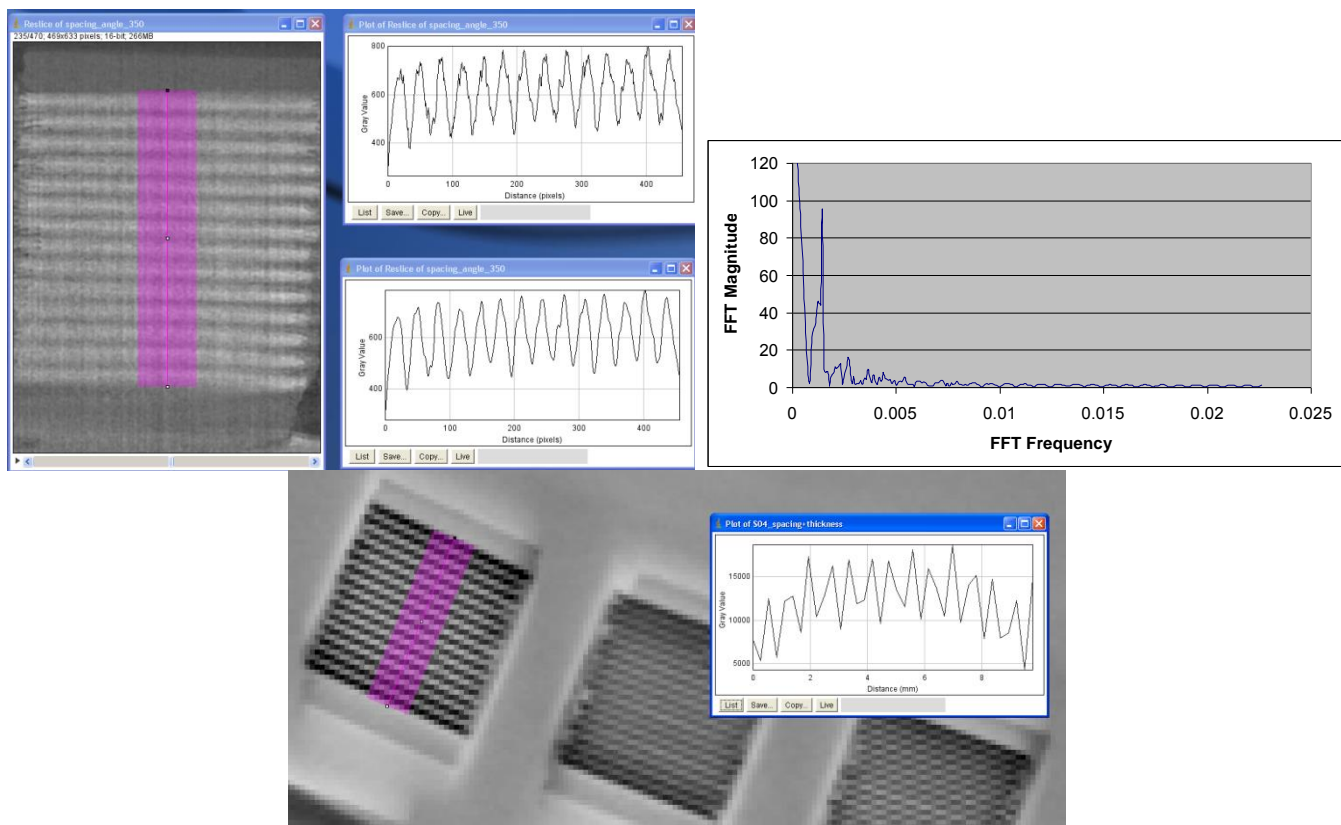


Figure 4: Creating line profile for Fast Fourier Transform from filtered μ CT reconstruction (upper left). In the above plot, a peak was identified at 351.23 μ m (upper right). The same procedure was repeated for DTS images (bottom center).

Thickness Phantoms

Thickness phantoms were scanned using microcomputed tomography and reconstructed at 10 μ m isotropic voxel size. These images were cropped to include only the phantom, and were resliced to expose a central cross section representing the phantom's banding pattern. The two sets of in-plane thickness phantoms (oriented in line and at 22.5° to length of the tray) were also DTS scanned in three orientations as described above, yielding 4 different angles relative to the scanning direction (0°, 22.5°, 67.5° and 90°; Figure 3).

Visual Analysis of DTS Thickness Phantom Images

DTS images of thickness phantoms were visually assessed for presence of aluminum layers separated by plastic. A central cross-sectional slice from each phantom was viewed at 200% magnification with display range set to the full pixel value range of the image.

Quantitative Analysis of Microcomputed Tomography and DTS Thickness Phantom Images

The same FFT, morphometric and textural analyses as previously described were performed on μ CT and DTS images of the thickness phantoms.

Aluminum grid panel phantom

The aluminum grid panel was scanned in four angular orientations relative to the scanning direction (Figure 5; 0°, 15°, 22.5° and 45°). Each scan generated a stack of 11 reconstructed image slices with 1 mm spacing between each slice. Two rectangular regions of interest (ROI: L1 and L2) with 500 pixel width and maximum length allowable within each the DTS image were analyzed for the gray value profiles, covering approximately 60-70% of examined image area.

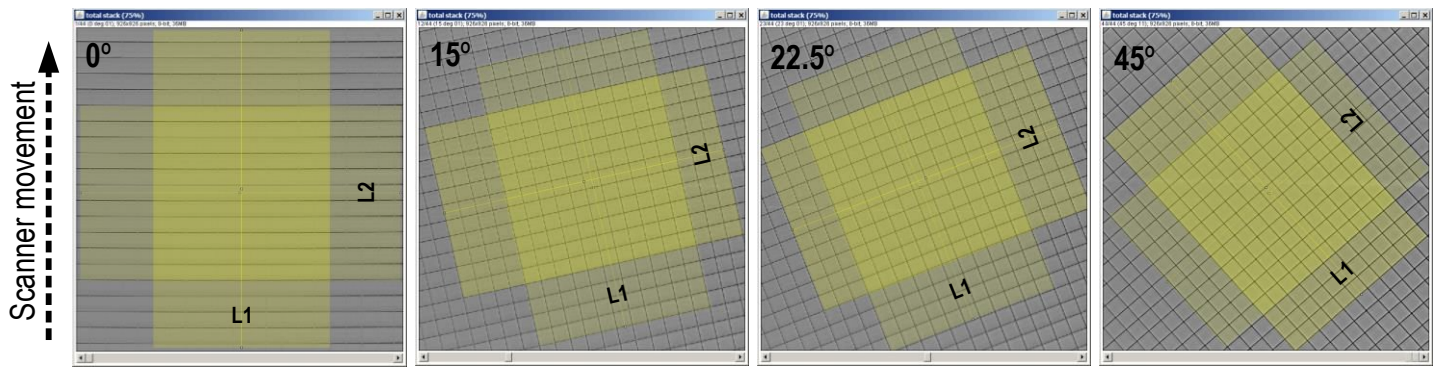


Figure 5: Aluminum grid panel was imaged at four angular orientations (0°, 15°, 22.5° and 45°) respective to the scanning movement. Each angular orientation constituted of 11 DTS slices that were spaced 1 mm between slices. The gray value profile of each image slice was measured at two principal orientations L1 and L2 (yellow boxes).

This task is complete.

Task 3. Microcomputed tomography (μ CT) (Months 5-6):

3a. Microcomputed tomography scanning/reconstruction of individual vertebral bodies at 30 micrometer voxelsize using a calibrated radiographic reference. (Month 5)

3c. Preparation of regions of interest, segmentation and quantification of average and standard deviation of conventional micro-CT parameters using specialized CT-analyzer software: bone volume fraction, bone surface to volume ratio, trabecular number, thickness and separation, structure model index, connectivity and anisotropy. (Month 5)

3d. Preparation of regions of interest and calculation of fractal dimensions and lacunarity. (Months 5-6)

3e. Preparation of regions of interest, segmentation and calculation of line fraction deviation. (Month 6)

We have previously noted that calculations of microstructural properties are affected by the voxel size used in μ CT scanning and image reconstruction (Kim et al., 2004). The maximum resolution that can be achieved during a μ CT scan is affected by the size of the object; larger vertebrae allow for larger minimum voxel size (resulting in lower resolution). In order to avoid a potential confounding effect of vertebral size (through voxel size) on calculated parameters, we determined a minimum voxel size that can be used for all vertebrae in the study by measuring vertebral dimensions of the actual specimens, either on the specimen using a caliper or on images captured from pilot μ CT views. We determined for the first 40 vertebrae (T6, T8, T11 and L3 vertebrae from 5 female and 5 male cadavers; Age 63-90 years) that 45 micrometers is the minimum voxelsize that can be used for all the samples. Large scale finite element models of cancellous bone based on μ CT images with 50 micrometer voxelsize achieved good agreement with experimentally measured stiffness in previous work (Hou et al., 1998) indicating that the cancellous microstructure of vertebral bone is sufficiently resolved at this resolution.

The in-house μ CT system used in the project is built on the principles of an earlier in-house system previously described in detail (Reimann et al., 1997). The presently operating system uses a Kevex 16-watt x-ray source with a 9-micron focal spot, a 1888x1408-pixel Varian PaxScan 2520 flat panel digital x-ray detector with 127-micron pitch, a Newport precision rotational stage, and control software running under Windows XP. Each vertebra was placed in a radiolucent tube, sealed prior to scans, and scanned using our in-house μ CT system at a voxel size of 45 μ m. In each reconstruction of whole vertebral body, the largest possible cubical volume of interest (VOI) consisting only the cancellous bone was digitally cut out using ImageJ (NIH, USA). The bone and non-bone phases were segmented using Microview (v2.0, GE Healthcare, Little Chalfont, UK), which is based on standard global thresholding procedures previously described and widely used (Kuhn et al., 1990; Hou et al., 1998; Yeni and Fyhrie, 2001).

For analysis of the microstructure, the segmented images were binarized. The analysis was carried out using both custom-written software (Goulet et al., 1994; Yeni et al., 2011) and commercial software (CT Analyzer, Skyscan, Kontich, Belgium). The intra-specimen mean (A_v) and standard deviation (SD) of the following microstructural properties were calculated from each binarized VOI using stereologic methods: Bone volume fraction (BV/TV), bone surface to volume ratio (BS/BV) trabecular thickness (Tb.Th), trabecular number (Tb.N) and trabecular separation (Tb.Sp). Degree of anisotropy (DA) was also calculated using the 3D Secants, configuration and star volume methods. The A_v and SD were recorded as measures of intraspecimen magnitude

and heterogeneity, respectively, of a given parameter. Connectivity, structure model index and fractal dimension parameters were calculated using CT Analyzer among other properties of the microstructure.

We have automated LFD, MIL, and fractal measurement and are able to batch-process image sets for this analysis. We can not only analyze selected sections from the image as was originally planned but can also process an entire series of slices within a single μ CT volume. Using this approach, we performed LFD, MIL and fractal analyses using volumes of μ CT images matched for both thickness and location to the DTS slice (see Task 4).

The work described thus far fulfills the scope of the statement of work.

In addition to the analyses of microstructure, we performed finite element simulations on each of the cancellous bone volumes, in order to estimate cancellous bone stiffness and trabecular stress distribution properties. This was to obtain Young's modulus (E_{FEM}), coefficient of variation of von Mises stress distribution (VMCV) and average trabecular von Mises stress per apparent uniaxial stress (VM_{Exp}/σ_{app}) in the cancellous bone, and later to build multi regression models with DTS parameters to assess prediction capability of the DTS system. Linear elastic FE models with isotropic element properties were prepared using a custom-written meshing algorithm as in previous studies (Yeni et al., 2005). Young's modulus of each bone element was assigned using an approach similar to that used by Nekkanty et al. (Nekkanty et al., 2010) resulting in the relationship:

$$E_{tissue} \text{ (MPa)} = (8020/1130.257) GL_{element}$$

where $GL_{element}$ is the gray-level of the element and 1130.257 is the gray level corresponding to a mineral density of 1.223g/cm^3 . All elements were assigned a Poisson's ratio of 0.3. Uniaxial compression was simulated by using a displacement equivalent to an apparent strain of 0.005. The models were displaced in the superoinferior direction while the displacements in other directions were not constrained (Free-end conditions). The models were solved using a custom-written element-by-element pre-conjugated gradient solver as in previous studies (Hou et al., 1998; Yeni et al., 2005). Apparent modulus of cancellous bone was calculated using nodal reaction forces, the apparent surface area of the sample and the input apparent strain. The average and standard deviation of trabecular von Mises stress were calculated for the entire sample.

This task is complete.

Task 4. Digital Tomosynthesis (DTS) of vertebrae (Months 7-9):

4a. DTS scanning of vertebral bodies using the SonialVision Safire II system (Shimadzu Co., Kyoto, Japan), with the superoinferior axis as the axis of image rotation. Scans with the coronal and sagittal views centered at zero degree angle will be obtained. (Month 7)

4b. Preparation of regions of interest and calculation of fractal dimensions and lacunarity. (Months 7-8)

4c. Preparation of regions of interest, segmentation and calculation of line fraction deviation. (Month 8)

Using the Shimadzu Sonialvision Safire II tomosynthesis system (Shimadzu, Kyoto), 74 radiographic tomosynthesis images were captured over 2.5 seconds at 65 kV and 250A and then reconstructed with image slice thickness of 1 mm.

We conducted our study in two phases to fully explore the potential of DTS in predicting fracture strength of vertebral bones. The first phase was conducted as a preliminary study to test the feasibility of MIL, LFD and fractal analyses on DTS images and to identify which parameters from these analyses would be informative in predicting cancellous bone stiffness obtained from μ CT-based finite element analysis. In phase 1, imaging parameters were established and image pre-processing techniques were examined.

In the phase 2 of the study, with an enhanced understanding of which DTS parameters are informative in stiffness prediction, we then investigated the effect of scanning orientation and 3D analysis of DTS slices predicting both μ CT stereological parameters and mechanical fracture strength of the 40 vertebral bones.

Phase 1

In phase 1, T6, T8, T11, and L3 vertebral bodies were scanned in thin-walled plastic cylinders, aligned and separated using radiolucent foam. The cylinders were scanned transverse to the axis of the spine with the cylinders aligned such that reconstructed slices represented the anterior-posterior (AP) anatomic direction. A single coronal image from each bone was selected for analysis. The images were then processed with three different image processing methods (Figure 6) in an effort to enhance extraction of trabecular structures within the image texture. Three types of processing methods were examined:

- i) USM - unsharp mask (USM) filter sharpened without binarization (i.e., grayscale)
- ii) Bin.Csv – conservative binarization by use of weak convolution and high pass filters
- iii) Bin.Ag - aggressive binarization by use of strong convolution and high pass filters

The filtering processes were performed using Photoshop (Adobe Systems Inc, San Jose, California) and ImageJ (NIH, Bethesda, Maryland). However fractal analysis was performed on images with no pre-processing.

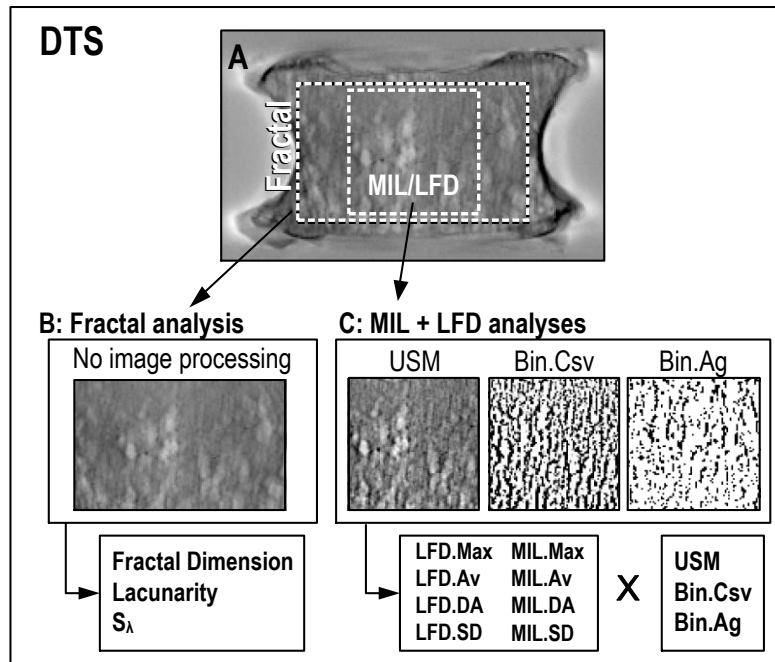


Figure 6: A) A typical DTS image segment used for the analyses. There were two types of ROI; B) Fractal dimension, lacunarity and S_λ were calculated through fractal analysis without image pre-processing. C) MIL and LFD parameters (Max, DA, Av and SD of MIL and LFD) were calculated for each of the three types of image pre-processing methods (USM, Bin.Csv and Bin.Ag).

Fractal analysis – Using box count fractal analysis method (Fazzalari and Parkinson, 1996; Plotnick et al., 1996), fractal dimension (FD) and mean lacunarity (λ) were obtained by use of FracLac 2.5 plugin (Karperien, 2007) of ImageJ (NIH, Maryland). The box count method uses a series of sequentially reducing box size grids on the image to sample the local difference between the maximum and minimum gray values in each box region. As a secondary derivative measure of lacunarity, a slope of lacunarity against box size value was also calculated (S_λ).

MIL and LFD analyses – We have performed both MIL and LFD analyses using custom MATLAB codes (Mathworks, MA), calculating MIL and LFD values for each 1 degree increment over 360 degrees (Sander and Barocas, 2009). The MIL and LFD values were polar plotted (Figure 7) and mean (Av), standard deviation (SD), maximum (Max) and degree of anisotropy (DA) of MIL and LFD were obtained for each DTS image.

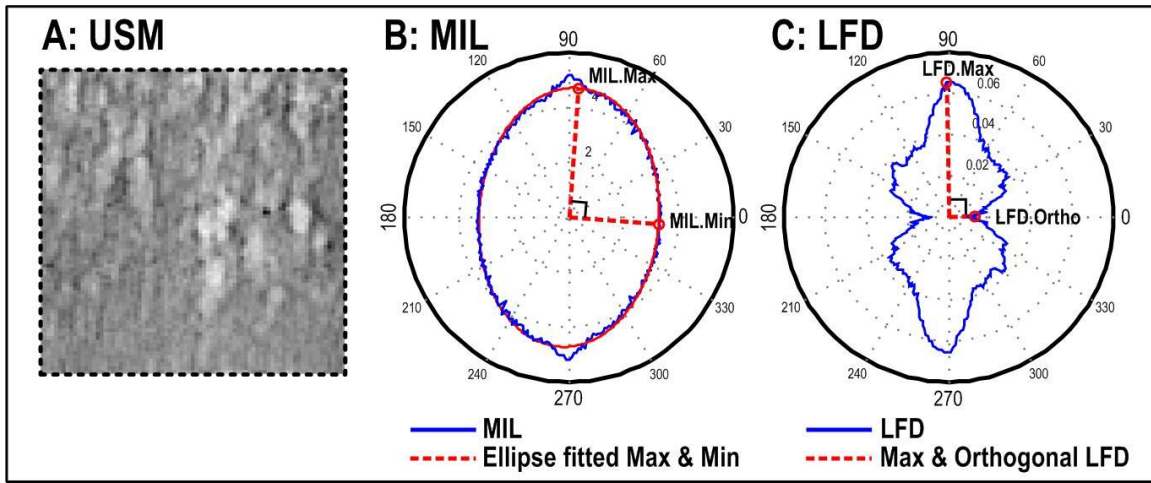


Figure 7: A) An example of a DTS image that generated polar plots of B) MIL (mean intercept length) and C) LFD (line fraction deviation). Note how overall orientations of the polar plots correspond to that of the trabecular texture in (A). Dotted red lines represent the principal components in MIL and LFD. The degree of anisotropy (DA) was calculated from the ratio of maximum to secondary principal component where MIL.DA was from MIL.Max/MIL.Min and LFD.DA was from LFD.Max/LFD.Ortho.

In order to further understand LFD, MIL and fractal parameters, we subjected a single DTS slice (1 mm thick) and 20 corresponding μ CT slices (each 0.045 mm thick) – the regions matched for both thickness and location – to LFD, MIL and fractal analyses (Figure 8) and constructed pair-wise mixed regressions.

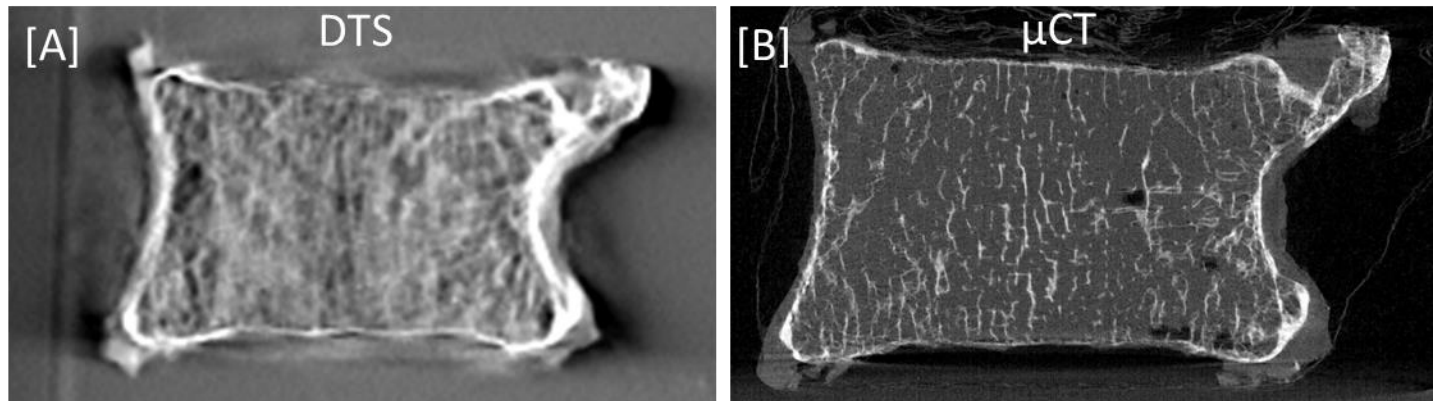


Figure 8: DTS slice (a) and μ CT stack of equivalent thickness (b) were analyzed for MIL, LFD and fractal parameters and then DTS and μ CT generated parameters were compared. DTS image has been inverted for white bone presentation.

The work described thus far fulfills the scope of the statement of work.

During this phase, we developed the capability to automatically batch-process a large number of images which allows us to analyze multiple slices of a single DTS reconstruction. In analyzing the first set of images, it became apparent that the resolution of trabecular structure is highly directionally dependent in DTS imaging. It was also found that image pre-processing does not conclusively enhance correlation between μ CT stereology parameters and DTS texture parameters and was therefore not used in future studies. With the knowledge gained from phase 1, we were posed to better address the research topic.

Phase 2

With the better understanding of which DTS parameters are potentially informative in predicting cancellous bone finite element stiffness from phase 1 of the study, we rescanned the same 40 vertebral bones but this time in six different configurations (Figure 10); in coronal (AP – anterior posterior) and sagittal (LM – lateral medial) views at three different angles to the spinal axis (par, ang, perp - 0°, 22.5° and 90°) so as to understand which view and orientation would provide best prediction in fracture strength.

Precision in specimen positioning was considered an issue in phase 1, so specimens were mounted and consistently aligned in a custom radiolucent scanning tank filled with 0.9% saline (Figure 11). Alignment was

ensured using a radiolucent clamping system.

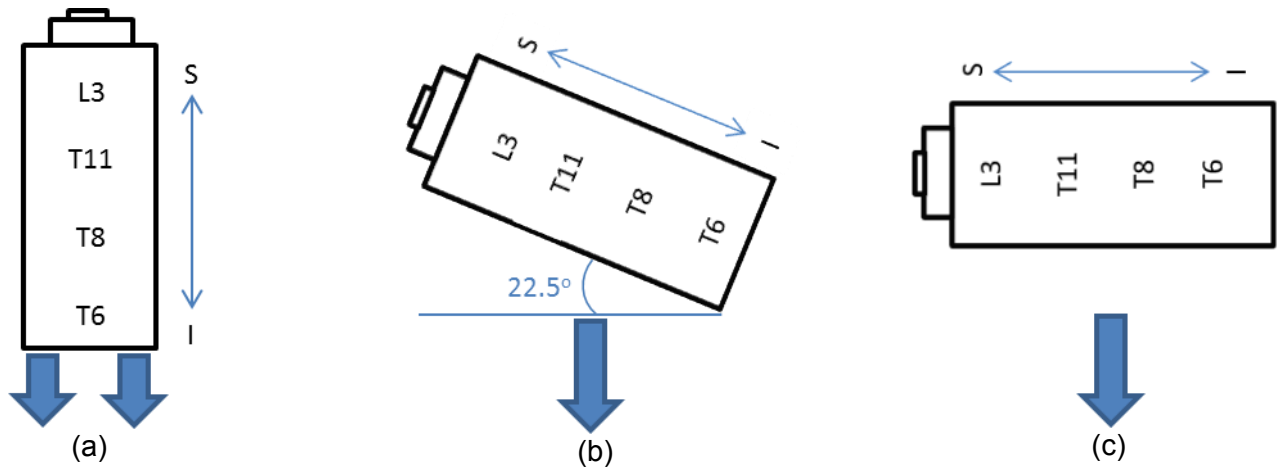
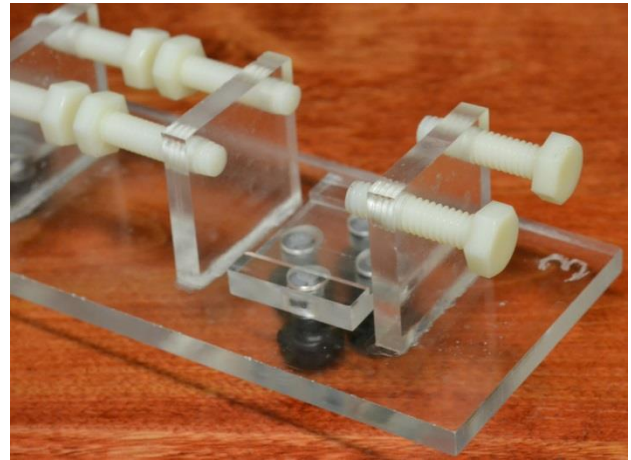


Figure 10: Vertebrae were scanned at six orientations in total, parallel (a), oblique (b), and perpendicular (c) to the superoinferior axis of the spine, in both AP (anterior-posterior) and LM (lateral-medial) views. Superior/inferior (S/I) orientation was aligned with respect to the scanning direction (indicated by large arrows).



(a)



(b)

Figure 11: Specimens were mounted on trays inside custom-built radiolucent tanks, allowing for precise specimen positioning and orientation with respect to image axes (a). Consistent AP/LM alignment and transverse tilt correction was achieved via rotation on a tray-mounted clamping system within each box (b).

Matching cuboidal VOIs were prepared from both μ CT and DTS reconstructions. The DTS volume was analyzed on a slice-by-slice basis for texture parameters (LDF, MIL, and fractal) and the μ CT volume was analyzed for stereology parameters. A description of the measured parameters and nomenclature are described in **Figure 12**. Mixed regressions were used to compare DTS (LFD, MIL and fractal) parameters to μ CT stereology parameters.

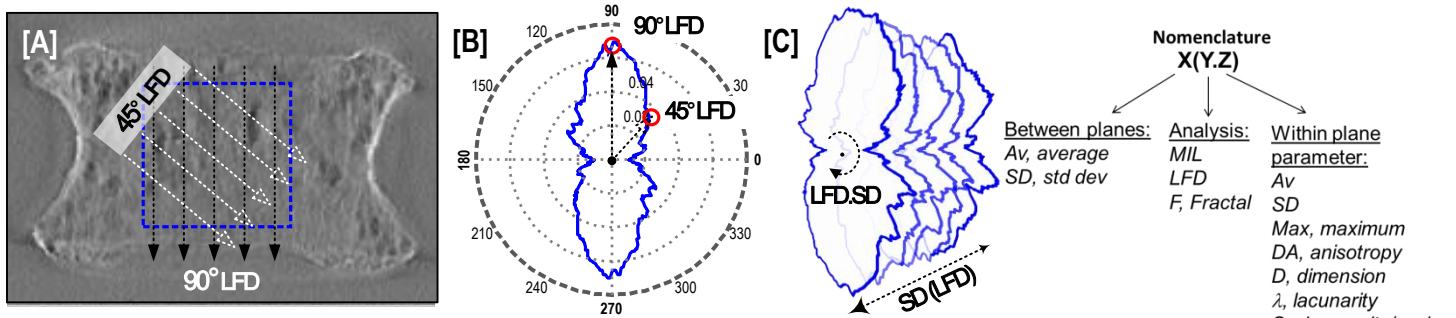


Figure 12: (A) A square region cropped out of the DTS image is analyzed using the fractal, MIL and LFD analysis methods. MIL and LFD are calculated in all directions in the image. (B) A typical polar plot representation of the LFD data, from which an average, standard deviation, max and anisotropy (LFD at 90° / LFD at 0°) can be calculated for each slice. (C) Each slice in the stack is analyzed. Stack average and standard deviation (e.g. SD (LFD.SD)) are calculated as measures of 3D microstructure within the bone.

Additionally we have measured approximate vertebral height and width using the central slices from AP-transverse and LM-transverse (corresponding to coronal and sagittal views - Figure 13)

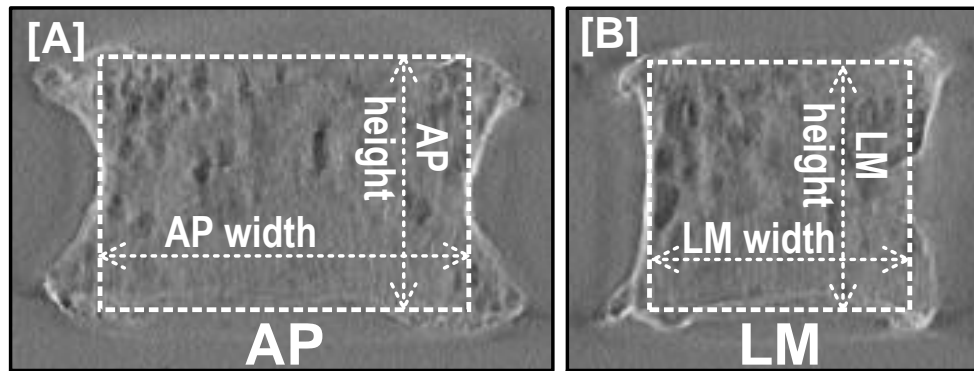


Figure 13: A central slice from (a) anterior-posterior (AP) coronal and (b) lateral-medial (LM) sagittal scans was used to measure waist-to-waist width and endplate-to-endplate height.

In phase 2, we also investigated three methods of ROI/VOI selection (Figure 14) to determine if increasing analysis volume would improve the prediction performance. The three methods were (A) using a single largest possible ROI from AP and LM mid-plane (a single 2D image), (B) multiple slice VOI with constant dimension square within each slice and (C) multiple slice VOI with largest possible square ROI in each given slice resulting in a varying cross-sectional ROI area across the stack. At the end of phase 2, we constructed both mixed regression models predicting peak fracture forces of the 40 vertebrae from wedge compression tests.

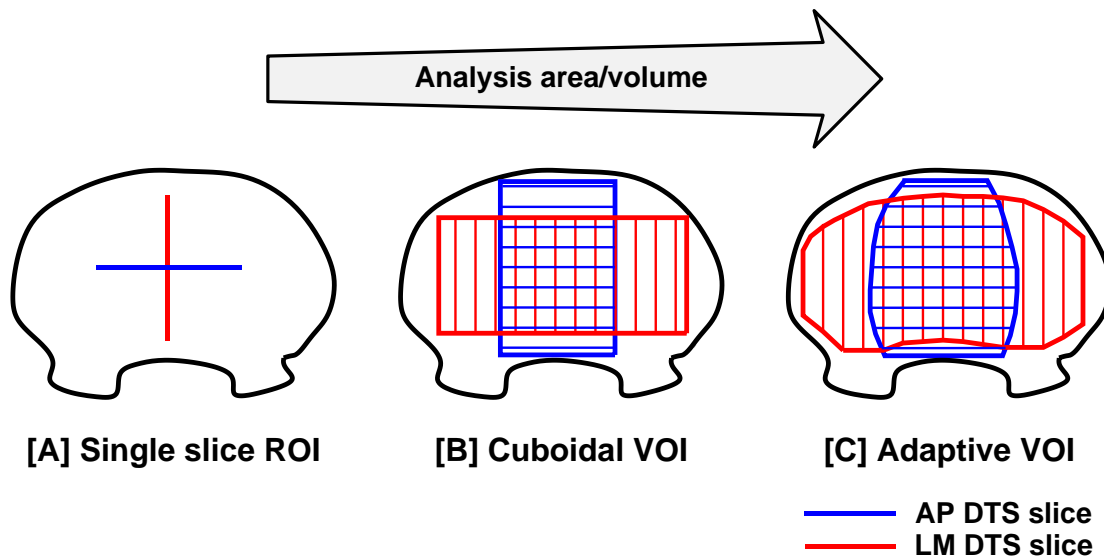


Figure 14: Three ROI methods in selecting DTS images for analysis. (A) single largest possible ROI from AP and LM mid-plane, (B) VOI with constant dimension or (C) VOI with largest square ROI per slice.

This task is complete.

Task 5. Mechanical testing of vertebral bodies (Months 10-11)

5a. Non-uniform compression testing of vertebral bodies using a materials test machine (8501M, Instron Inc., MA). Determine vertebral strength as the maximum load during fracture. (Months 10-11)

5b. Reduction of mechanical test data. (Month 11)

Preliminary wedge loader model

The mechanical testing fixture and protocol were designed to apply non-uniform loading conditions to the specimen vertebral bodies. Specifically, the non-uniform loading would consist of uniaxial compression and a bending moment, which would simulate the loads producing a wedge fracture, often a result of heavy weight lifting. The objective of the design and protocol was to allow independent control of the compressive load and the bending moment. Previous researchers achieved combined loading via wedged load platens (McDonnell et al., 2010), multi-arm hydraulic systems (Whealan et al., 2000), and robotic arm (Buckley et al., 2007). We produce the requisite loading via an axial and rotary actuator. The axial actuator control applies the compressive loading condition while the rotary actuator control applies the bending loading.

During the study period, we started by designing and fabricating a prototype combined loading fixture to prove out the concept – Figure 15 is a conceptual design rendering of the prototype. The upper load applicator has an inclined surface which, when rotated, directs one of the load transfer rods downward and the other upward. This rotates the combined loading platen and imparts bending to the specimen mounted to the specimen mount. Axial displacement of the load applicator directs both load transfer rods downward simultaneously and imparts specimen compression. Testing during the prototype trials consisted of applying compression, bending, and combined compression and bending to a foam test block to evaluate the combined loading fixture operation. The combined loading of the test foam blocks produced a linear load response (Figures 16-19).

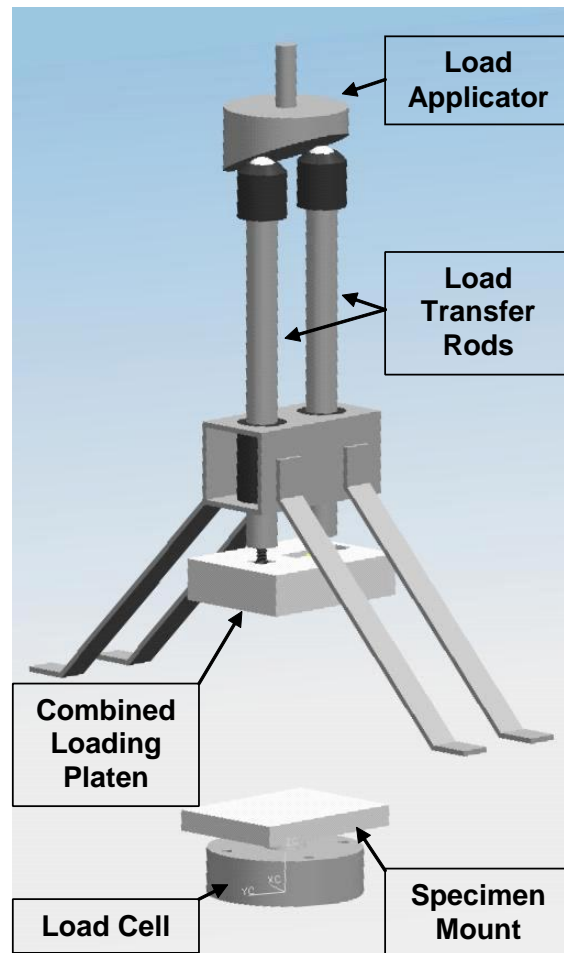


Figure 15: Conceptual design rendering of the combined loading fixture

Fabrication of the project combined loading fixture commenced after the prototype tests were complete (Figures 20-22). Two design changes were incorporated in the modified design. The first design change consisted of reducing the angle of the inclined surface on the load applicator from 22° to 11° which reduced the maximum bending angle placed on the vertebral body to 5° . The second design change was to include a flat section on half of the load applicator, with the other half inclined at the desired angle noted above. The purpose of the flat section on the load applicator was to prevent lift off of the combined loading platen from the posterior rim of the vertebral body.

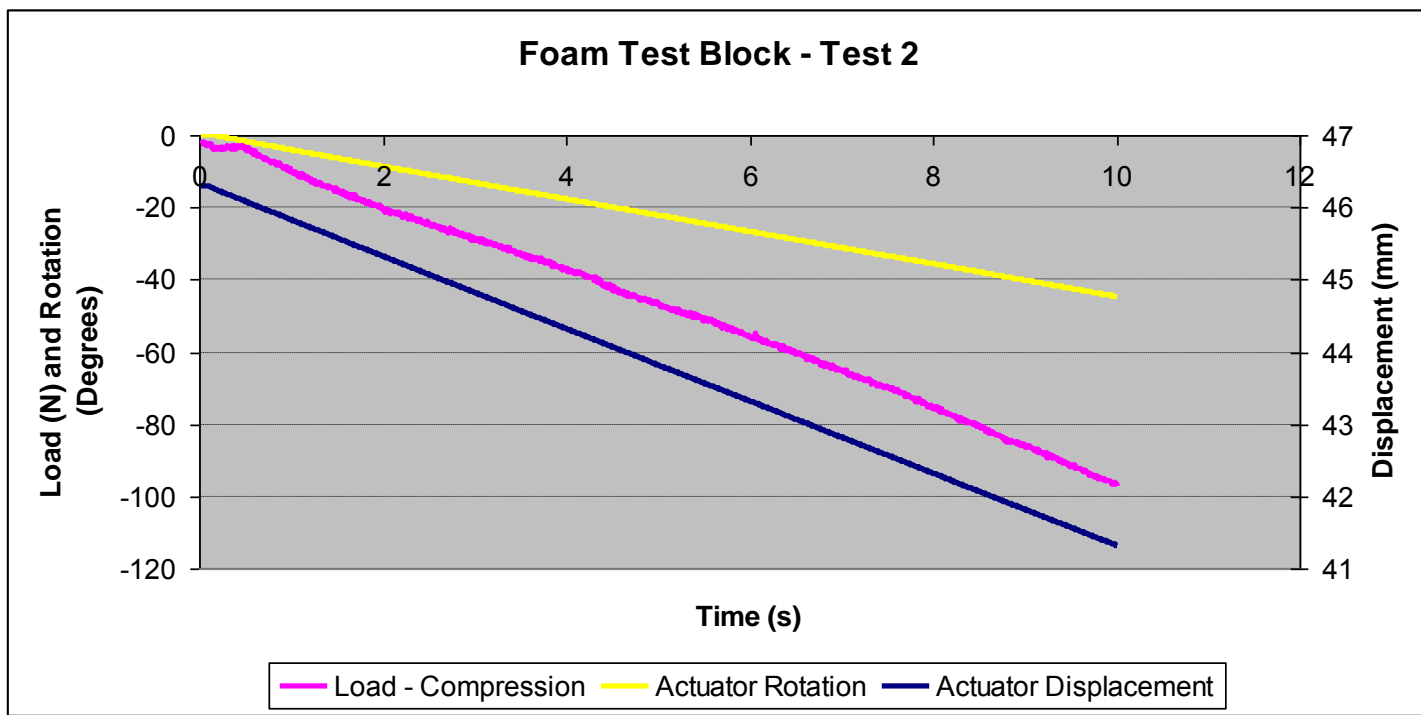


Figure 16: Prototype test #2. Foam block spinal surrogate.

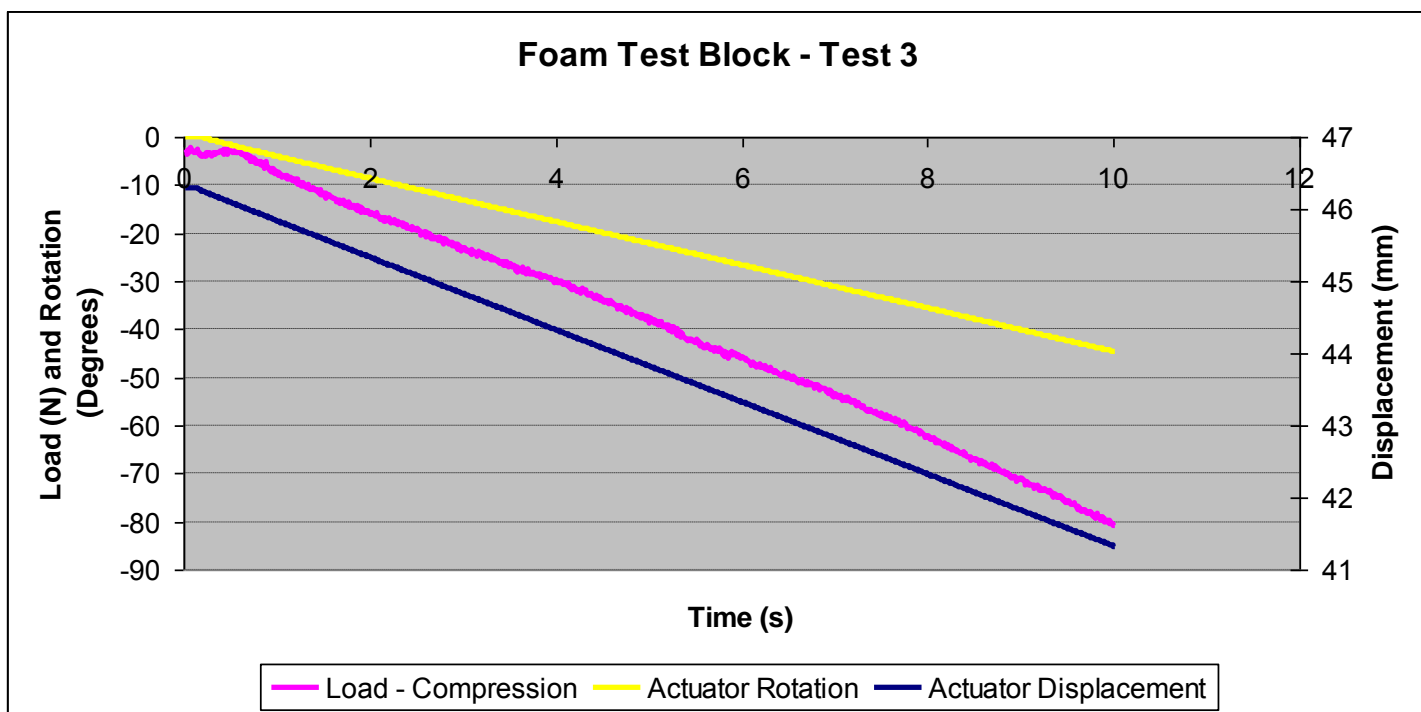


Figure 17: Prototype test #3. Foam block spinal surrogate.

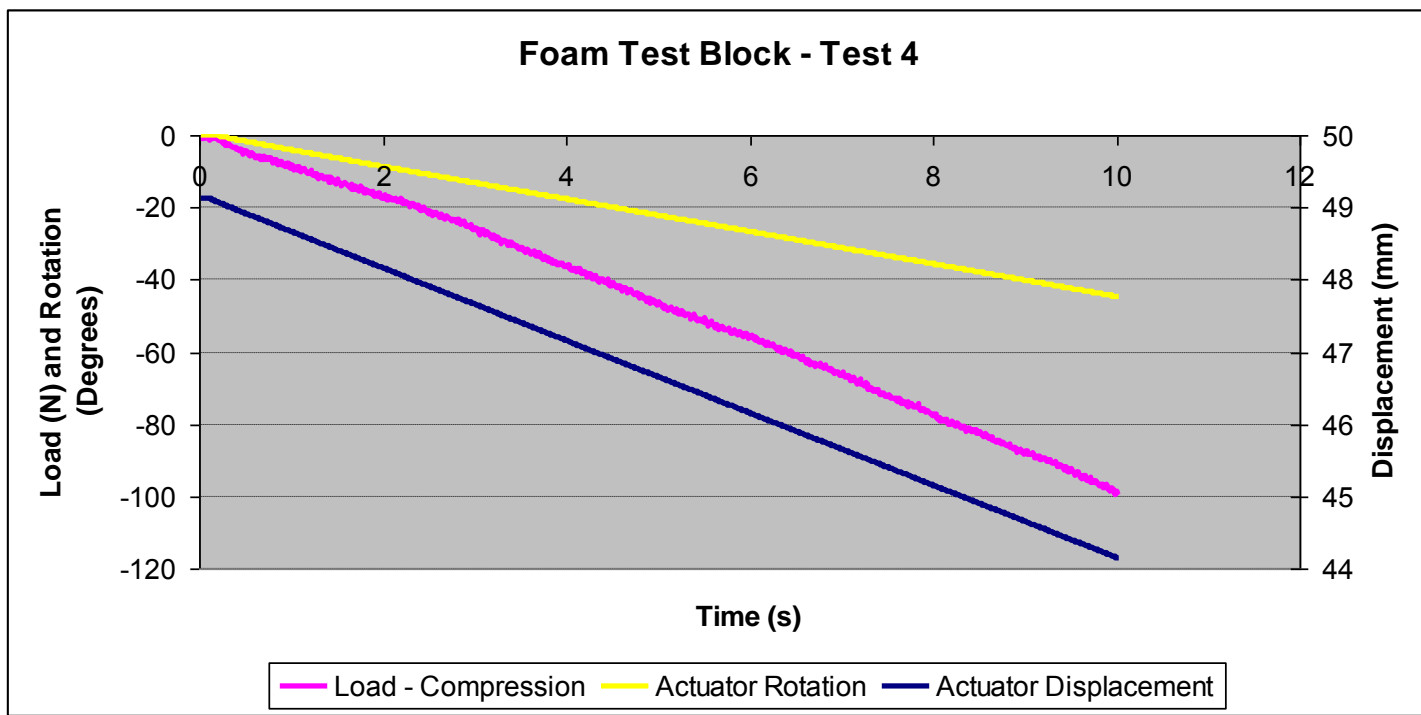


Figure 18: Prototype test #4. Foam block spinal surrogate.

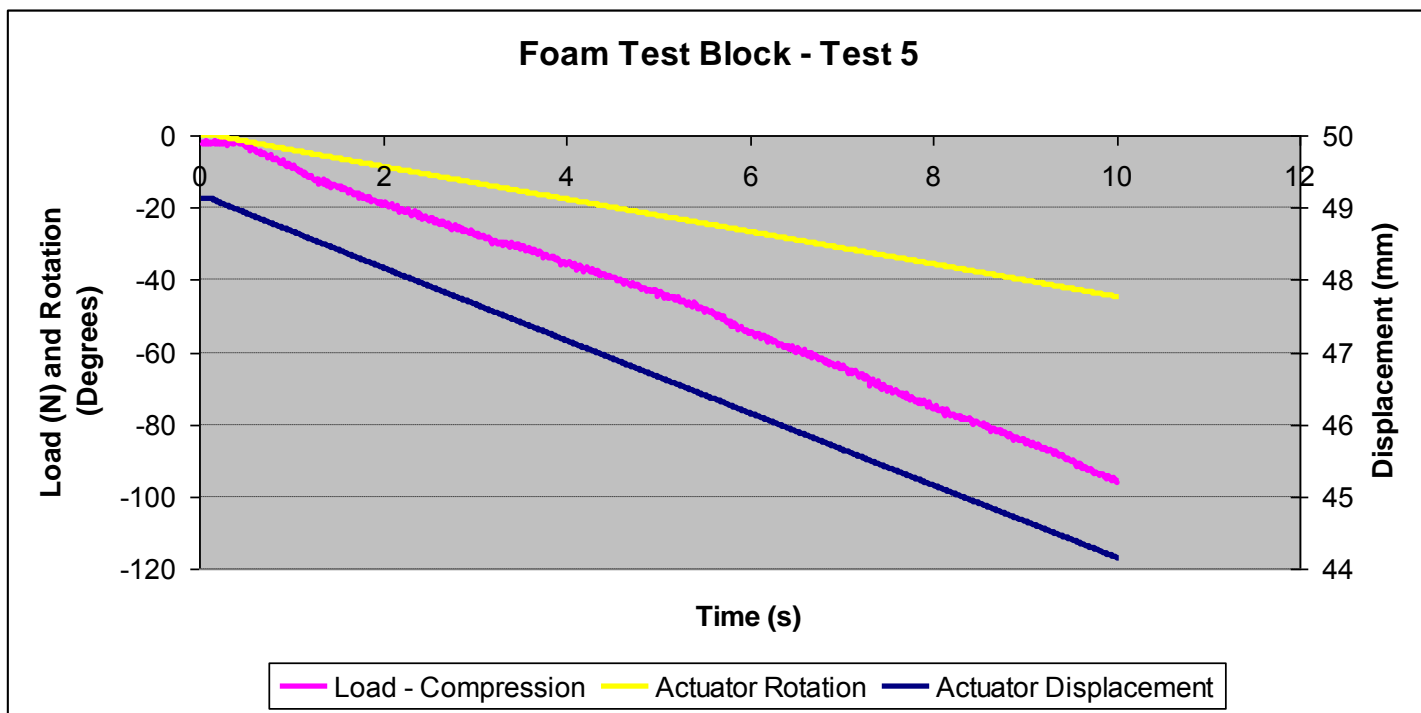


Figure 19: Prototype test #5. Foam block spinal surrogate.

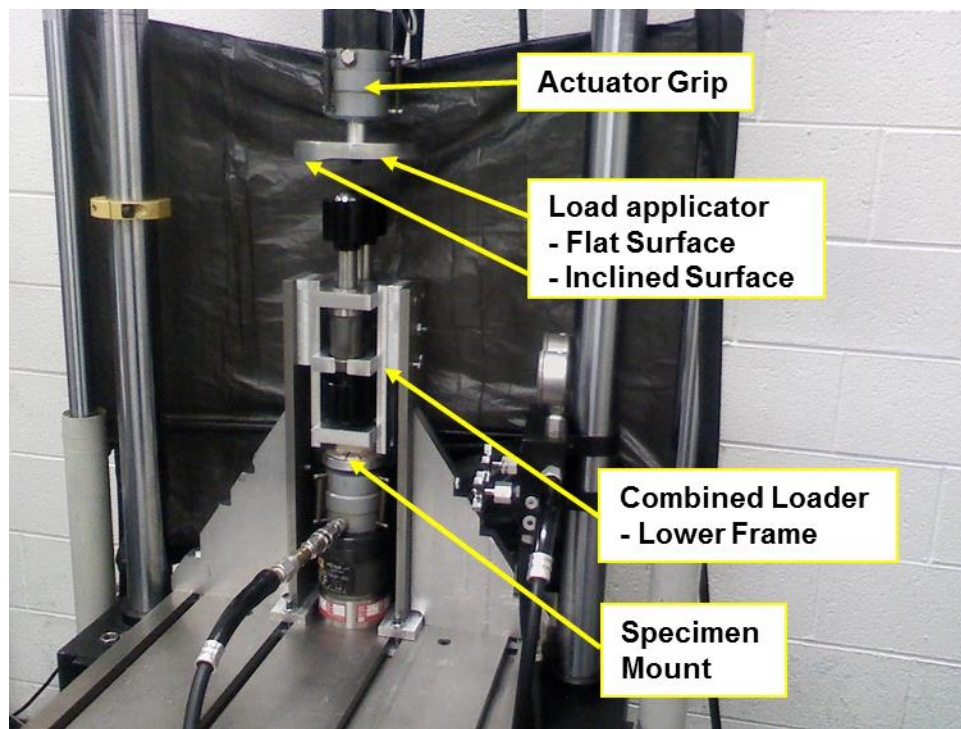


Figure 20: Preliminary wedge loading fixture. Load applicator attached to the test machine actuator is shown with flat and inclined sections.

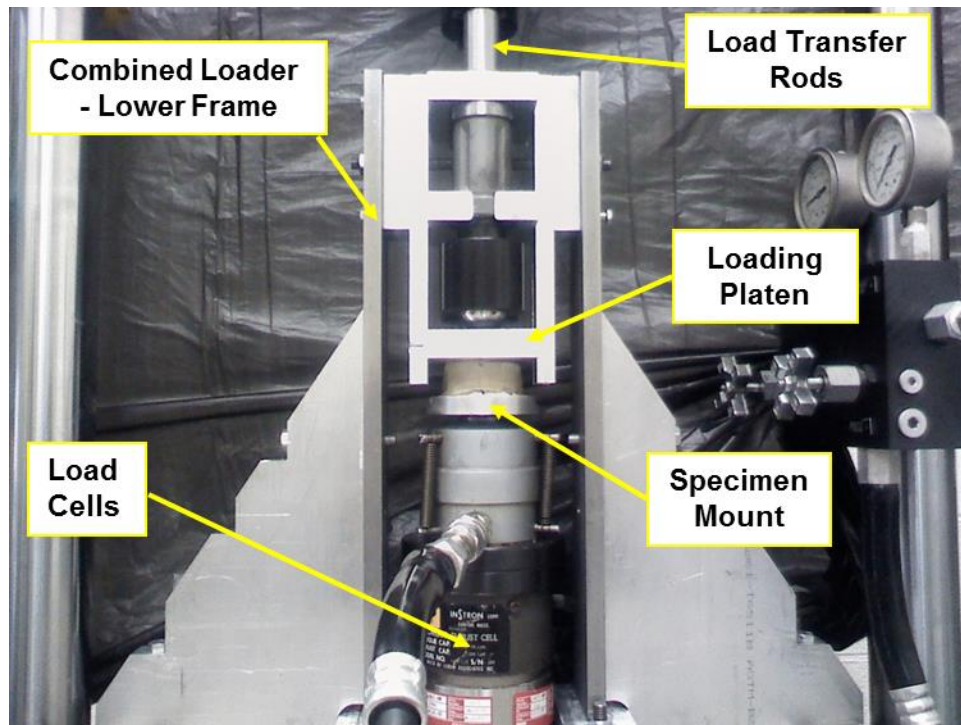


Figure 21: Preliminary wedge loading fixture – lower frame. Lower frame shows the load transfer rods, loading platen and specimen mounted and attached to load cell.

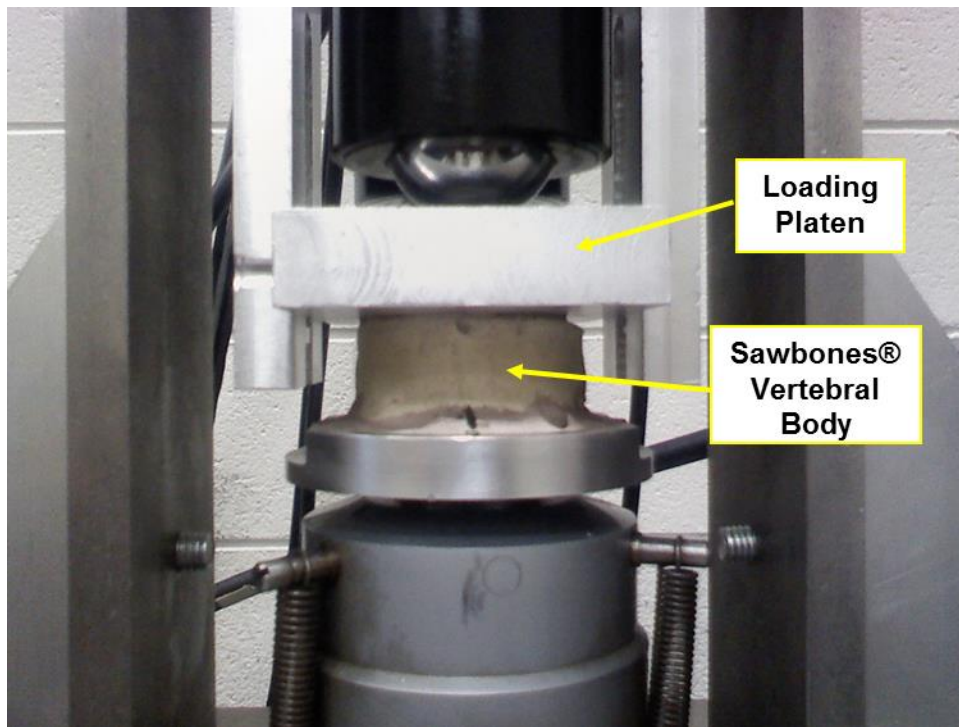


Figure 22: Preliminary wedge loading fixture – lower frame, loading platen and specimen mount. Picture shows a Sawbones® surrogate vertebral body specimen positioned in the loading fixture between the loading platen and specimen mount. View is in the A-P direction and bending will be applied anteriorly in the sagittal plane.

In our calculations we have assumed that the vertebral body loading, with the combined loading fixture, will conform to a beam theory cantilever model (Figure 23). The model assumes a fixed end (the potted inferior vertebral endplate) and a guided opposite end (superior vertebral endplate). The input forces are P (compressive load) and W (transverse load), with W placed at a distance a from the superior endplate. In this case, a equals zero. The reaction moments at the superior and inferior endplates can be calculated from these loads. The forces (P & W) are directly measured with a 3-axis load cell (FUTEK Advanced Sensor Technology Inc., Irvine CA, USA).

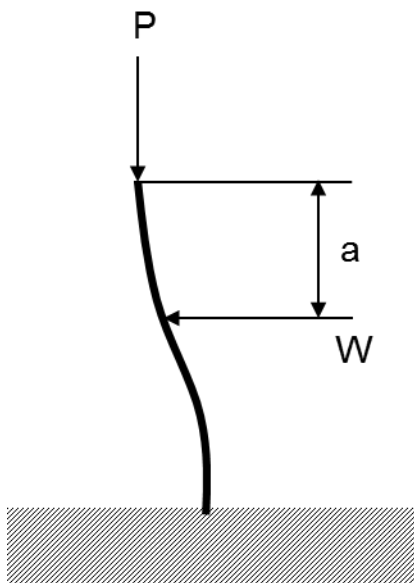


Figure 23: The model for the multiaxial (wedge) loading.

Multiple tests were conducted on a Sawbones® vertebral body using the combined loading fixture. Test modes included compression only, bending, and combined compression and bending. Compression and combined loading tests were conducted with an endpoint uniaxial displacement of 2mm and 1mm, respectively, in the vertical (z -axis) direction at a rate of 0.1 mm/s. Bending and combined loading tests were conducted with a rotary actuator endpoint rotation of 30°-40° and 20°-30°, respectively, at a rate of 1°/s. The observed loads were within the expected range of loads for cadaveric vertebrae. Loads ranged from 4993N to 9047N. During these tests it was noted that the z -axis displacement did not travel to the programmed endpoints or at the programmed displacement rate. The result was endpoint displacements that increasingly deviated from the programmed endpoint as the distance travelled increased (Figure 24). Also the displacement behavior at the transition between downward and upward travel became nonlinear. The first three displacement-time curves (1.0 mm

endpoint – 1mm/s, 1.5 mm endpoint – 1mm/s, 2.0 mm endpoint – 1mm/s) show that the actual displacement was 83% and 77.0% of the programmed endpoint for 1.0 mm of travel and 2.0 mm of travel, respectively. The displacement rates had similar deviation from the programmed value. This issue was found to be a result of the PID gain settings of the displacement control feedback loop in the materials test machine. The PID gain settings were modified to optimum settings for the test setup, which corrected the endpoint displacement and rate to a maximum of 91% of the programmed values (1.0 mm endpoint – 0.1mm/s – P30I20), without the actuator control becoming unstable.

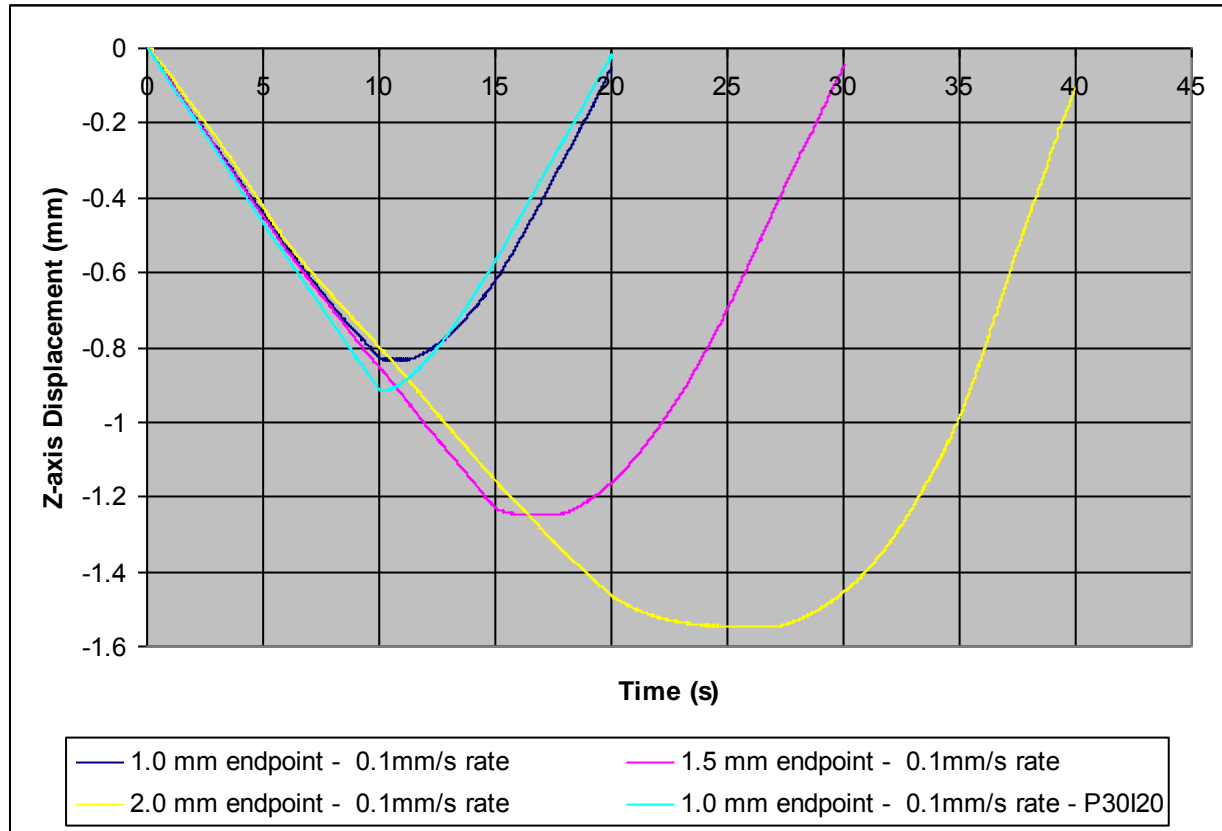


Figure 24: Comparison of z-axis displacement deviation from programmed endpoint and displacement rate. The deviation between the programmed and actual travel increases as a function of the endpoint distance.

Another aspect of the displacement deviation that has to be accounted for is the machine compliance. During a mechanical test, the recorded displacement of the actuator is comprised of specimen and test apparatus deformations (Kalidindi et al., 1997):

$$\delta_R = \delta_C + \delta_S$$

where, δ_R is the recorded displacement of the actuator, δ_C is the deformation of the test apparatus, the combined loading fixture in this case, and δ_S is the specimen deformation. Tests were conducted to characterize the machine compliance by defining an expression for the test apparatus deformations in terms of the applied force $\delta_C(F)$. Upon inspection of applied displacement axial displacement and rotation vs. linear variable displacement transducer (LVDT) measurement at the superior platen surface, it was determined that excessive compliance was present in this construct due to unavoidable internal movement within the linear bearing and ball transfer housing. Using the information gained from the preliminary wedge loader model, a simplified construct was fabricated which allowed combined loading via a lever arm with an offset hinge.

Final wedge loader model

The final wedge loader model produced uniaxial compression and a bending moment through the use of the linear actuator only (Figure 25). In this construct, a specimen-specific total displacement was applied at the top surface of a flat beam lever at a specimen-specific distance from a fixed hinge via a ball transfer. The entire construct is free to translate left and right in order to set a hinge-specimen distance, which can be locked to the table via four bolts. The height of the hinge point is set before each test such that the loader beam is level.

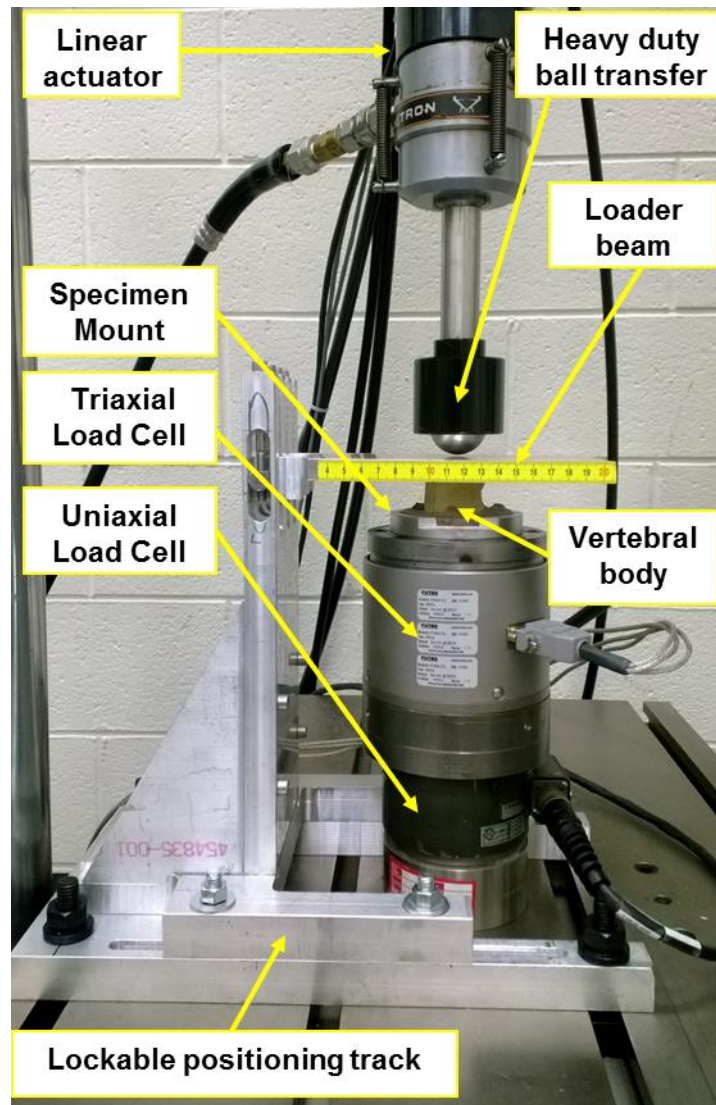


Figure 25: Final wedge loader. The simplified design allows for accurate specimen positioning with minimized system compliance.

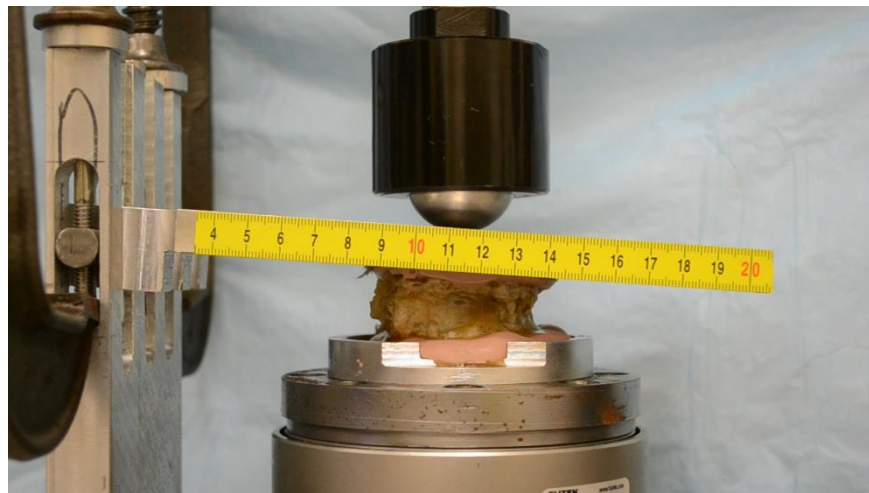


Figure 26: Close-up view of deformed human vertebral body in final wedge loader system.

Forces are measured at the inferior end via a FUTEK triaxial load cell, as well as the Instron uniaxial load cell at 100 Hz recording frequency. High quality video was also recorded throughout testing (Figure 26). The total displacement was calculated such that the test introduced a mild wedge fracture with 10% difference in height between posterior and anterior heights and an overall 25% mean reduction in vertebral height (see calculations below). Displacement rate was constant at 0.1 mm/sec.

Final wedge loader calculations

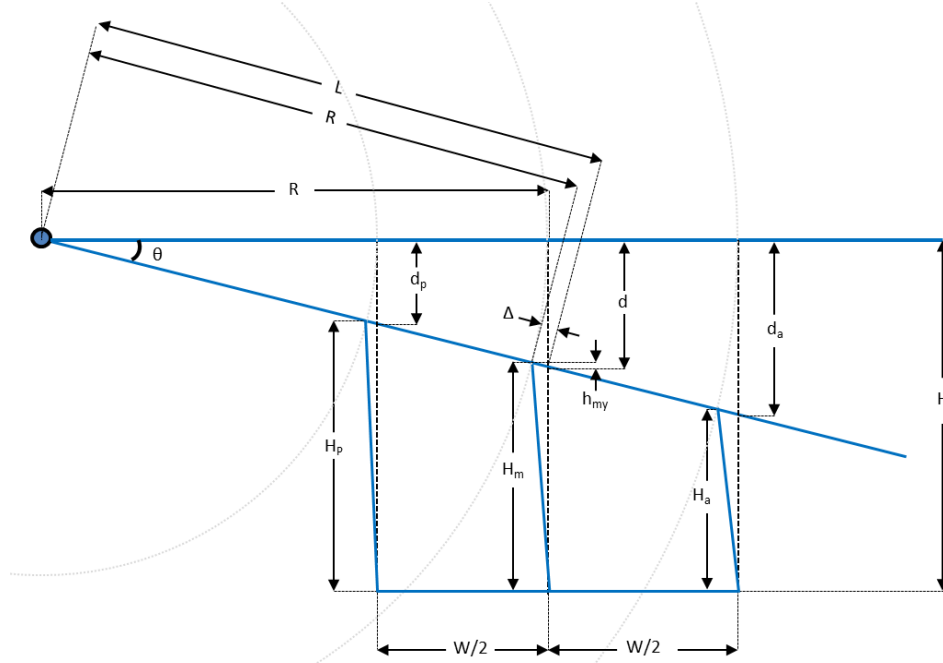


Figure 27: Combined loading parameters were defined by distance between the specimen center and the hinge point (R), as well as total actuator displacement (d).

In order to introduce a pre-determined ratio of anterior height (H_a) to posterior height (H_p) ($H_a/H_p=0.9$) and a mean specimen reduction in height $c=0.75$, distance between specimen center and hinge point (R) and total actuator displacement (d) were determined using the undeformed heights (H) and anterior-posterior widths (W) of each specimen, which were determined from CT images. The specimen was potted on both inferior and superior surfaces, and inferior surface was fixed while the superior surface was free to translate along the loader beam. The system was thus modeled with a polar approach, where superior contact surfaces were considered to translate and rotate together with the loader beam along a radius originating at the hinge point.

From the geometry in Figure 27, the following constraints were established:

- (1) $L = R + \Delta$
- (2) $L \sin \theta = d$
- (3) $L \cos \theta = R$

Substituting L from (1) into equations (2) and (3) yielded:

- (4) $(R + \Delta) \sin \theta = d$
- (5) $(R + \Delta) \cos \theta = R$

Pythagorean Theorem was used to find an expression for Δ in terms of R and d :

$$\begin{aligned}
 L^2 &= (R + \Delta)^2 = R^2 + d^2 \\
 R^2 + 2R\Delta + \Delta^2 &= R^2 + d^2 \\
 \Delta^2 + 2R\Delta - d^2 &= 0 \\
 (6) \quad \Delta &= \frac{-2R \pm \sqrt{4R^2 - 4d^2}}{2} = \begin{cases} -R - \sqrt{R^2 + d^2} \\ -R + \sqrt{R^2 + d^2} \end{cases}
 \end{aligned}$$

The y component of Δ was calculated as such:

$$(7) \quad h_{my} = \Delta \sin \theta = H_m - (H - d)$$

Substituting the positive solution for (6) for Δ and equation (4) for $\sin \theta$ yielded the following relationship:

$$(8) \quad (-R + \sqrt{R^2 + d^2}) \left(\frac{d}{\sqrt{R^2 + d^2}} \right) = H_m - (H - d)$$

Equation (8) was solved for d :

$$(9) \quad d = \frac{R(H-H_m)}{\sqrt{(R^2-(H-H_m)^2)}}$$

H_m was assumed to be a constant times the undeformed height:

$$(10) \quad H_m = c \times H$$

Equation (10) was substituted for H_m in equation (9):

$$(11) \quad d = \frac{R(H-cH)}{\sqrt{(R^2-(H-cH)^2)}} = \frac{RH(1-c)}{\sqrt{(R^2-(H(1-c))^2)}}$$

Considering that the lines drawn by distances d_p and d_a form similar triangles to the triangle drawn with distance d , $(H-H_p)$ and $(H-H_a)$ replaced $(H-H_m)$ in equation 9 in the expressions for d_p and d_a , respectively. Likewise, $(R-W/2)$ and $(R+W/2)$ replaced R in equation 9 in the expressions for d_p and d_a , respectively:

$$(12) \quad d_p = \frac{(R-\frac{W}{2})(H-H_p)}{\sqrt{\left(\left(R-\frac{W}{2}\right)^2-(H-H_p)^2\right)}}$$

$$(13) \quad d_a = \frac{(R+\frac{W}{2})(H-H_a)}{\sqrt{\left(\left(R+\frac{W}{2}\right)^2-(H-H_a)^2\right)}}$$

From the geometry in Figure 27, we know the following relationships hold:

$$(14) \quad \frac{d_p}{R-\frac{W}{2}} = \frac{d_a}{R+\frac{W}{2}} = \tan \theta$$

Substituting equations (12) and (13) for d_p and d_a in equation (14) yielded:

$$(15) \quad \frac{(H-H_p)}{\sqrt{\left(\left(R-\frac{W}{2}\right)^2-(H-H_p)^2\right)}} = \frac{(H-H_a)}{\sqrt{\left(\left(R+\frac{W}{2}\right)^2-(H-H_a)^2\right)}}$$

It was desired that the mechanical test continued until ratio H_p/H_a reached a physiologically relevant constant k :

$$(16) \quad \frac{H_p}{H_a} = k \quad \rightarrow \quad H_p = kH_a$$

H_p from equation (16) was substituted into equation (15) and then solved for H_a :

$$(17) \quad H_a = \frac{HW}{kR+\frac{kW}{2}-R+\frac{W}{2}} = \frac{HW}{R(k-1)+\frac{W}{2}(k+1)}$$

The similar triangles formed by distances $H-H_a$ and $H-H_m$ were used to calculate R :

$$(18) \quad \sin \theta = \frac{H-H_m}{R} = \frac{H-H_a}{R+W/2}$$

Substituting $H_m=cH$ into equation (18) and solving for R yielded:

$$(19) \quad R = \left(\frac{W}{2}\right) \left(\frac{H-cH}{cH-H_a}\right)$$

The value for R found in equation (19) was substituted into equation (17):

$$(20) \quad (k+1)H_a^2 - (k+1+2a)HH_a + 2cH^2 = 0$$

Solving for H_a yielded the following relationship:

$$(21) \quad H_a = \frac{H}{2} \times \frac{(k+1+2c) \pm \sqrt{(k+1+2c)^2 - 8c(k+1)}}{(k+1)}$$

The radicand in equation (21) must be equal to or greater than 0:

$$(k+1)^2 + 4c(k+1) + 4c^2 - 8c(k+1) \geq 0$$

$$(k+1)^2 - 4c(k+1) + 4c^2 \geq 0$$

$$[(k+1) - 2c]^2 \geq 0$$

Thus,

$$(k+1) - 2c \geq 0 \quad \text{and} \quad (k+1) - 2c \leq 0$$

$k \geq 2c - 1$ and $k \leq 2c - 1$, therefore all values of k and c are admissible.

The value found for H_a in equation (21) was substituted into equation (19), forming the expression for R :

$$(22) \quad R = \left(\frac{W}{2}\right) \left(\frac{H - cH}{cH - \left(\frac{H}{2} \times \frac{(k+1+2c) \pm \sqrt{(k+1+2c)^2 - 8c(k+1)}}{(k+1)}\right)} \right)$$

The value found for R in equation (22) was substituted into equation (11), forming the expression for d :

$$(23) \quad d = \frac{\left(\frac{W}{2}\right) \left(\frac{H - cH}{cH - \left(\frac{H}{2} \times \frac{(k+1+2c) \pm \sqrt{(k+1+2c)^2 - 8c(k+1)}}{(k+1)}\right)} \right) H(1-c)}{\sqrt{\left(\left(\left(\frac{W}{2}\right) \left(\frac{H - cH}{cH - \left(\frac{H}{2} \times \frac{(k+1+2c) \pm \sqrt{(k+1+2c)^2 - 8c(k+1)}}{(k+1)}\right)} \right) \right)^2 - (H(1-c))^2}}$$

Simplifying this expression yielded:

$$(24) \quad d = \frac{(c-1)^2 H(k+1)W}{((2c-1)k + \sqrt{(-2c+k+1)^2 - 1}) \sqrt{(c-1)^2 \left(\frac{(k+1)^2 W^2}{((2c-1)k + \sqrt{(-2c+k+1)^2 - 1})^2} - H^2 \right)}}$$

In addition, k and c must be chosen appropriately to yield R and d values that simultaneously fulfill several physical constraints of the mechanical testing setup (Figure 28):

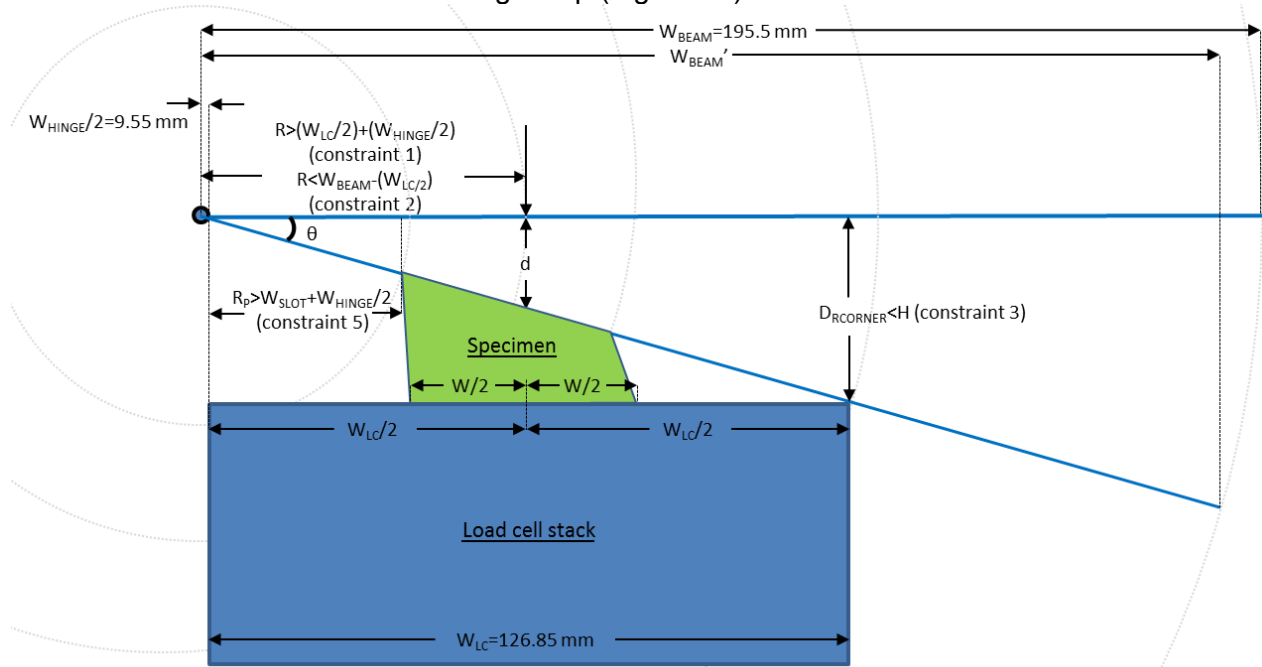


Figure 28: Physical constraints of the mechanical testing system imposed by loader geometry. Values for R and d must be chosen according to these constraints so that the test is feasible.

Constraint 1: If the load cell stack is moved as far left as possible, the value for R is inadmissible if less than the radius of the load cell stack plus half the thickness of the vertical support which contains the hinge pivot point at its center:

$$R > \left(\frac{W_{LC}}{2}\right) + \left(\frac{W_{HINGE}}{2}\right)$$

$$R > \left(\frac{126.85 \text{ mm}}{2}\right) + \left(\frac{19.1 \text{ mm}}{2}\right)$$

$$R > 72.975 \text{ mm}$$

Constraint 2: Taking into account translation of the loading point down the length of the beam during rotation, the value for R must be less than the original length of the beam less the x component resulting from rotation minus half the width of the specimen:

Using known quantities, solve for theta:

$$\sin \theta = \frac{H - H_m}{R}$$

$$\theta = \sin^{-1} \left(\frac{H - H_m}{R} \right)$$

Substitute the value for theta found above into the following expression and solve for W_{BEAM}' :

$$\cos \theta = \frac{W_{BEAM}'}{W_{BEAM}}$$

$$W_{BEAM}' = W_{BEAM} \cos \theta = 195.5 \text{ mm} \times \cos \theta$$

As discussed above, the following relationship must hold:

$$R < W_{BEAM}' - \left(\frac{W}{2} \right)$$

$$(25) \quad R < W_{BEAM} \cos \theta - \left(\frac{W_{LC}}{2} \right)$$

$$R < 195.5 \text{ mm} \times \cos \theta - \frac{W}{2}$$

Constraint 3: So as to avoid damaging the upper right corner of the load cell with the free end of the loader beam, the vertical displacement of the loading beam at a distance $R + W_{LC}/2$ (called $D_{RCORNER}$) must be less than the undeformed specimen height.

From the geometry drawn above, we know the following relationships:

$$\tan \theta = \frac{d}{R}$$

$$\tan \theta = \frac{D_{RCORNER}}{R + \frac{W_{LC}}{2}}$$

Set these expressions equal to each other and solve for $D_{RCORNER}$:

$$\frac{d}{R} = \frac{D_{RCORNER}}{R + \frac{W_{LC}}{2}}$$

$$D_{RCORNER} = \frac{d}{R} \times \left(R + \frac{W_{LC}}{2} \right) = d + \frac{dW_{LC}}{2R}$$

As discussed above, the following relationship must hold:

$$(26) \quad d + \frac{dW_{LC}}{2R} < H$$

Constraint 4: The pot has a 3" inside diameter (D_{POT}). The Feret diameter (D_F) was measured from a max intensity projection of all axial CT slices for a binarized mask of each vertebra. The Feret diameter is essentially a "caliper diameter" (i.e., the diameter of the smallest circle that would completely enclose the shape).

$$D_F < D_{POT}$$

This constrain held true for the largest vertebra, thus the 3" pot was appropriate for all specimens.

Constraint 5: To facilitate the hinge mechanism, the loader beam has a slot milled in it which extends 1.91 cm from the vertical support. Through rotation, the posterior edge of the superior construct surface (a distance R_P from the pivot point) cannot slide onto the slotted portion of the loader beam, so R_P in the deformed configuration must be more than half the hinge width ($W_{HINGE}/2$) plus the slot length (W_{SLOT}). This constraint can be expressed in terms of R :

Where $R_P = R - \frac{W}{2}$ and $R_P > W_{SLOT} + \frac{W_{HINGE}}{2}$

$$R - \frac{W}{2} > W_{SLOT} + \frac{W_{HINGE}}{2}$$

$$(27) \quad R > W_{SLOT} + \frac{W_{HINGE}}{2} + \frac{W}{2}$$

Equations (22) and (24) were solved for R and d , respectively, for an array of possible k and c combinations (in 0.025 increments) using specimen-specific geometry values W and H determined from CT images. This was done for the smallest specimen (lowest W and H) as a worst case scenario, because it would produce the lowest R value. The combination of k and c was simultaneously optimized such that a physiologically relevant wedge fracture was produced while system constraints 1-5 were fulfilled. Optimized k and c values were established via this method and applied for all specimens, such that the mechanical test would end at 25% mean reduction in height with 10% difference between posterior and anterior heights. Subsequently solving equations (22) and (24) to establish R and d values for all 40 specimens fulfilled constraints 1-5 for all specimens.

The 40 human vertebral bodies were tested to failure following all imaging studies. An example failure curve is shown in Figure 29. Local maximum at the first peak was considered failure load.

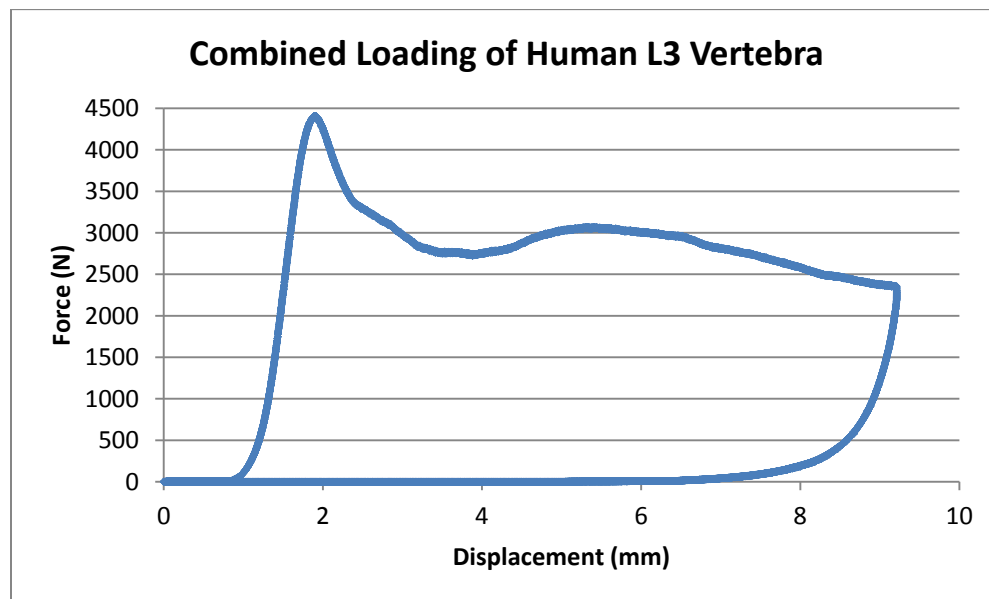


Figure 29: Example force-displacement curve from a human L3 vertebra using the final wedge loader system. Failure load was recorded for the purpose of correlation with texture parameters from tomosynthesis images.

Task 6. Publications, Reports and Proposal Writing (Months 11-12)

Kim, W., Oravec, D., Sander, E., Divine, G. W., Flynn, M. J. and Yeni, Y. N., "Digital Tomosynthesis-Derived Microstructural Parameters Predict Cancellous Bone Stiffness in Human Vertebrae". 59th Annual Meeting of the Orthopaedic Research Society, San Antonio, Texas. (2013). Poster 0701.

Kim, W., Oravec, Divine, G. W., Flynn, M. J. and Yeni, Y. N., " Digital Tomosynthesis of Human Vertebral Bone: The Effect of Positioning and Scan Orientation on Prediction of Cancellous Bone Stiffness."

Conference abstract submitted to the 60th Annual Meeting, Orthopaedic Research Society, March 15-18, 2014, New Orleans, Louisiana.

Kim, W., Oravec, Divine, G. W., Maatman, T, Flynn, M. J. and Yeni, Y. N., "Digital Tomosynthesis for Prediction of Human Whole Vertebral Stiffness"

Conference abstract submitted to the 60th Annual Meeting, Orthopaedic Research Society, March 15-18, 2014, New Orleans, Louisiana.

Kim, W., Oravec, D., Nekkanty, S., Yerramshetty, J., Sander, E., Divine, G. W., Flynn, M. J. and Yeni, Y. N., "Digital tomosynthesis (DTS) for quantitative assessment of trabecular microstructure in human vertebral bone"
Manuscript in preparation to be submitted to Spine. A final draft is generated, under review by the senior author.

Xiao, A. and Yang, E. "Topographical Measurements of Vertebral Endplate to Predict Bone Fragility:

Comparison of Digital Tomosynthesis and High Resolution Computed Tomography with Microcomputed Tomography". September 27, 2013.

Report submitted by summer research students to the 2013 Siemens Competition in Math, Science & Technology.

Tomosynthesis for assessment of hip bone quality and fracture strength

National Institutes of Health (R21)

Requested Award period: 1/1/2014 - 12/31/2015

Role on grant: Principal Investigator

Total Direct Costs: \$275,000

Submitted June 16, 2013. The data from the current project was a part of the preliminary data supporting the feasibility of the DTS methods to be used in assessment of hip bone quality and fracture risk.

Tomosynthesis of the human spine in vivo for assessment of vertebral bone quality

National Institutes of Health (R01)

Requested Award period: 4/1/2014 - 3/31/2019

Role on grant: Principal Investigator

Total Direct Costs: \$1,250,000

To be submitted November 12, 2013. The submission has been delayed (from Oct 5) due to government shutdown during the submission deadline. Data from the current project was the major motivation to develop and test a DTS approach applicable in vivo for assessment of vertebral bone quality and fracture risk.

With the submission of this final report this task is complete.

Results:

Results from Task 2

Density Phantom Images

If the analysis region is limited to the central portion of the cylinder, a nonlinear relationship was found between radiographic density (DTS gray values) and solution density (Figure 30a, b) (A cubic polynomial explains over 99.9% of this relationship). The within-session and between session variability of density phantoms was less than 5% (coefficient of variation=0.5% to 4.7%) with largest variations caused by air (3.5% and 4.7% for within- and between-session variability, respectively).

Radiograph gray value was found to have a linear response to increased solution density (Figure 31).

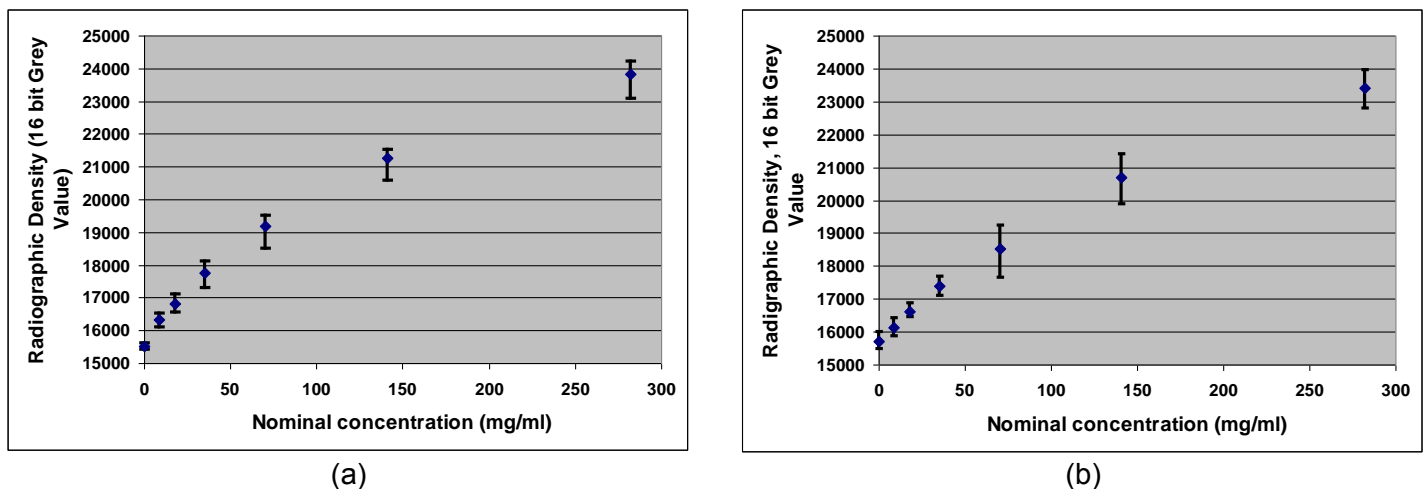


Figure 30: (a) Average DTS gray value versus solution density for 5 sessions. (b) Average DTS gray value versus solution density within a single session. Error bars represent between-session gray value range.

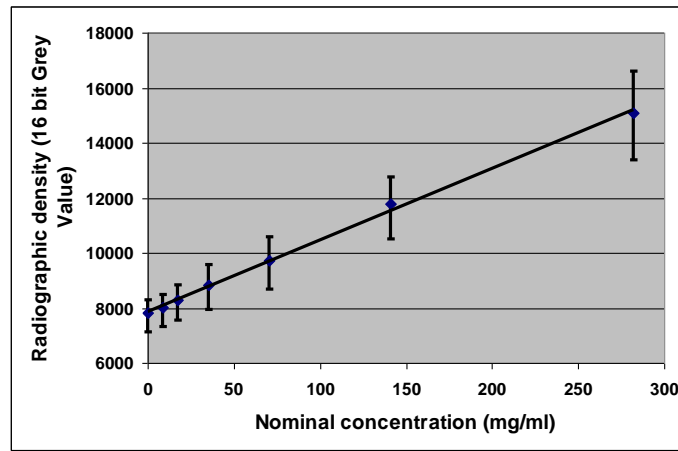


Figure 31: Average DTS gray value versus solution density vs. solution concentration obtained from DTS radiogram. Error bars represent the range of gray values. ($R^2=0.9981$ for linear regression.)

Although the nonlinear relationship found between gray values and density in DTS images may be useful for quantitative purposes, the edge enhancement apparent in DTS images may affect neighboring radiographic density values making quantitative density measurements difficult. On the other hand, the high resolution digital radiography capabilities of the DTS system offer another possibility for density measurements (Kinds et al., 2011). Combined with the structural analyses from the DTS images, density measurements from the DTS radiograms may result in a powerful tool for bone quality assessment.

Spacing phantoms

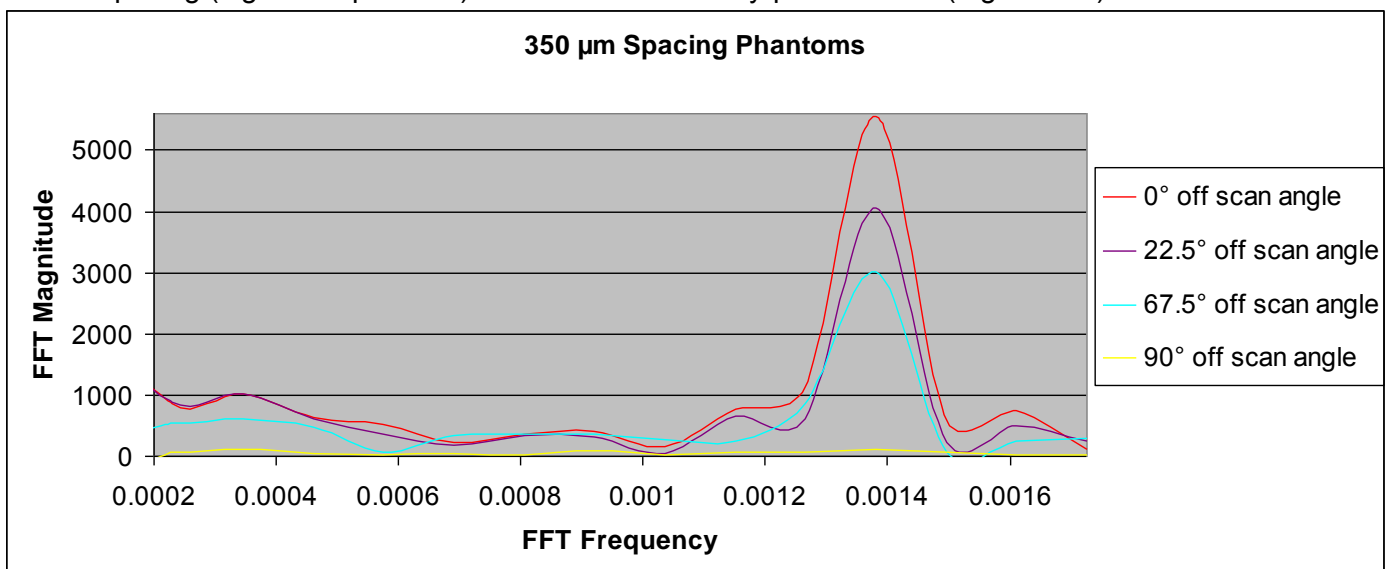
Visual Analysis of DTS Spacing Phantom Images

The 350 and 300 μm spacing phantoms could be resolved visually when oriented 0° , 22.5° , and 67.5° to the scanning direction. The 250 and 200 μm phantoms could only be partially resolved, while 150 and 100 μm phantoms had minimal texture and no visually detectable banding pattern. At the 90° orientation, textural information was completely lost for all spacing phantoms.

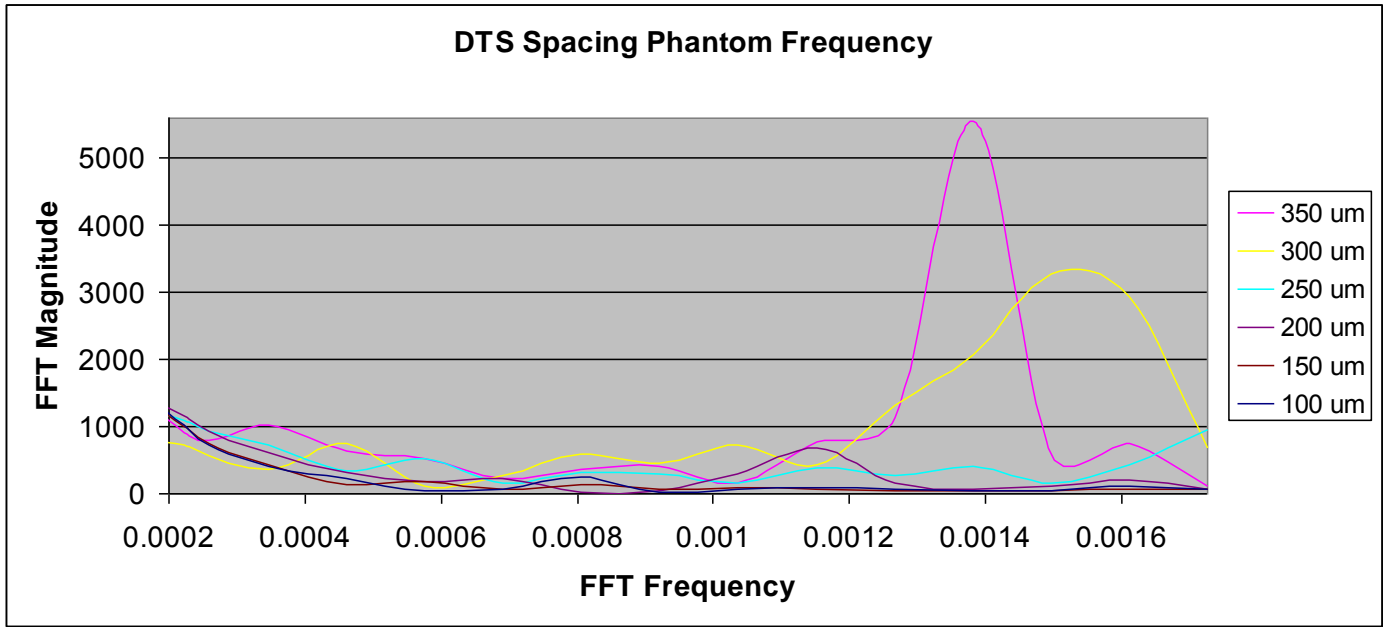
Quantitative Analysis of Microcomputed Tomography and DTS Spacing Phantom Images

Average FFT-measured layer thickness agreed well with thicknesses measured by micrometer during phantom preparation, supporting the use of μCT images as an established reference for further analyses.

For DTS images, of the four phantom angles relative to the scanning direction, orienting the length of the spacing phantom in line with the scanning direction yielded the greatest magnitude of frequency (0° off scanning direction in Figure 32a). Taking the 0° angle as a best resolution case, the FFT analysis method on DTS images accurately identified the phantom spacing for 350 μm and 300 μm , but the peaks were lost at narrower spacing (higher frequencies) consistent with the Nyquist criterion (Figure 32b).



(a)



(b)

Figure 32: (a) FFT magnitude was highest when layers of spacing phantom were oriented perpendicular to the scanning direction. (b) For the 0° angle scan, the FFT method was able to identify spacing accurately for 350 and 300 μm spacing phantoms, but 250 μm and below could not be resolved.

In the MIL, LFD and fractal analyses, we interpret the results with the goal of finding parameters that are sensitive to changes in spacing, i.e., those that monotonically increase or decrease with increasing spacing and those that correlate with μCT measurements of the same kind.

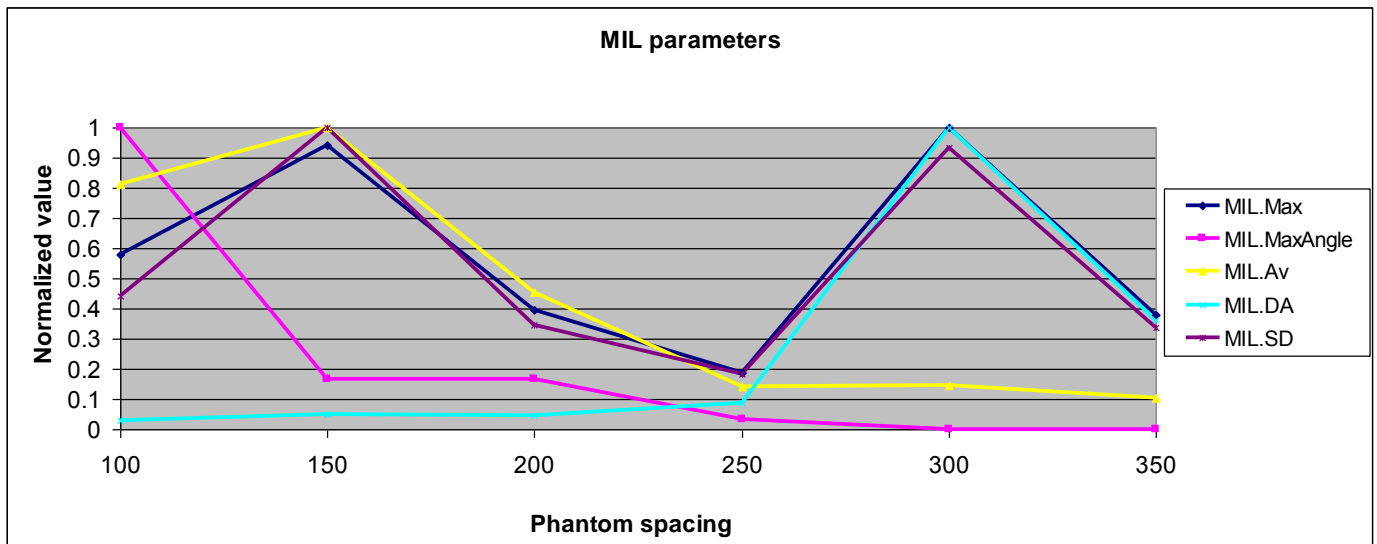
Most of the MIL and LFD parameters measured from DTS did not follow a monotonic relationship with spacing for the full range of spacing, although some trends could be visible (Figure 33a, b). LFD parameters generally performed better than MIL parameters. Consequently, higher correlations were found between DTS LFD and μCT LFD parameters than between DTS MIL and μCT MIL parameters ($R^2=0.60$ for MIL.SD vs $R^2=0.64-0.95$ for LFD.Max, LFD.EllipseMax, LFD.DA, and LFD.SD). Especially noteworthy is the anisotropy of LFD for which DTS and μCT correlated 95%.

Fractal dimension decreases with phantom spacing (increasing image homogeneity) until 150 μm, below which aluminum is inseparable from plastic to resolve a scale-dependent pattern (Figure 33c). The decrease in lacunarity following a peak at 250 μm is possibly because texture heterogeneity is no longer detected due to low resolution and the image appears uniform to the lacunarity analysis (Figure 33c).

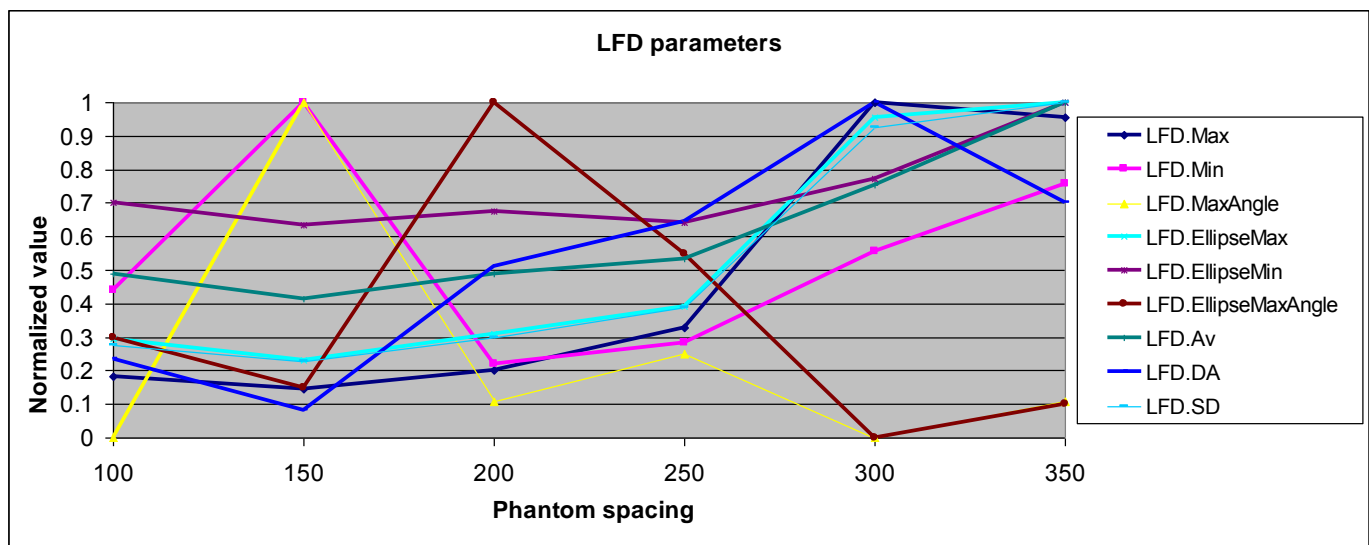
Thickness Phantoms

Visual Analysis of DTS Thickness Phantom Images

Aluminum thicknesses of 120, 115, 90, 75, and 60 μm phantoms could be resolved visually when oriented 0°, 22.5°, and 67.5° to the scanning direction, while 25 μm phantoms had minimal texture and no visually detectable banding pattern. At the 90° orientation, a banding pattern could be identified visually in 120, 115, 90, and 75 μm phantoms, but not in 60 and 25 μm phantoms.



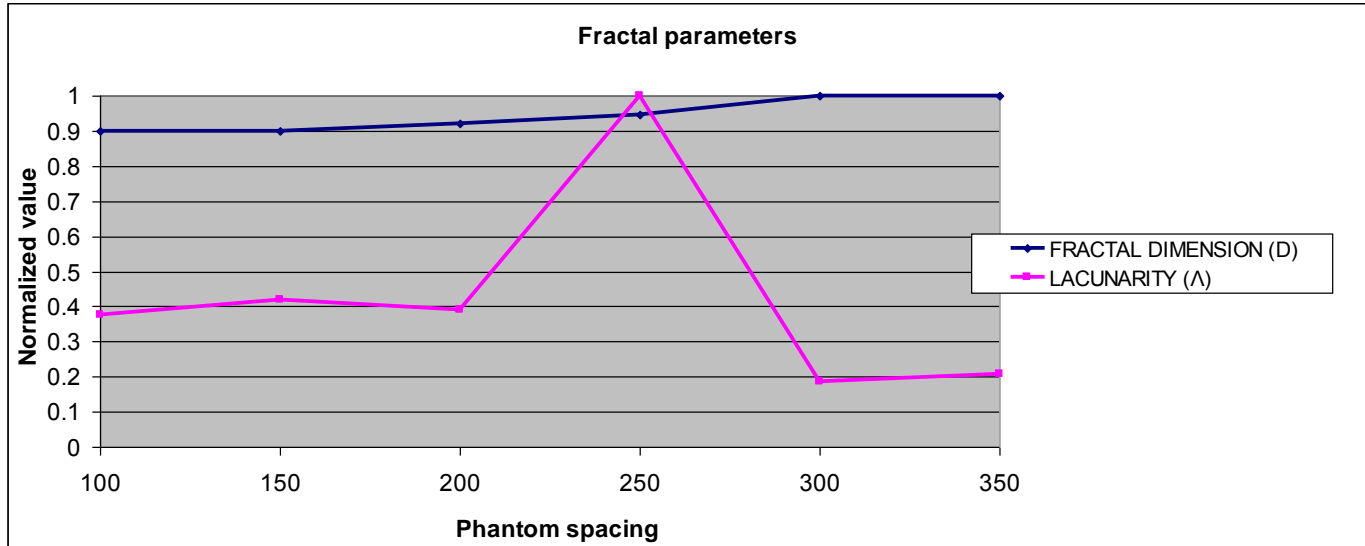
(a)



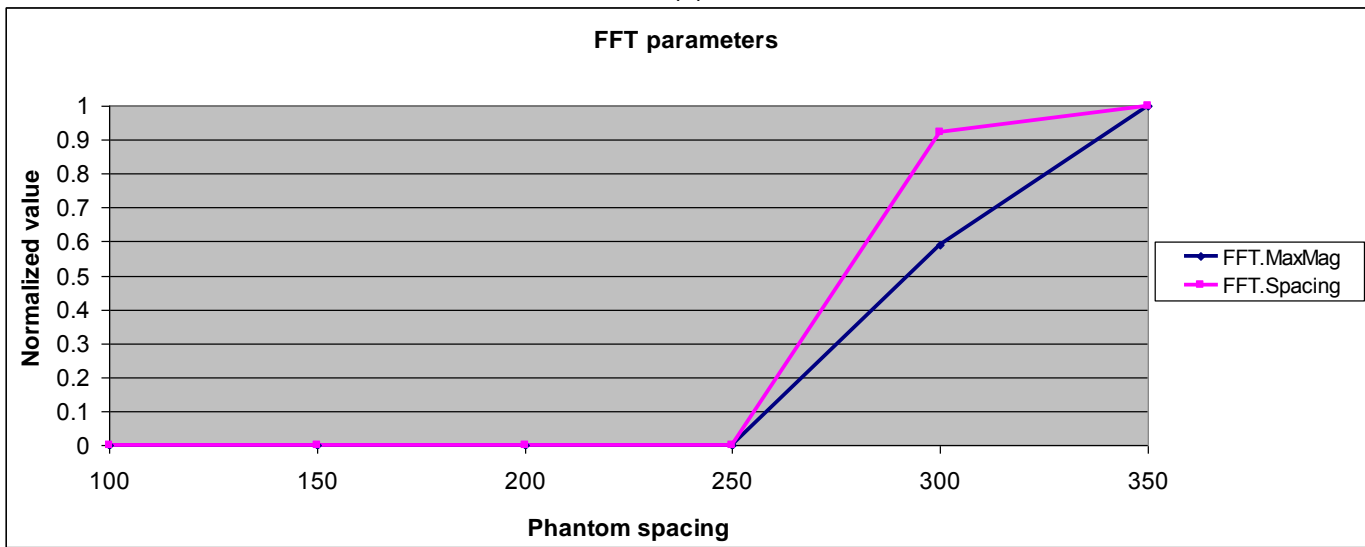
(b)

Figure 33

Figure 33 continued



(c)



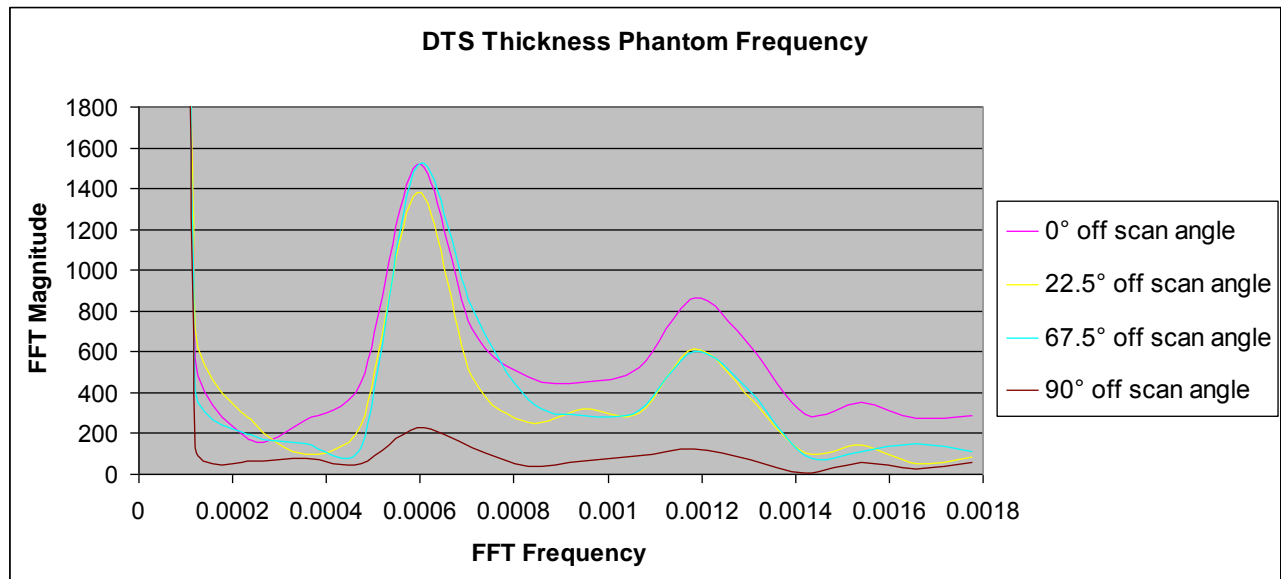
(d)

Figure 33: The changes in morphometric parameters with varying phantom spacing as measured from DTS images. All parameters are normalized for comparison purposes. (a) MIL, (b) LFD, (c) fractal and (d) FFT parameters.

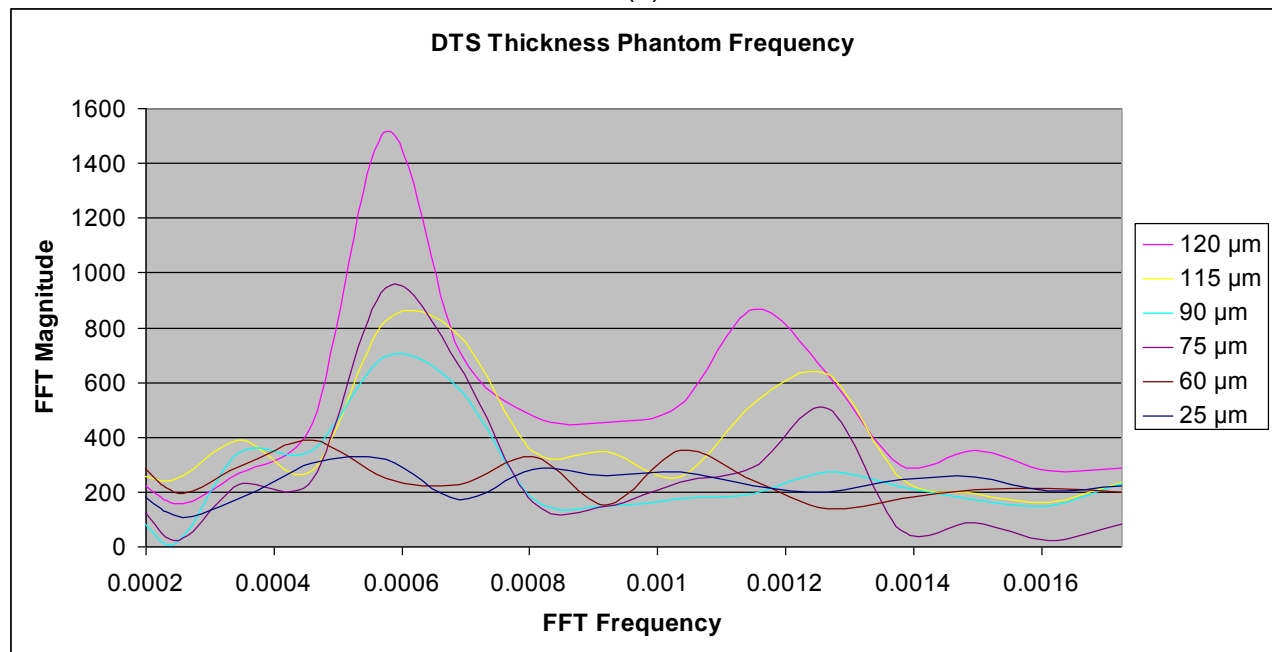
As with the spacing phantoms, thicknesses were resolved best in the 0° scan, well in the oblique angles, and worst in the 90° scan. This is demonstrated as a weakened response of FFT magnitude at the same frequency at different specimen orientations (Figure 34a). FFT magnitude decreased together with decreasing layer thickness until 75 μm , below which aluminum could not be resolved from plastic by the analysis method. Taken together with spacing phantom results, FFT appears to be a sensitive tool for determining presence of small, sufficiently separated features within a structure. The effect of angle on resolving power emphasizes the importance of performing serial scans at various angles to extract the maximum amount of available structural information.

Although FFT analysis was able to resolve frequencies down to 75 μm , a banding pattern was still visible in the 60 and 25 μm phantoms, albeit faint. For this reason, MIL, LFD, and fractal analyses were again performed on regions cropped from μCT and DTS images. MIL.Max, MIL.DA, and MIL.SD decreased with plate thickness (Figure 35a). Of the aforementioned MIL parameters, MIL.Max and MIL.SD were moderately correlated to μCT MIL measurements ($R^2=0.68$ and 0.72 , respectively). Among the LFD parameters, LFD.Max, LFD.SD, and LFD.EllipseMax decreased monotonically with thickness down to 25 μm . Of these LFD parameters, LFD.Max, LFD.Av, LFD.SD, and LFD.EllipseMax were highly correlated with μCT LFD measurements ($R^2=0.97$, 0.97 , 0.95 , and 0.98 , respectively). Fractal dimension remained relatively constant while lacunarity decreased monotonically with thickness down to 25 μm . These findings suggest MIL, LFD and fractal analyses can detect

changes in feature thickness. However these changes in the measured parameters are of correlational nature with respect to the underlying structural changes at small resolutions.



(a)



(b)

Figure 34: a) FFT magnitude was highest when layers of thickness phantom were oriented perpendicular to the scanning direction and lower when layers were parallel. b) For the 0° angle scan, the FFT method was able to identify thickness accurately for 75-120 μm thickness phantoms, but 60 μm and below could not be resolved.

Aluminum grid panel phantom

All DTS images exhibited a varying degree of “halo” artifacts adjacent to the aluminum grid (Figure 36a, b). The gray value of the aluminum grid was shown as a valley as it exhibited a higher attenuation due to its higher density than air (Figure 36c). The location of this valley was used to determine the location of the grid and the amplitude was used to monitor signal variations in the DTS images.

All gray value profiles generated from measurements of 11 slices /stack in four orientations (0°, 15°, 22.5° and 45°) performed for both the L1 and L2 ROIs are plotted in Figure 37. Within each plot box in Figure 37, the 11 gray value distributions within each image slice stack overlap nearly perfectly along the x-axis (transverse distance from the center of image). These results indicate that there is no significant sliding of peak locations

between 0 mm to 11 mm along the z-axis (i.e., depth of grid panel) for L1 or L2 measurements. Furthermore the results revealed that, while most of the plot boxes show clear signals of peaks (gray value range: 100-20), signals at 0° performed poorly for the L2 orientation. This confirms results from spacing and thickness phantoms at the 90° (parallel) angle, indicating that DTS performs poorly in reconstructing structural features that are parallel to the scanning direction (also (Flynn et al., 2007)).

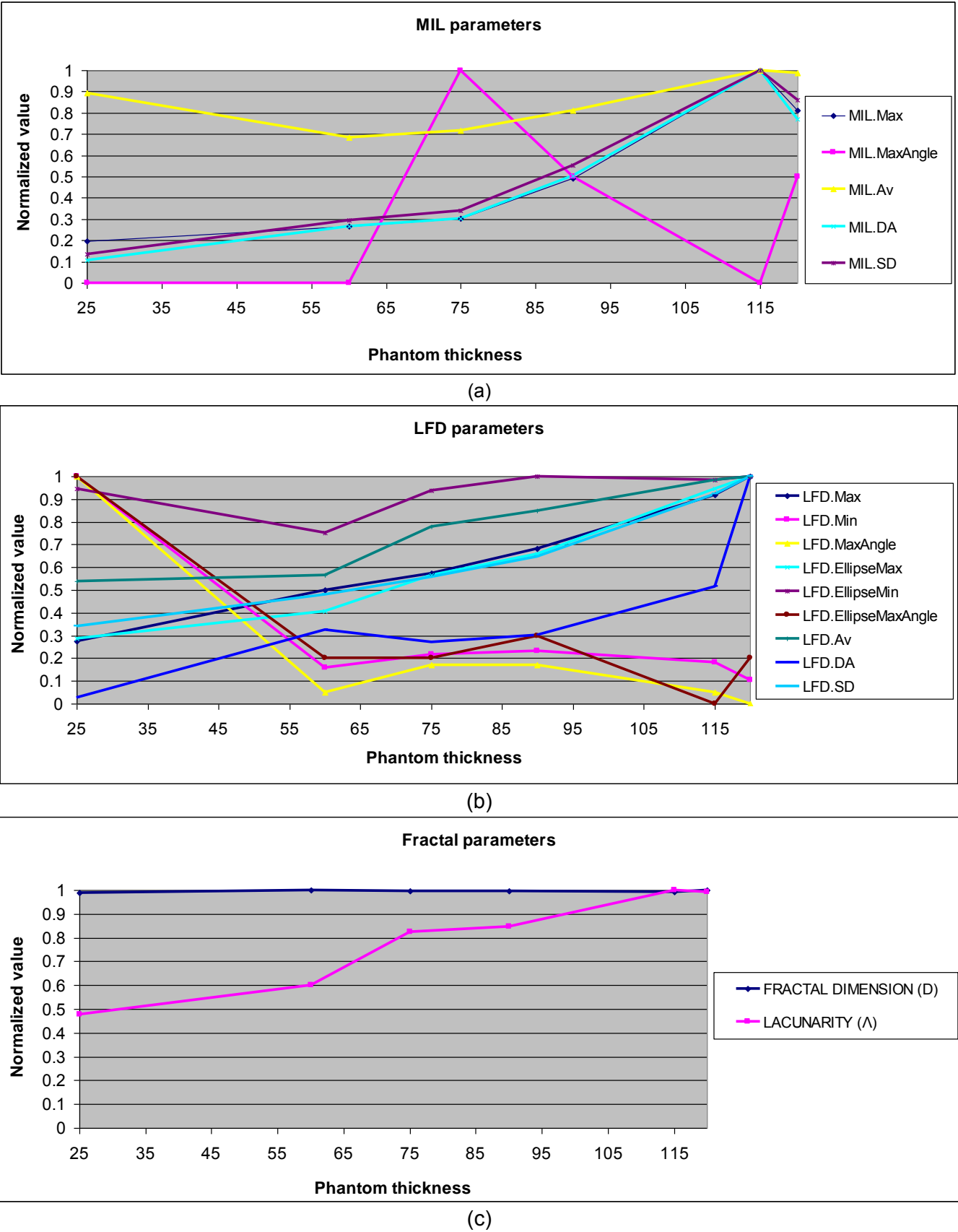
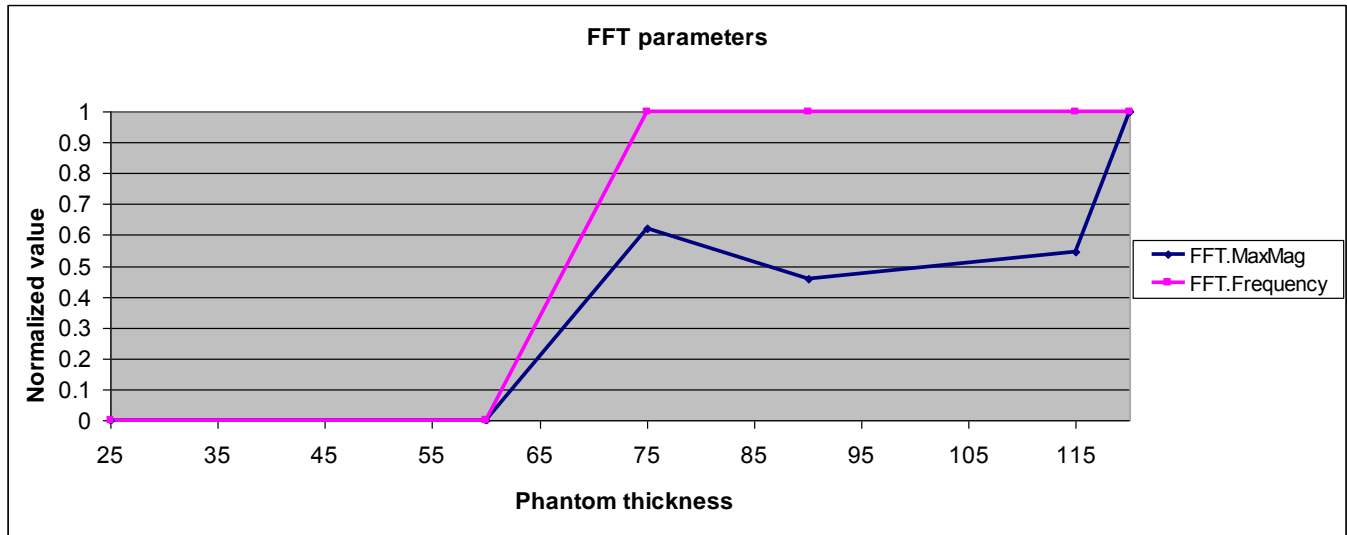


Figure 35

Figure 35 continued



(d)

Figure 35: The changes in morphometric parameters with varying phantom thickness as measured from DTS images. All parameters are normalized for comparison purposes. (a) MIL, (b) LFD, (c) fractal and (d) FFT parameters.

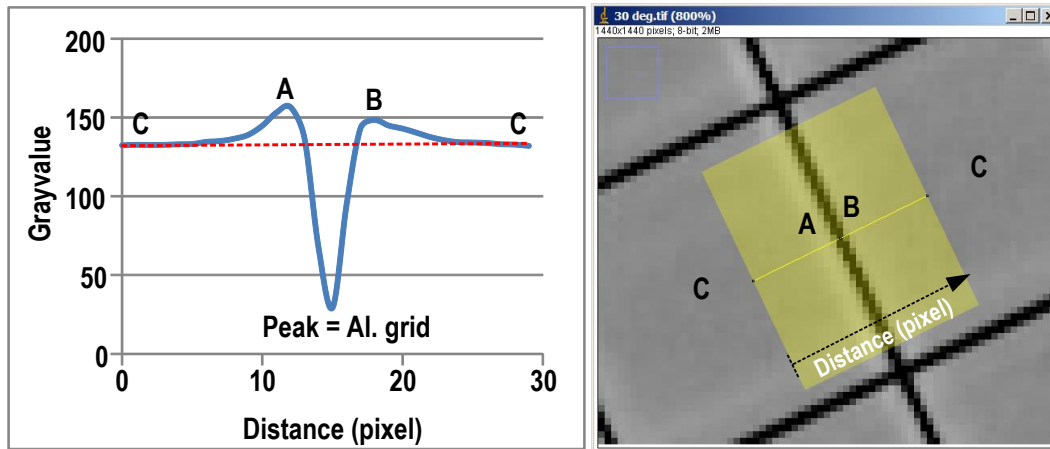


Figure 36: A typical gray value profile distribution in the ROI shown in yellow. The DTS image has a characteristic “halo” (A and B) reflecting a sudden change in density (i.e., air-to-aluminum). The halo has a slightly higher gray value (i.e., whiter). The air is marked as C.

Table 1 shows the mean and standard deviations of peak interval distances within each ROI. The table also confirms that there is a minimal variation of mean interval distance between grids within each ROI setting as well as among the eight orientations. The results indicate that there is no measurable distortion effect among two different measurement orientations (L1 vs. L2) as well as different scanning orientations (0°, 15°, 22.5° and 45°). This in turn assures that the dimension data obtained in DTS is likely to be reliable given that the subject geometry, structure and density characteristics are comparable to the aluminum grid used here.

Table 1: Mean and standard deviations of peak interval distances of different ROIs.

Orientation-ROI	0° L1	0° L2	15° L1	15° L2	22.5° L1	22.5° L2	45° L1	45° L2
No. grids in ROI (n)	20	17	19	17	17	17	18	16
Mean interval distance between two peaks (mm)	12.5	12.6	12.6	12.6	12.6	12.6	12.6	12.6
Standard deviation	0.14	0.14	0.14	0.14	0.14	0.14	0.14	0.14

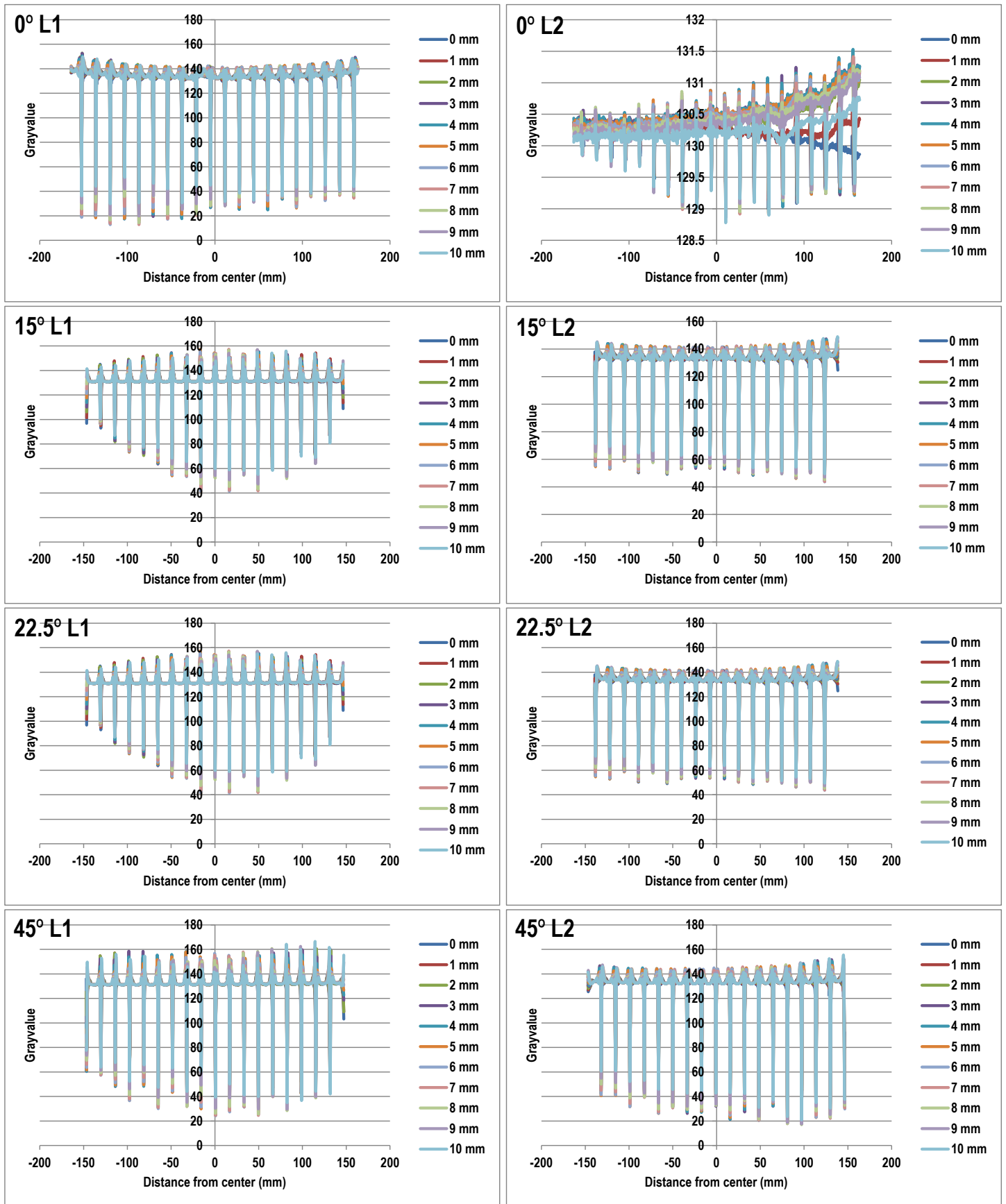


Figure 37: Gray value profile plots of L1 and L2 ROIs from 0°, 15°, 22.5° and 45° scanning orientation for the grid phantom. Note how all peak locations are near perfectly aligned between different slices within each ROI.

Mean peak values of 11 slices from each angular orientation ($n = 8$) were plotted in Figure 38. In general, the data indicate that the level of signal strength (gray value) is affected by i) angular orientation of the grid relative to the scan direction, ii) angle of measurements (L1 vs L2) within each scanning orientation and iii) distance

from the center of the scanning area.

While 0° L1 and 45° L1 generated highest signal levels, the signal from their L2 counterparts was much less; 0° L2 generated nearly no signal and 45° L2 generated approximately 40% less signal than that of 45° L1. The differences between L1 and L2 were reduced in 15° and 22.5° sets. Overall, the 22.5° scan performed best as L1 and L2 signals were, as a pair, relatively uniform across the distance from the center of the image and had comparable signal strength. The near-zero signal of 0° L2 confirms the previous observation that features that are parallel to the direction of tomographic acquisition are not well resolved in the final DTS image (also (Flynn et al., 2007)).

The signals varied as the distance from the center of the detector panel varied, for example from the left (-ve) to right (+ve), the signals of 45° L1, L2 and 22.5° L1 increased, 0° L1 decreased and 15° L2, 22.5° L2 formed a plateau at the center and their signals decreased at the edges of measurement area. In general scans performed in oblique orientations resulted in more uniform signals across the ROI.

Based on the results of the grid study, it is recommended that additional scans performed at 22.5° orientation should be explored for objects that contain both vertical and horizontal features such as vertebral bodies. Furthermore the finding that signal levels in the 22.5° scanning orientation are relatively uniform across the measuring area of 30 x 30 cm ($\pm 150\text{mm}$ as shown in Figure 38) supports this approach as this ROI is large enough to image six to eight levels of spine at once.

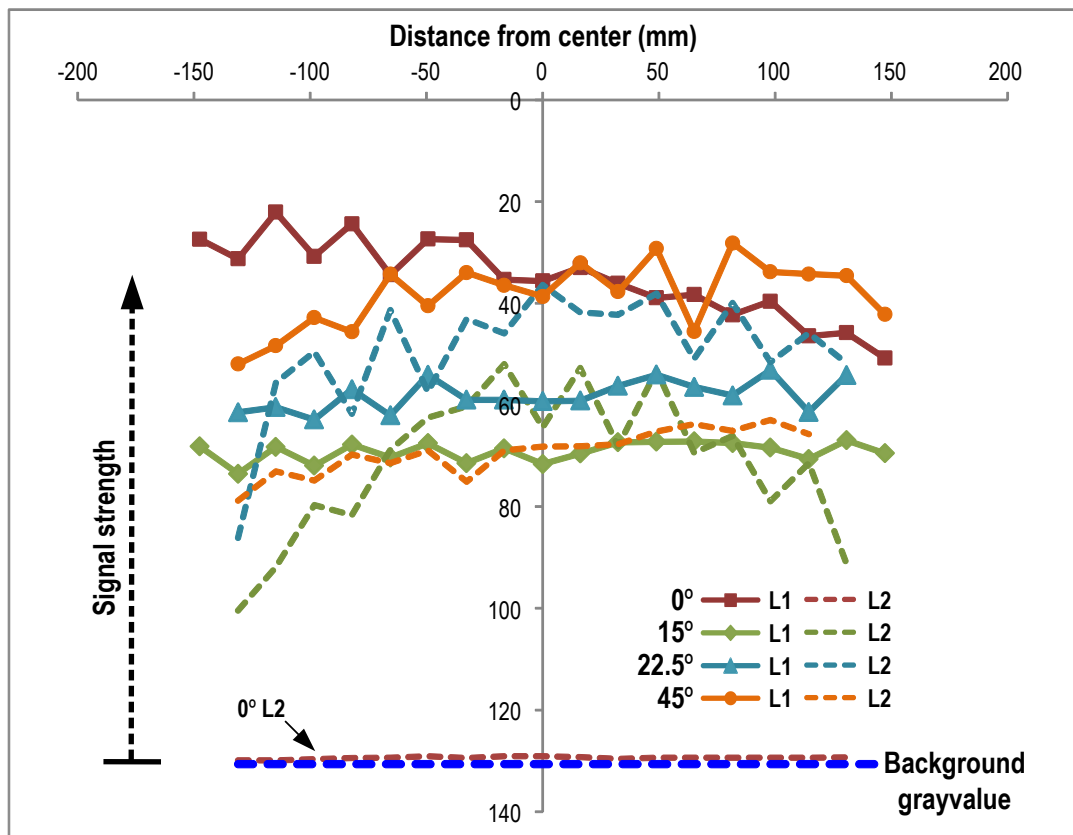


Figure 38: Mean peak gray value profiles of all ROI orientations. The plots are drawn upside down to show signal strength relative to the background signal (≈ 130 in blue).

Results from Tasks 3 and 4

Phase 1 Results

Relationship between μCT stereology and DTS (LFD, MIL and fractal) parameters:

Relationships were examined between μCT -derived and DTS-derived parameters of cancellous microstructure. The analysis consisted of mixed linear regression models between stereological parameters of μCT (BV/TV,

Tb.Th, Tb.N, Tb.Sp, DA) and DTS parameters (fractal, MIL and LFD). Mixed models were used in lieu of simple regression models to account for pseudoreplication in the data. Statistical analysis was carried using JMP 10 (Cary, NC).

MIL and LFD parameters calculated from the aggressively binarized (Bin.Ag) images had stronger and larger number of significant relationships with μ CT parameters than those from the unsharpened (USM) and conservatively binarized (Bin.Csv) methods (Table 2). This has resulted in no single filter method (i.e., USM, Bin.Csv, Bin.Ag) producing a complete set of DTS-derived fractal or morphometric parameters that correlated with all of the μ CT parameters tested. Fractal dimension and lacunarity slope parameters from fractal analysis also had strong relationships with μ CT parameters. However, mean lacunarity (λ) was not related to the μ CT parameters. Interestingly, neither the magnitude nor the heterogeneity of Tb.Sp (Tb.Sp.Av and Tb.Sp.SD, respectively) and heterogeneity of Tb.N (Tb.N.SD) were related to DTS parameters.

Table 2: Coefficients of determination (R^2) from mixed linear models where one μ CT parameter (columns) was the outcome and one DTS parameter (rows) was the effect variable. This table was constructed using mixed models instead of using simple correlations to account for pseudo-replication. Direction of the correlation coefficient (\uparrow for positive and \downarrow for negative relationships) and the p-value (in parenthesis) are given in each cell along with the R value. Only those models with $p < 0.05$ are shown.

	R^2 (p-value)	BVTV.Av	Tb.Th.Av	Tb.N.Av	Tb.Sp.Av	BVTV.SD	Tb.Th.SD	Tb.N.SD	Tb.Sp.SD	μ CT.DA
Fractal	FD		\downarrow 0.72 (<0.002)				\downarrow 0.65 (0.01)			
	λ									
	S_λ	\downarrow 0.89 (0.002)	\downarrow 0.83 (<0.0001)			\downarrow 0.82 (0.001)	\downarrow 0.77 (<0.0001)			
USM (Unsharp mask)	MIL.Max			\downarrow 0.93 (<0.02)	\uparrow 0.92 (0.03)					\uparrow 0.55 (0.03)
	MIL.DA									\uparrow 0.58 (0.01)
	MIL.Av			\downarrow 0.93 (0.006)	\uparrow 0.92 (0.01)					
	MIL.SD									\uparrow 0.57 (0.01)
	LFD.Max						\uparrow 0.67 (<0.009)			
	LFD.DA									
	LFD.Av			\downarrow 0.92 (0.03)			\uparrow 0.66 (0.009)			
	LFD.SD						\uparrow 0.66 (0.01)			
Bin.Csv (Conservative binarization)	MIL.Max		\uparrow 0.63 (0.03)							
	MIL.DA									\uparrow 0.58 (0.01)
	MIL.Av									
	MIL.SD									\uparrow 0.57 (<0.02)
	LFD.Max	\uparrow 0.88 (<0.02)	\uparrow 0.76 (<0.0001)				\uparrow 0.72 (<0.001)			
	LFD.DA									
	LFD.Av	\uparrow 0.88 (<0.02)	\uparrow 0.74 (0.0001)			\uparrow 0.77 (<0.04)	\uparrow 0.71 (<0.002)			
	LFD.SD		\uparrow 0.70 (<0.002)				\uparrow 0.65 (<0.02)			
Bin.Ag (Aggressive binarization)	MIL.Max									
	MIL.DA		\uparrow 0.59 (<0.03)				\uparrow 0.62 (0.03)			\uparrow 0.58 (<0.02)
	MIL.Av									

Table 2, continued.

MIL.SD				↑ 0.57 (<0.02)
LFD.Max	↑ 0.90 (<0.004)	↑ 0.79 (<0.0001)	↑ 0.80 (<0.02)	↑ 0.66 (0.01)
LFD.DA				
LFD.Av	↑ 0.88 (0.03)	↑ 0.73 (0.0008)		↑ 0.69 (0.003)
LFD.SD	↑ 0.89 (0.01)	↑ 0.71 (0.001)		

Relationship between μ CT (LFD, MIL and fractal) and DTS (LFD, MIL and fractal) parameters:

To examine the comparability between μ CT and DTS in terms of LFD-MIL parameters, linear regression analyses were performed between the MIL and LFD data extracted from DTS and μ CT at the same slice location. Because a single DTS slice represents a 1 mm layer while a slice from μ CT represents 0.045 mm, 20 μ CT slices were individually analyzed and then averaged to span the thickness represented in a DTS slice.

To account for the pseudo-replication effects, donor effect was treated as a random effect in the regression models (Table 3). Only MIL.Max, MIL.DA and MIL.SD of Bin.Csv and USM were significant ($p=0.006$ to $p=0.0427$). MIL.Max parameters had the highest explanatory power ($R^2_{adj} = 0.58$ and 0.591) followed by the MIL.SD parameters ($R^2_{adj} = 0.527$, 0.535).

Table 3: Summary of the relationships between μ CT-derived LFD, MIL and fractal parameters versus DTS-derived counterpart. Mixed regression models were used for the analysis. Only those with $p < 0.05$ are shown. For significant results, R^2_{adj} , coefficient, and p-value are reported below. Nonsignificant results are indicated by “-” and analysis types not applicable to a given variable are indicated by NA.

Y(μ CT) vs X (DTS)	Mixed univariate regression			
	Bin.Ag	Bin.Csv	USM	No processing
LFD.Max	-	-	-	NA
LFD.Av	-	-	-	NA
LFD.DA	-	-	-	NA
LFD.SD	-	-	-	NA
MIL.Max	-	0.580 8.653 (0.0427)	0.591 3.340 (0.0193)	NA
MIL.Av	-	-	-	NA
MIL.DA	-	0.296 0.770 (0.006)	0.302 0.541 (0.0477)	NA
MIL.SD	-	0.527 6.911 (0.0117)	0.535 3.584 (0.0115)	NA
FD	NA	NA	NA	-
λ	NA	NA	NA	-
S_λ	NA	NA	NA	-

While μ CT and DTS are fundamentally different in terms of acquisition and reconstruction methods, in this study, we have demonstrated that by use of the MIL method, there is a good degree of association between the two modalities. LFD and fractal parameters failed to correlate with μ CT parameters, which may be due to the fact that these two methods are more sensitive to the grayscale and binary representation of bone and non-bone phases. (The grayscale values of nonbone phases in μ CT are generally not useful.) Other possible reasons may be that the fact that while each DTS slice represented an integration of images over a 1 mm thick slice of bone, μ CT data was an average of 20 individually analyzed slices. This study thus motivates the use of

MIL in DTS images as parameters representative of true MIL properties. However, the slopes of regressions were greater than 1 indicating that DTS may have precision but lacks accuracy in MIL and may require further calibrations. The lack of an association between DTS derived and μ CT derived LFD parameters but presence of correlations between DTS derived LFD and μ CT derived non-LFD microstructural parameters indicate that LFD measurements contain information on the texture of cancellous bone structure but this information is of correlational nature and unlikely a true representation of the bone's LFD properties.

Relationship between image pre-processing and correlations between DTS parameters and FE-derived mechanical parameters:

The ability of DTS-derived parameters to predict bone stiffness and stress distribution properties (E_{FEM} , VMCV and $VMExp/\sigma_{app}$), was examined with and without BV/TV.Av in the regression equations. BV/TV.Av was introduced to the regression models to examine predictive capability of DTS parameters beyond that of BV/TV.Av alone, in which BV/TV.Av was treated as a surrogate measurement of bone mass (i.e., clinical BMD).

Statistical significance was set at $p < 0.05$. The multiple regression models were performed in a stepwise manner by eliminating parameters that exhibit multi-collinearity from the initial predictor set based on variance inflation factors ($VIF > 5$) and then eliminating parameters with nonsignificant effects ($p > 0.05$).

USM method:

DTS images processed using the USM method provided parameters that were comparable to bone mass in their ability to explain E_{FEM} and $VMExp/\sigma_{ap}$ but more explanatory than BV/TV alone for VMCV (Table 4). When used together with BV/TV.Av in multiregression models (simulating a situation where bone mass information is already available from another modality), addition of DTS-derived parameters contributed significantly to prediction of E_{FEM} and VMCV but not $VMExp/\sigma_{app}$: In addition to BV/TV, S_λ , LFD.Max, MIL.Av and MIL.DA significantly contributed to E_{FEM} and FD and MIL.DA to VMCV. (Figure 39)

Table 4: Summary of multiple regression models of BV/TV-only, DTS-only and DTS+BV/TV for the predictions of E_{FEM} , VMCV, $VMExp/\sigma_{app}$ using unsharp mask method (USM). The table cells for model terms include the variable name, estimates of the coefficient and p-values associated with that variable. Only those with $p < 0.05$ are shown.

USM Model		R^2_{adj}	μ CT Term	DTS Term 1	DTS Term 2	DTS Term 3	DTS Term 4	Intercept
E_{FEM}	BV/TV	0.82	BVTV.Av 1694 (<0.0001)					-61.91 (0.05)
	DTS	0.88		S_λ -2994 (<0.0001)	LFD.Max 1579 (<0.005)	MIL.Av -59.21 (<0.0009)	MIL.DA 247.8 (<0.0004)	-218.2 (0.03)
	BV/TV+DTS	0.93	BVTV.Av 1376 (<0.0001)	S_λ -1947 (<0.0001)	LFD.Max 1193 (<0.002)	MIL.Av -30.20 (0.005)	MIL.DA 148.0 (0.001)	-306.5 (<0.0001)
VMCV	BV/TV	0.57	BVTV.Av -1.3680 (0.005)					0.9867 (<0.0001)
	DTS	0.76		FD 1.247 (0.003)	LFD.Av 5.572 (<0.03)	LFD.SD -11.020 (0.01)	MIL.DA -0.2336 (<0.03)	-2.280 (0.04)
	BV/TV+DTS	0.71	BVTV.Av -1.277 (<0.003)	FD 0.9519 (<0.02)	LFD.Av - -	LFD.SD - -	MIL.DA -0.2770 (<0.01)	-1.199 (<0.3)
$VMExp/\sigma_{app}$	BV/TV	0.96	BVTV.Av -49.34 (<0.0001)					14.58 (<0.0001)
	DTS	0.94		S_λ 52.23 (0.0001)	MIL.Max 0.8621 (0.001)	MIL.DA -5.748 (<0.002)		14.94 (<0.0001)
	BV/TV+DTS	0.96	BVTV.Av -49.34 (<0.0001)	S_λ - -	MIL.Max - -	MIL.DA - -		14.58 (<0.0001)

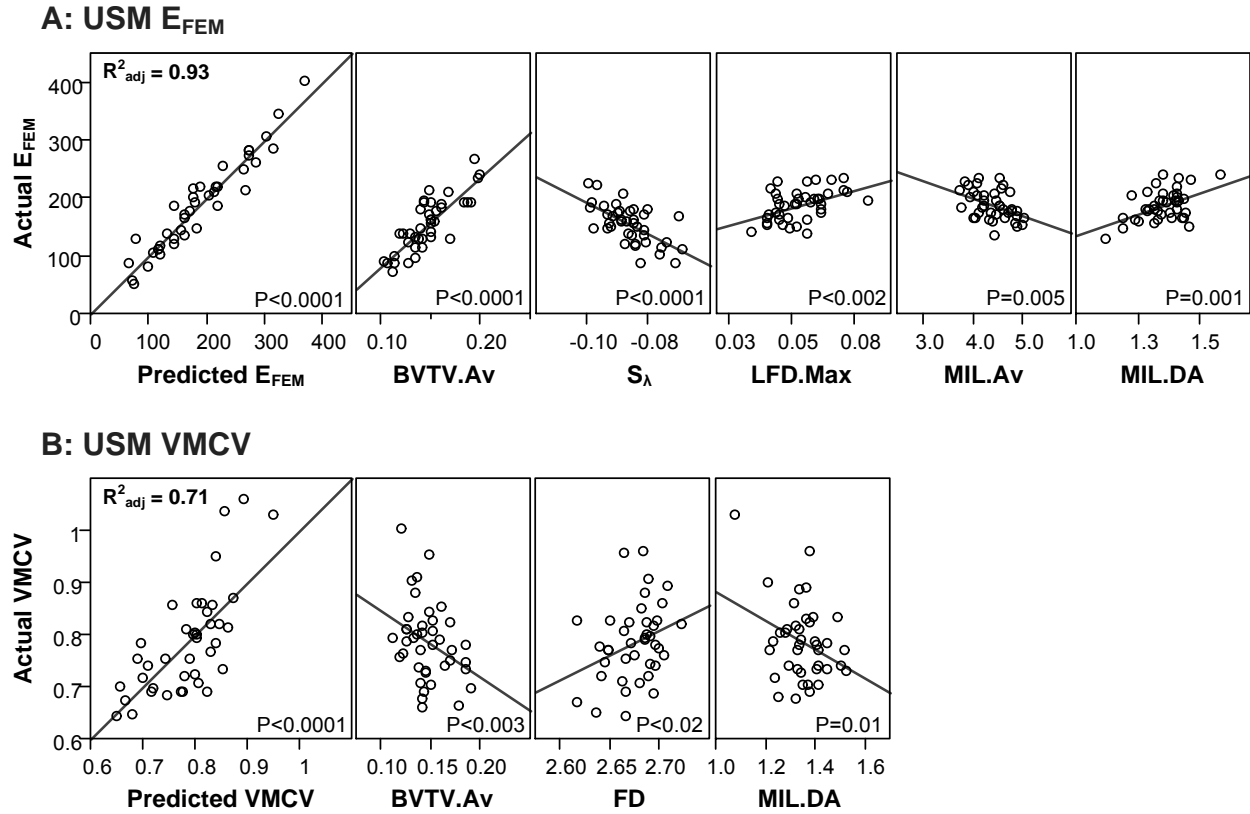


Figure 39: Multiple regression results from the unsharp mask (USM) processing method. Fit of the multiple regression models constructed using both BV/TV and DTS-based predictor variables and the leverage plots for the individual effects with the associated p-values for **(A)** E_{FEM} and **(B)** VMCV.

Bin.Csv method:

DTS images processed using the Bin.Csv method also provided parameters that were comparable to bone mass in their ability to explain E_{FEM} and $VMExp/\sigma_{ap}$ but more explanatory than BV/TV alone for VMCV (Table 5). When used together with BV/TV.Av in multiregression models (simulating a situation where bone mass information is already available from another modality), addition of DTS-derived parameters contributed significantly to prediction of E_{FEM} and VMCV but not $VMExp/\sigma_{app}$: In addition to BV/TV, S_λ and MIL.DA significantly contributed to E_{FEM} and VMCV. (Figure 40)

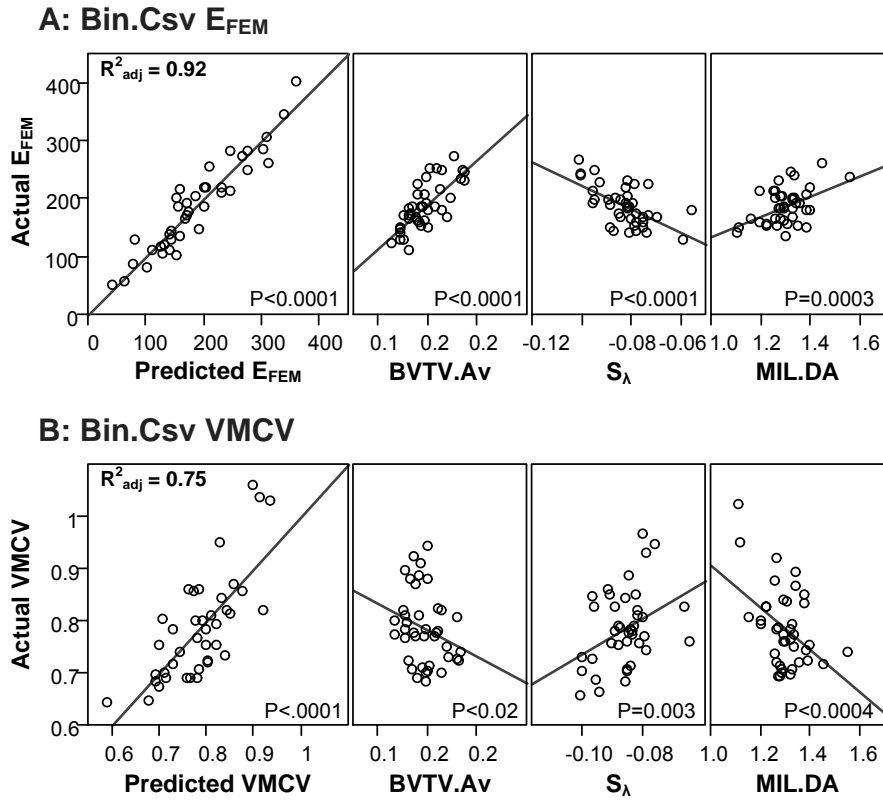


Figure 40: Multiple regression results from the conservatively binarized method (Bin.Csv). Fit of the multiple regression models constructed using both BV/TV and DTS-based predictor variables and the leverage plots for the individual effects with the associated p-values for **(A)** E_{FEM} and **(B)** VMCV.

Table 5: Summary of multiple regression models of BV/TV-only, DTS-only and DTS+BV/TV for predictions of E_{FEM} , VMCV, $VMExp/\sigma_{app}$ using conservatively binarized method (Bin.Csv). The table cells for model terms include the variable name, estimates of the coefficient and p-values associated with that variable. Only those with $p < 0.05$ are shown.

Bin.Csv Model	R^2_{adj}	μCT Term	DTS Term 1	DTS Term 2	Intercept
E_{FEM}	0.82	BVTV			
		BVTV.Av 1694 (<0.0001)			-61.91 (0.05)
		DTS	S_A -3294 (<0.0001)	MIL.DA 220.9 (<0.004)	-371.7 (<0.002)
	0.92	BVTV.Av 1534 (<0.0001)	S_A -2028 (<0.0001)	MIL.DA 175.0 (<0.0003)	-433.1 (<0.0001)
VMCV	0.57	BVTV			
		BVTV.Av -1.368 (0.005)			0.9867 (<0.0001)
		DTS	S_A 3.572 (<0.0002)	MIL.DA -0.4306 (<0.0003)	1.640 (<0.0001)
	0.75	BVTV.Av -1.015 (<0.02)	S_A 2.815 (0.003)	MIL.DA -0.4041 (<0.0004)	1.692 (<0.0001)
$VMExp/\sigma_{app}$	0.96	BVTV			
		BVTV.Av -49.34 (<0.0001)			14.58 (<0.0001)
		DTS	S_A 46.56 (0.001)		11.16 (<0.0001)
	0.96	BVTV.Av -49.34 (<0.0001)	S_A - -		14.58 (<0.0001)

Bin.Ag method:

DTS images processed using the Bin.Ag method, similar to other methods above, provided parameters that were comparable to bone mass in their ability to explain E_{FEM} and $VMExp/\sigma_{ap}$ but more explanatory than BV/TV alone for VMCV (Table 6). When used together with BV/TV.Av in multiregression models (simulating a situation where bone mass information is already available from another modality), addition of DTS-derived parameters contributed significantly to prediction of E_{FEM} and VMCV but not $VMExp/\sigma_{app}$: In addition to BV/TV, S_λ and LFD.SD significantly contributed to E_{FEM} and, MIL.DA to VMCV. In this case, there seems to be a large confounding effect of BV/TV on most significant DTS parameters such that inclusion of BV/TV is significantly worse than DTS alone. (Figure 41)

Table 6: Summary of multiple regression models of BV/TV-only, DTS-only and DTS+BV/TV for predictions of E_{FEM} , VMCV, $VMExp/\sigma_{app}$ using aggressively binarized method (Bin.Ag). The table cells for model terms include the variable name, estimates of the coefficient and p-values associated with that variable. Only those with $p < 0.05$ are shown.

Bin.Ag Model	R^2_{adj}	μCT Term	DTS Term 1	DTS Term 2	DTS Term 3	Intercept
E_{FEM}		BV/TV				
	0.82	BVTV.Av 1694 (<0.0001)				-61.91 (0.05)
	0.84		S_λ -2443 (0.0003)	LFD.SD 5853 (0.009)		-116.9 (0.03)
	0.89	BV/TV+DTS	BVTV.Av 1580 (<0.0001)	S_λ -1470 (0.002)	LFD.SD 3194 (0.009)	-222.4 (<0.0001)
VMCV		BV/TV				
	0.57	BVTV.Av -1.368 0.005				0.9867 (<0.0001)
	0.76		FD 0.9037 (<0.04)	MIL.DA -0.7169 (0.006)	MIL.SD 0.5414 (<0.03)	-0.8906 0.5
	0.68	BV/TV+DTS	BVTV.Av -1.404 (0.001)	FD - (0.001)	MIL.DA -0.2951 (0.001)	MIL.SD - - (<0.0001)
$VMExp/\sigma_{app}$		BV/TV				
	0.96	BVTV.Av -49.34 (<0.0001)				14.58 (<0.0001)
	0.93		S_λ 30.88 (<0.03)	LFD.DA 1.115 (0.01)	LFD.SD -144.8 (0.01)	10.06 (<0.0001)
	0.96	BV/TV+DTS	BVTV.Av -49.34 (<0.0001)	S_λ - -	LFD.DA - -	LFD.SD - - (<0.0001)

Even though it appears that DTS parameters calculated using the aggressive binarization (Bin.Ag) method had stronger and larger number of significant relationships with μCT parameters, DTS parameters calculated using the USM processing resulted in slightly better models of mechanical parameters than the other two processing methods. This may be because the two binarization methods produced parameters that are largely correlated to bone mass whereas the USM method produced parameters that contain heterogeneity information independent from bone mass (Table 2). The USM method is also a “grayscale” method which may correspond to the gray-level-based heterogeneous FE models better than the binarized images do.

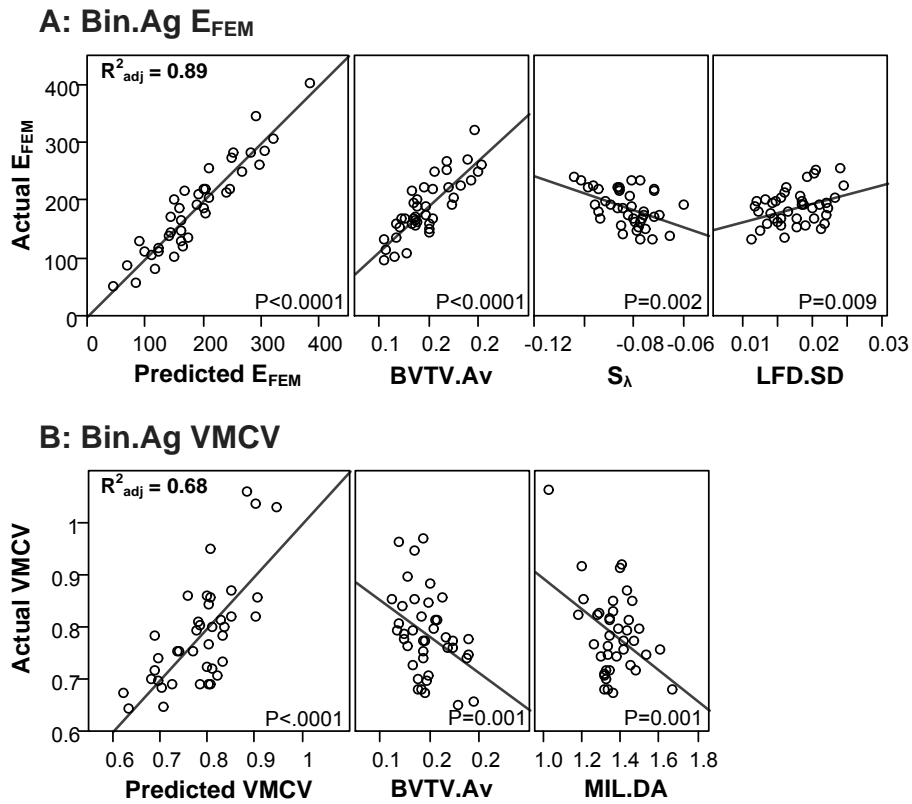


Figure 41: Multiple regression results from the aggressively binarized method (Bin.Ag). Fit of the multiple regression models constructed using both BV/TV and DTS-based predictor variables and the leverage plots for the individual effects with the associated p-values for **(A)** E_{FEM} and **(B)** VMCV.

Phase 2 Results

Relationship between μ CT stereology and stack-based DTS (LFD, MIL and fractal) parameters with varying scan orientation:

Mean (and standard deviation where appropriate) μ CT stereology parameters of bone volume fraction (BV/TV), trabecular thickness (Tb.Th), number (Tb.N), separation (Tb.Sp), and degree of anisotropy (DA), connectivity (Conn.Dn), fractal dimension (FD), structure model index (SMI) were correlated to stack-based DTS parameters (i.e., mean and standard deviations of MIL, LFD, and fractal parameters) calculated from six scanning orientations (AP and LM at angular (22.5°), parallel (0°) and perpendicular (90°)) using mixed regression models (Table 7).

Table 7: Summary of mixed regression models examining correlations between μ CT stereology parameters and DTS parameters. The DTS measurements used in these analyses were from the cuboidal VOIs as this type of VOI is most comparable to that used in μ CT analyses. Only those with $p < 0.05$ are shown. Models which are both significant in AP and LM are highlighted. AP = anterior posterior (coronal) view, LM = Lateral-medial (sagittal) view. Scan directions ang = angular (22.5°), par = parallel (0°), perp = perpendicular (90°) are with respect to the axis of the spine.

Y = μ CT	DTS			Mean (averaged within stack)			SD (intra-heterogeneity within stack)		
Stereology Parameter	View	Orientation	Parameter	R^2_{adj}	Coefficient sign	p-value	R^2_{adj}	Coefficient sign	p-value
BVTV.Av	AP	ang	MIL.Av	.	.	.	0.881	+	0.0067
			MIL.Max	.	.	.	0.883	+	0.0048
			MIL.SD	.	.	.	0.867	+	0.0422
	LM	perp	LFD.Av	0.870	+	0.0322	.	.	.
			LFD.Max	0.874	+	0.0215	.	.	.
			S_λ	.	.	.	0.867	+	0.0359

Table 7, continued.

BVTv.SD	AP	ang	MIL.Av	.	.	.	0.757	+	0.0464
			MIL.Max	.	.	.	0.758	+	0.0436
	LM	par	FD	.	.	.	0.760	+	0.0363
			LFD.Max	.	.	.	0.771	+	0.0195
Tb.Th.Av	AP	ang	MIL.Av	.	.	.	0.636	+	0.0237
			MIL.DA	0.621	+	0.0334	.	.	.
			MIL.Max	.	.	.	0.647	+	0.0155
			MIL.SD	.	.	.	0.661	+	0.0050
		perp	LFD.Av	0.634	+	0.0321	.	.	.
			LFD.Max	0.659	+	0.0096	.	.	.
			LFD.SD	0.618	+	0.0462	.	.	.
			MIL.DA	0.687	+	0.0016	0.558	+	0.0291
			MIL.SD	0.702	+	0.0026	.	.	.
	LM	ang	FD	.	.	.	0.581	+	0.0480
			MIL.DA	.	.	.	0.639	+	0.0046
		par	MIL.DA	0.624	-	0.0011	.	.	.
			MIL.SD	0.566	-	0.0440	.	.	.
		perp	LFD.Av	0.691	+	0.0020	.	.	.
			LFD.Max	0.705	+	0.0012	.	.	.
			LFD.SD	0.656	+	0.0118	.	.	.
			MIL.DA	0.705	+	0.0006	.	.	.
			MIL.SD	0.704	+	0.0022	.	.	.
Tb.Th.SD	AP	ang	S _A	0.629	-	0.0229	.	.	.
		par	LFD.DA	.	.	.	0.623	+	0.0360
			S _A	.	.	.	0.636	+	0.0201
		perp	LFD.Av	0.635	+	0.0286	.	.	.
			LFD.Max	0.680	+	0.0033	.	.	.
			LFD.SD	0.648	+	0.0117	.	.	.
			MIL.DA	0.743	+	0.0000	0.609	+	0.0069
			MIL.Max	0.656	+	0.0184	.	.	.
			MIL.SD	0.764	+	0.0000	0.667	+	0.0029
	LM	ang	MIL.DA	0.600	+	0.0202	0.603	+	0.0362
			S _A	0.626	-	0.0375	.	.	.
		par	LFD.DA	0.644	-	0.0192	.	.	.
			MIL.DA	0.627	-	0.0277	.	.	.
			S _A	0.613	-	0.0394	.	.	.
		perp	LFD.Av	0.656	+	0.0238	.	.	.
			LFD.Max	0.643	+	0.0348	.	.	.
			MIL.DA	0.772	+	0.0000	.	.	.
			MIL.SD	0.737	+	0.0003	.	.	.
Tb.N.Av	AP	ang	S _A	0.923	+	0.0210	0.929	+	0.0096
		par	S _A	0.927	+	0.0100	0.920	+	0.0499
	LM	ang	S _A	0.931	+	0.0044	.	.	.
		par	S _A	0.930	+	0.0044	.	.	.
Tb.N.SD	AP	ang	LFD.DA	.	.	.	0.735	+	0.0309
	LM	ang	LFD.Max	.	.	.	0.762	+	0.0173
			LFD.SD	.	.	.	0.768	+	0.0155
		par	LFD.Max	.	.	.	0.754	+	0.0206
			LFD.SD	.	.	.	0.753	+	0.0213
Tb.Sp.Av	AP	ang	LFD.Av	.	.	.	0.924	+	0.0173
			S _A	.	.	.	0.927	+	0.0085
		par	S _A	0.920	-	0.0207	.	.	.
	LM	ang	S _A	0.917	-	0.0439	.	.	.
		par	MIL.Av	0.917	+	0.0160	.	.	.
			MIL.Max	0.916	+	0.0200	.	.	.
Tb.Sp.SD	LM	ang	MIL.Av	0.870	+	0.0399	.	.	.
			S _A	.	.	.	0.878	+	0.0106
		par	MIL.Av	0.869	+	0.0359	0.869	+	0.0270
			MIL.Max	.	.	.	0.865	+	0.0388
		perp	MIL.Max	.	.	.	0.875	+	0.0186
			MIL.SD	.	.	.	0.884	+	0.0065
Conn.Dn.	AP	ang	FD	0.762	-	0.0203	.	.	.
			S _A	0.769	+	0.0065	0.756	+	0.0457
		par	FD	.	.	.	0.739	+	0.0439
			LFD.DA	.	.	.	0.742	+	0.0485
			LFD.Max	.	.	.	0.749	+	0.0232
			MIL.Max	.	.	.	0.733	+	0.0443
			MIL.SD	.	.	.	0.746	+	0.0164
			S _A	.	.	.	0.792	+	0.0021
		perp	MIL.DA	0.770	-	0.0049	.	.	.
			MIL.Max	0.741	-	0.0380	.	.	.
			MIL.SD	0.773	-	0.0036	.	.	.
	LM	ang	S _A	0.809	+	0.0006	0.749	+	0.0319

Table 7, continued.

		par	MIL.DA	0.771	+	0.0104	.	.	.
			S _λ	0.791	+	0.0011	.	.	.
		perp	LFD.DA	0.753	-	0.0430	.	.	.
			LFD.SD	.	.	.	0.754	+	0.0458
			MIL.DA	0.778	-	0.0053	.	.	.
			MIL.Max	0.769	-	0.0107	.	.	.
			MIL.SD	0.801	-	0.0009	.	.	.
			S _λ	0.738	+	0.0477	.	.	.
FD.Av	AP	ang	MIL.Av	.	.	.	0.893	+	0.0138
			MIL.Max	.	.	.	0.893	+	0.0134
	LM	ang	MIL.DA	.	.	.	0.887	+	0.0289
		perp	LFD.Av	0.887	+	0.0262	.	.	.
			LFD.Max	0.890	+	0.0194	.	.	.
			S _λ	.	.	.	0.885	+	0.0413
FD.SD	AP	ang	λ	0.764	+	0.0048	0.748	+	0.0105
		par	λ	0.743	+	0.0246	0.725	+	0.0441
			MIL.DA	0.745	+	0.0121	.	.	.
			MIL.Max	0.754	+	0.0424	.	.	.
			MIL.SD	0.763	+	0.0090	.	.	.
		perp	λ	.	.	.	0.711	+	0.0192
			LFD.DA	0.754	-	0.0147	0.768	+	0.0093
			LFD.Max	0.717	-	0.0228	.	.	.
			LFD.SD	0.726	-	0.0233	.	.	.
			S _λ	0.738	+	0.0144	.	.	.
	LM	ang	FD	.	.	.	0.766	+	0.0011
			λ	0.751	+	0.0182	0.757	+	0.0047
			LFD.Av	.	.	.	0.754	+	0.0273
		par	FD	.	.	.	0.727	+	0.0170
			λ	0.773	+	0.0040	0.761	+	0.0027
			MIL.DA	0.846	+	0.0000	0.787	+	0.0005
			MIL.SD	0.771	+	0.0056	0.761	+	0.0040
			S _λ	.	.	.	0.713	+	0.0390
		perp	FD	.	.	.	0.715	+	0.0380
			LFD.Av	0.699	-	0.0130	.	.	.
			LFD.Max	0.708	-	0.0061	.	.	.
			LFD.SD	0.717	-	0.0352	.	.	.
			MIL.Av	0.749	-	0.0106	.	.	.
			MIL.DA	0.735	-	0.0430	.	.	.
			MIL.Max	0.765	-	0.0031	.	.	.
			MIL.SD	0.773	-	0.0015	.	.	.
			S _λ	0.739	+	0.0105	.	.	.
mean MIL	AP	ang	MIL.Av	.	.	.	0.648	+	0.0002
			MIL.Max	.	.	.	0.647	+	0.0002
			MIL.SD	.	.	.	0.540	+	0.0066
SD MIL	AP	perp	S _λ	0.402	+	0.0302	.	.	.
	LM	ang	LFD.Av	0.411	+	0.0341	.	.	.
			LFD.Max	0.404	+	0.0361	.	.	.
			LFD.SD	0.400	+	0.0269	.	.	.
		par	LFD.Av	0.520	+	0.0041	0.346	+	0.0234
			LFD.DA	0.346	+	0.0445	0.394	+	0.0178
			LFD.Max	0.479	+	0.0092	.	.	.
			LFD.SD	0.484	+	0.0036	.	.	.
		perp	S _λ	0.398	+	0.0283	.	.	.
SMI	LM	perp	LFD.Av	0.943	-	0.0151	.	.	.
			LFD.DA	0.940	-	0.0394	.	.	.
			LFD.Max	0.945	-	0.0094	.	.	.
			LFD.SD	0.945	-	0.0096	.	.	.

A number of significant correlations were found between μ CT and DTS variables. In general, perpendicular scans in the LM view provided significant correlates for a greater number of μ CT parameter than other scans. As suggested by the phantom studies of Task 2, it is possible that the perpendicular scans are better for examining the vertically aligned trabeculae while parallel scans are better for examining the horizontally aligned trabeculae. While the perpendicular scans in an LM view appear to be the preferable single scan configuration, it is likely that scans in multiple orientations will provide complementary information. This is most notable for the cases of Tb.N.Av, Tb.Sp.Av and Tb.Sp.SD where parallel scans provided significant correlates but perpendicular scans did not. Overall, the results support the idea that DTS can provide quantitative information on the cancellous bone microstructure and possibly can contribute towards the prediction of bone strength.

Relationship between vertebral fracture strength and DTS (LFD, MIL and fractal) parameters with varying scan orientation and VOI method:

We found several significant correlations between vertebral fracture strength and DTS-derived cancellous bone parameters (Table 8). The adaptive VOI method, which allows for examination of a larger volume of cancellous bone, produced a higher number of significant models with 1 to 3% higher explained variability compared to the other VOI methods. Overall, analysis of the image stack provided more explanatory information than the analysis of a single slice.

Table 8: Summary of significant ($p < 0.05$) relationships between peak fracture force and (A) mean(DTS) and (B) SD(DTS) parameters as assessed by mixed linear regression. The results are grouped by slice/stack, ROI-VOI methods and scanning orientations. For ease of interpretation, the μ CT parameters that are associated with the DTS parameter under question are presented in the “Correlates to μ CT” column. AP = anterior posterior coronal plane, LM = Lateral-medial sagittal plane, ang = angular (22.5°), par = parallel (0°), perp = perpendicular (90°).

(A) Mean (DTS)				Slice			Stack					
				Largest ROI			Cuboidal VOI			Adaptive VOI		
View	Orientation	DTS Parameter	Correlates to μ CT	R^2_{adj}	Coeff.	p-value	R^2_{adj}	Coeff.	p-value	R^2_{adj}	Coeff.	p-value
AP	ang	S_A	Tb.Th.SD, Tb.N.Av, Conn.Dn	0.415	30530	0.050
	perp	LFD.Max	FD.SD	0.456	-66932	0.044
		LFD.SD	FD.SD	0.453	-293629	0.032
		MIL.DA	Tb.Th.Av, Conn.Dn.	0.461	-2423	0.048
		MIL.Max	Conn.Dn.	.	.	.	0.467	-606	0.030	0.478	-638	0.019
		MIL.SD	Conn.Dn.	.	.	.	0.504	-3191	0.014	0.514	-3471	0.009
LM	ang	S_A	Tb.Th.SD, Tb.N.Av, Conn.Dn	0.437	31260	0.024
	par	S_A	Tb.N.Av	0.389	30278	0.040
	perp	LFD.Av	Tb.Th.Av	0.509	-129171	0.009	0.459	-137404	0.041	0.489	-153525	0.020
		LFD.Max	FD.SD	.	.	.	0.475	-77805	0.031	0.490	-85184	0.026
		LFD.SD	FD.SD	.	.	.	0.455	-275525	0.024	0.448	-283332	0.028
		MIL.DA	Tb.Th.Av, Conn.Dn.	.	.	.	0.479	-3485	0.044	0.484	-3634	0.041
		MIL.Max	Conn.Dn.	.	.	.	0.427	-429	0.025	0.458	-496	0.011
		MIL.SD	Conn.Dn.	.	.	.	0.490	-2949	0.007	0.511	-3050	0.005

(B) SD (DTS)				Stack								
				Cuboidal VOI			Adaptive VOI					
View	Orientation	DTS Parameter	Correlates to μ CT	R^2_{adj}	Coeff.	p-value	R^2_{adj}	Coeff.	p-value			
AP	perp	LFD.Max	FD.SD	.	.	.	0.444	-151319	0.043			
		LFD.SD	FD.SD	.	.	.	0.477	-633858	0.016			
		MIL.Max	Conn.Dn.	.	.	.	0.458	-990	0.029			
LM	perp	MIL.Max	Conn.Dn.	0.321	-895.212	0.037	0.316	-1561	0.007			
		MIL.SD	Conn.Dn.	0.276	-6436.189	0.032	0.330	-7256	0.031			

Multiple regression models constructed using DTS parameters from the adaptive VOI approach indicated that using a combination of variables measured from a single DTS configuration, the prediction strength for vertebral fracture force can be substantially increased (up to 86%) (Table 9).

Models from the perpendicular scanning orientations had greater explanatory capability for vertebral strength than did the parallel or angular scans. Parameters of vertebral size (width and height) were significant and addition of a vertebral size parameter in the model increased explanatory capability of the model for six scanning configurations. The model with the highest explanatory capability was for the AP/perpendicular configuration. The addition of vertebral size into the models changed the composition of predictors in the model for most cases. However, three out of the four predictor parameters persisted up on addition of vertebral size in to the AP/perpendicular model, indicating some level of robustness for these predictors.

The study thus demonstrates mixed multiple regression models of DTS parameters can predict fracture strength of vertebral bone where the best scanning orientation is anterior-posterior with DTS acquisition motion perpendicular to the torso. We have observed that vertebral size itself is a significant contributor to fracture strength and further improves the predictability by 5 to 28%.

Table 9: Summary of the mixed multiple regression models for peak vertebral fracture force with and without height and width data measured from DTS images. Each cell shows R^2_{adj} followed by the predictor(s) in the model (p-value). Only those with $p < 0.05$ are shown.

View	Orientation	DTS parameters only	DTS parameters + size
AP (Anterior-posterior coronal plane)	Angular (23°)	0.653 Av(F.S _A) (0.0168) SD(LFD.SD) (0.0018) SD(F.S _A) (0.0260) Av(MIL.SD) (0.0405)	0.755 AP Height (<0.0001) SD(LFD.SD) (0.0002) Av(MIL.Max) (0.0357)
	Parallel (0°)	0.503 SD(MIL.DA) (0.0032) Av(MIL.DA) (0.0431)	0.712 AP Height (<0.0001) SD(MIL.DA) (0.0102)
	Perpendicular (90°)	0.814* Av(MIL.SD) (<0.0001) SD(MIL.DA) (<0.0001) Av(MIL.Av) (0.0028) SD(LFD.SD) (0.0090)	0.860* AP Height (0.0006) Av(MIL.SD) (<0.0001) SD(MIL.DA) (<0.0001) Av(MIL.Av) (0.0015) SD(MIL.Max) (0.0346)
LM (Lateral-medial sagittal plane)	Angular (23°)	0.437 Av(F.S _A)(0.0243)	0.669 LM Height (<0.0001)
	Parallel (0°)	0.389 Av(F.S _A) (<0.0398)	0.669 LM Height (<0.0001)
	Perpendicular (90°)	0.511 Av(MIL.SD) (0.0045)	0.713 LM Height (<0.0001) SD(LFD.Av) (0.0141)

KEY RESEARCH ACCOMPLISHMENTS

We produced strong evidence that the “concept” being explored, i.e., that quantitative analysis of bone quality using DTS is feasible.

We characterized the DTS imaging system and identified its ability to resolve features under different operational parameters.

We determined the potential of the DTS system for quantification of density.

We established methods to be used for quantitative analysis from DTS images of vertebral bone.

To the best of our knowledge, this is the first demonstration that correlates of conventionally used parameters of cancellous bone microstructure can be derived from quantitative analysis of bone texture from DTS images.

We demonstrated that parameters of cancellous bone microstructure derived from DTS increases accuracy in prediction of cancellous bone stiffness.

We demonstrated that parameters of cancellous bone microstructure and vertebral geometry derived from DTS increases accuracy in prediction of vertebral strength.

We have identified that AP-perpendicular scanning orientation may provide optimum DTS parameters for prediction of bone fracture strength.

We designed and fabricated an innovative, cost-effective apparatus that can apply multiaxial “wedge” loads using the capability of a conventional uniaxial materials testing system.

REPORTABLE OUTCOMES

Manuscripts

Kim, W., Oravec, D., Nekkanty, S., Yerramshetty, J., Sander, E., Divine, G. W., Flynn, M. J. and Yeni, Y. N., “Digital tomosynthesis (DTS) for quantitative assessment of trabecular microstructure in human vertebral bone”
Manuscript in preparation to be submitted to Spine. Final draft is under review by the PI.

Xiao, A. and Yang, E. “Topographical Measurements of Vertebral Endplate to Predict Bone Fragility: Comparison of Digital Tomosynthesis and High Resolution Computed Tomography with Microcomputed Tomography”. September 27, 2013.

Report submitted by summer research students to the 2013 Siemens Competition in Math, Science & Technology.

Abstracts

Kim, W., Oravec, D., Sander, E., Divine, G. W., Flynn, M. J. and Yeni, Y. N., "Digital Tomosynthesis-Derived Microstructural Parameters Predict Cancellous Bone Stiffness in Human Vertebrae". 59th Annual Meeting of the Orthopaedic Research Society, San Antonio, Texas. (2013). Poster 0701.

Kim, W., Oravec, Divine, G. W., Flynn, M. J. and Yeni, Y. N., " Digital Tomosynthesis of Human Vertebral Bone: The Effect of Positioning and Scan Orientation on Prediction of Cancellous Bone Stiffness."

Conference abstract submitted to the 60th Annual Meeting, Orthopaedic Research Society, March 15-18, 2014, New Orleans, Louisiana.

Kim, W., Oravec, Divine, G. W., Maatman, T, Flynn, M. J. and Yeni, Y. N., "Digital Tomosynthesis for Prediction of Human Whole Vertebral Stiffness"

Conference abstract submitted to the 60th Annual Meeting, Orthopaedic Research Society, March 15-18, 2014, New Orleans, Louisiana.

Presentations

Structural and Microstructural Considerations in Vertebral Bone Fragility, Wayne State University, Department of Biomedical Engineering, February 23, 2012.

Invited seminar as a part of a graduate class: BME seminar class (BME 8070).

Deciphering trabecular microstructure using digital tomosynthesis (DTS), Bone and Joint Center Seminar Series, Henry Ford Hospital, August 3, 2012.

Institutional level seminar.

Assessing fracture risk in osteoporotic spine using DTS – scanning orientation effects explored, Bone and Joint Center Seminar Series, Henry Ford Hospital, June 7, 2013.

Institutional level seminar.

Funding applied for based on work supported by this award

April, 2012: "Novel Digital Tomosynthesis and Noncoding RNA Approaches to Predict Progression of Osteoarthritis"

FY12 DOD CDMRP Peer Reviewed Medical Research Program Investigator Initiated Award

Role on grant: Principal Investigator (MPI: Gibson)

The proposed project was based on the methods developed for analysis of bone quality from DTS images and the encouraging results obtained from vertebral bone. However, we were not invited to submit a full application.

Tomosynthesis for assessment of hip bone quality and fracture strength

National Institutes of Health (R21)

Requested Award period: 1/1/2014 - 12/31/2015

Role on grant: Principal Investigator

This is an exploratory project to examine the feasibility of DTS for assessment of hip bone quality and fracture risk. The methods developed for analysis of bone quality from DTS images and the encouraging results obtained from vertebral bone during the current award support feasibility of the proposed work. However, as we learned during this award, scan configuration and analysis methods can be critical for a successful application to the hip and these may not be the same as for the spine. Therefore, there is merit in conducting research to explore feasibility and optimize methodologies for this problem. This proposal is currently pending review.

Tomosynthesis of the human spine in vivo for assessment of vertebral bone quality

National Institutes of Health (R01)

Requested Award period: 4/1/2014 - 3/31/2019

Role on grant: Principal Investigator

Having established feasibility and developed methods to measure vertebral bone, we prepared this proposal to examine the in vivo feasibility of the approach. We will examine subjects with a prevalent vertebral fracture and subjects with primary hyperparathyroidism (pHPT) as test cases representing increased fracture risk but with different bone microstructural/structural factors involved. These groups will be compared to normal controls (without fracture or pHPT) and the ability of DTS to discriminate among these groups will be examined and compared to BMD from DEXA, serum and urine biomarkers of bone turnover, bone remodeling dynamics as determined from iliac biopsies and high resolution microstructural analysis of iliac bone. This proposal will be submitted by November 12, 2013.

Employment or research opportunities applied for and/or received based on experience/training supported by this award

This project provided training opportunities for the following individuals whether or not they were compensated by the project funds:

1. Woong Kim, PhD: University of Auckland, New Zealand, Post-doc fellow, 2012 – present.
Scanning and analysis methods for DTS imaging of vertebral bone.
2. Richard Banglmaier, PhD: Wayne State University, Senior Research Engineer, 2011 – April 2013.
Nonuniform mechanical testing of vertebral bone.
3. Daniel Oravec, MSc: Tampere University of Technology, Finland, Research Engineer, 2011 – present
All aspects of the project.
4. Ryan Bylsma, Student, Wayne State University, School of Medicine, October 2011 – January 2012.
Micro-CT scanning of bone
5. Mary Nixon, Student, Wayne State University, School of Medicine, May 2012 – July 2012.
Image processing and analysis.
6. Justin Schupbach, Student, Wayne State University, School of Medicine, June 2012 – July 2012.
Image processing and analysis.

7. Kaitlin McLoughlin, Student, Wayne State University, School of Medicine, August 2012 – September 2012.
Stereologic analysis of cancellous bone.
8. Kalyan Sreeram, Student, Wayne State University, School of Medicine, August 2012 – April 2013.
Image processing and analysis.
9. Thomas K Maatman, Student, Wayne State University, School of Medicine, August 2012 – May 2013.
Micro-CT scanning of bone, bone phantoms and image analysis. Finite element modeling.
10. Nicole Ramo, Student, Kettering University, Biomedical Engr., Winter 2011, Spring 2012.
Micro-CT image analysis. Specimen preparation.
11. Jason Bagnall, Student, Oakland Community College, Engineering, March – August 2012.
Micro-CT image processing. Stereologic analysis of cancellous bone.
12. Vincent Giacomelli, Student, Harrison High School, Farmington, MI, June 18 – August 10, 2012.
DTS image processing, LFD analysis of cancellous bone images.
13. Toufic Jildeh, Student, Wayne State University, School of Medicine, May 2013 – September 2013.
DTS and radiographic image processing and analysis.
14. Joy Zhang, Student, Detroit Country Day High School, Beverly Hills, MI, June 10 – August 9, 2013.
Micro-CT image processing. Stereologic analysis of cancellous bone.
15. Angela Xiao, Student, Troy High School, Troy, MI, June 17 – September 30, 2013.
Micro-CT and DTS image processing and analysis.
16. Ellen Yang, Student, Troy High School, Troy, MI, July 17 – September 30, 2013.
Micro-CT and DTS image processing and analysis.
17. Matthew Varga, Student, Wayne State University, BMS Masters Program, June 2013 – present
Image processing and analysis.
18. Omaina Bokhari, Student, Wayne State University, School of Medicine, Year 4, August 2013 – present.
DTS image processing and analysis.

CONCLUSION

DTS generated images analyzed by fractal, MIL and LFD methods provided good to excellent predictions of in vitro vertebral trabecular bone stiffness and whole vertebral strength. This technique could augment the current clinical imaging modalities (DEXA and CT) to increase the prediction accuracy of the fracture risk in patients.

Future work is planned to adapt the tomosynthesis reconstruction techniques to multipurpose imaging systems so as to achieve multidirectional DTS scan capabilities in vivo and extend the feasibility studies to clinical experiments where the ability of DTS to predict fracture risk will be examined using clinical cohorts known to be at high risk, such as those with prevalent fractures or metabolic bone disease. Comparison of DTS with other clinically available modalities such as DEXA and CT are also planned.

REFERENCES

- Buckley, J. M., Cheng, L., Loo, K., Slyfield, C. and Xu, Z. (2007). "Quantitative computed tomography-based predictions of vertebral strength in anterior bending." *Spine* 32(9): 1019-1027.
- Fazzalari, N. L. and Parkinson, I. H. (1996). "Fractal dimension and architecture of trabecular bone." *J Pathol* 178(1): 100-105.
- Flynn, M. J., McGee, R. and Blechinger, J. (2007). Spatial resolution of x-ray tomosynthesis in relation to computed tomography for coronal/sagittal images of the knee, San Diego, CA, United states, Progress in Biomedical Optics and Imaging - Proceedings of SPIE, SPIE, 6510: 65100D-65109.

- Geraets, W. G. (1998). "Comparison of two methods for measuring orientation." *Bone* 23(4): 383-388.
- Goulet, R. W., Goldstein, S. A., Ciarelli, M. J., Kuhn, J. L., Brown, M. B. and Feldkamp, L. A. (1994). "The relationship between the structural and orthogonal compressive properties of trabecular bone." *J Biomech* 27(4): 375-389.
- Hou, F. J., Lang, S. M., Hoshaw, S. J., Reimann, D. A. and Fyhrie, D. P. (1998). "Human vertebral body apparent and hard tissue stiffness." *J Biomech* 31(11): 1009-1015.
- Kalidindi, S. R., Abusafieh, A. and El-Danaf, E. (1997). "Accurate Characterization of Machine Compliance for Simple Compression Testing." *Experimental Mechanics* 37(2): 210-215.
- Karperien, A. (2007). "FracLac for ImageJ, version 2.5.
<http://rsb.info.nih.gov/ij/plugins/fractalac/FLHelp/Introduction.htm>. 1999-2007."
- Kim, D. G., Christopherson, G. T., Dong, X. N., Fyhrie, D. P. and Yeni, Y. N. (2004). "The effect of microcomputed tomography scanning and reconstruction voxel size on the accuracy of stereological measurements in human cancellous bone." *Bone* 35(6): 1375-1382.
- Kinds, M. B., Bartels, L. W., Marijnissen, A. C., Vincken, K. L., Viergever, M. A., Lafeber, F. P. and de Jong, H. W. (2011). "Feasibility of bone density evaluation using plain digital radiography." *Osteoarthritis Cartilage* 19(11): 1343-1348.
- Kuhn, J. L., Goldstein, S. A., Feldkamp, L. A., Goulet, R. W. and Jesion, G. (1990). "Evaluation of a microcomputed tomography system to study trabecular bone structure." *J Orthop Res* 8(6): 833-842.
- McDonnell, P., Harrison, N. and McHugh, P. E. (2010). "Investigation of the failure behaviour of vertebral trabecular architectures under uni-axial compression and wedge action loading conditions." *Med Eng Phys* 32(6): 569-576.
- Nekkanty, S., Yerramshetty, J., Kim, D. G., Zauel, R., Johnson, E., Cody, D. D. and Yeni, Y. N. (2010). "Stiffness of the endplate boundary layer and endplate surface topography are associated with brittleness of human whole vertebral bodies." *Bone* 47(4): 783-789.
- Plotnick, R. E., Gardner, R. H., Hargrove, W. W., Prestegard, K. and Perlmutter, M. (1996). "Lacunarity analysis: A general technique for the analysis of spatial patterns." *PHYSICAL REVIEW E* 53(5): 5461-5468.
- Reimann, D. A., Hames, S. M., Flynn, M. J. and Fyhrie, D. P. (1997). "A cone beam computed tomography system for true 3D imaging of specimens." *Appl Radiat Isot* 48(10-12): 1433-1436.
- Sander, E. A. and Barocas, V. H. (2009). "Comparison of 2D fiber network orientation measurement methods." *J Biomed Mater Res A* 88(2): 322-331.
- Whealan, K. M., Kwak, S. D., Tedrow, J. R., Inoue, K. and Snyder, B. D. (2000). "Noninvasive imaging predicts failure load of the spine with simulated osteolytic defects." *J Bone Joint Surg Am* 82(9): 1240-1251.
- Yeni, Y. N., Christopherson, G. T., Dong, X. N., Kim, D. G. and Fyhrie, D. P. (2005). "Effect of microcomputed tomography voxel size on the finite element model accuracy for human cancellous bone." *J Biomech Eng* 127(1): 1-8.
- Yeni, Y. N. and Fyhrie, D. P. (2001). "Finite element calculated uniaxial apparent stiffness is a consistent predictor of uniaxial apparent strength in human vertebral cancellous bone tested with different boundary conditions." *J Biomech* 34(12): 1649-1654.
- Yeni, Y. N., Zinno, M. J., Yerramshetty, J. S., Zauel, R. and Fyhrie, D. P. (2011). "Variability of trabecular microstructure is age-, gender-, race- and anatomic site-dependent and affects stiffness and stress distribution properties of human vertebral cancellous bone." *Bone* 49(4): 886-894.

APPENDICES

Appendix 1:

Kim, W., Oravec, D., Sander, E., Divine, G. W., Flynn, M. J. and Yeni, Y. N., "Digital Tomosynthesis-Derived Microstructural Parameters Predict Cancellous Bone Stiffness in Human Vertebrae". 59th Annual Meeting of the Orthopaedic Research Society, San Antonio, Texas. (2013). Poster 0701.

Appendix 2:

Xiao, A. and Yang, E. "Topographical Measurements of Vertebral Endplate to Predict Bone Fragility: Comparison of Digital Tomosynthesis and High Resolution Computed Tomography with Microcomputed Tomography". September 27, 2013.

Report submitted by summer research students to the 2013 Siemens Competition in Math, Science & Technology.

Appendix 3:

Kim, W., Oravec, Divine, G. W., Flynn, M. J. and Yeni, Y. N., " Digital Tomosynthesis of Human Vertebral Bone: The Effect of Positioning and Scan Orientation on Prediction of Cancellous Bone Stiffness."

Conference abstract submitted to the 60th Annual Meeting, Orthopaedic Research Society, March 15-18, 2014, New Orleans, Louisiana.

Appendix 4:

Kim, W., Oravec, Divine, G. W., Maatman, T, Flynn, M. J. and Yeni, Y. N., "Digital Tomosynthesis for Prediction of Human Whole Vertebral Stiffness"

Conference abstract submitted to the 60th Annual Meeting, Orthopaedic Research Society, March 15-18, 2014, New Orleans, Louisiana.

Digital Tomosynthesis-Derived Microstructural Parameters Predict Cancellous Bone Stiffness in Human Vertebrae

Kim, Woong¹; Oravec, Daniel¹; Sander, Edward²; Divine, George W¹; Flynn, Michael J¹; Yeni, Yener N¹

1. Bone and Joint Center, Henry Ford Hospital, Detroit, MI, United States.
2. Dept of Biomedical Engineering, The University of Iowa, Iowa City, IA, United States.

Introduction: Clinical modalities currently available for the assessment of fracture risk in the spine largely rely on the bone mineral density (BMD) measurements; however their ability to provide information on the trabecular structure is limited. Digital tomosynthesis (DTS) is a relatively new imaging modality that has many advantages over the conventional CT and radiography, where DTS can generate multiple image slices with superior in-plane resolution than that of CT but with only 1/6th of the radiation. Nekkanty et al. have recently reported that fractal dimension (FD) as measured from DTS images of human vertebrae is correlated to stereologic measures of cancellous microstructure obtained from μ -CT images [1]. Also they have shown that FD could be used to predict the compressive stress state in the microstructure. The objectives of this study was to investigate if the MIL (mean intercept length) and LFD (line fraction deviation [2]) parameters of DTS images obtained from human vertebrae could i) be correlated to the μ -CT stereological parameters and ii) predict trabecular bone stiffness, independent from bone volume fraction.

Methods: T6, T8, T11, and L3 vertebrae from 5 female and 5 male cadavers (age 63-90yr) were μ -CT scanned and reconstructed at 45 μ m voxel size. In each trabecular bone region, mean (Av) and standard deviation (SD) of the bone volume fraction (BV/TV), trabecular thickness (Tb.Th), number (Tb.N), and separation (Tb.Sp), and degree of anisotropy (DA) were calculated. Cancellous bone apparent modulus (E) was calculated from a finite element (FE) simulation of inferior-superior compression [3]. The same bones were scanned using DTS (Shimadzu Sonalvision Safire II) and reconstructed. In each image set, the coronal central slice was used for MIL and LFD analyses (**Fig 1**). Mean (Av), standard deviation (SD), maximum (Max) and degree of anisotropy (DA) were recorded (MIL.DA = ellipse fitted Max/Min and LFD.DA = Raw Max/LFD orthogonal to Max). Mixed model regressions of μ -CT parameters to DTS parameters were examined (**Table 1**). Multi regression models were constructed to examine the relationship of MIL and LFD parameters with E with and without BV/TV. In all regression models, the donor variable was included as a random effect to account for pseudo-replication.

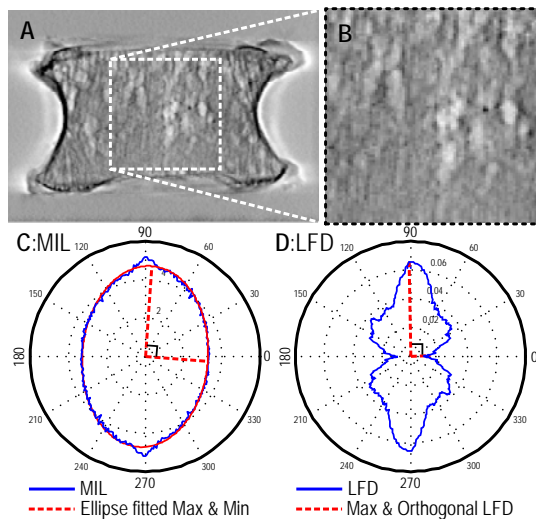


Figure 1 – [A] Coronal view of DTS image of a L3 vertebra and [B] region analyzed with [C] MIL (mean intercept length) and [D] LFD (line fraction deviation) methods. The overall alignment of MIL and LFD plots corresponds to that of the trabecular texture. Dotted red lines mark vectors of ellipse fitted max and min MIL in [C], and max LFD and orthogonal to the maximum LFD in [D].

Results: MIL.Max, MIL.DA, MIL.SD, LFD.Max and LFD.Av from DTS were significantly related with Tb.Th.Av, BV/TV.SD, Tb.Th.SD, Tb.N.SD and DA from the μ -CT stereological parameters (**Table 1**, $p < 0.001$ to $p < 0.05$). DTS parameters were significant in multiple regression models of E after accounting for BV/TV (**Fig 2**). Multiple regression models of E using DTS parameters alone (MIL.DA + MIL.Av + LFD.Max) were as predictive as BV/TV alone ($R^2_{adj} = 0.832$ vs. 0.819 respectively).

R (p-value)	MIL.Max	MIL.DA	MIL.SD	LFD.Max	LFD.Av
Tb.Th.Av		+0.82 (0.01)	+0.83 (0.01)	+0.77 (0.04)	+0.77 (0.02)
BV/TV.SD	-0.86 (0.02)				
Tb.Th.SD		+0.87 (<0.001)	+0.86 (<0.001)		+0.81 (0.03)
Tb.N.SD	-0.86 (<0.001)	-0.86 (0.01)	-0.86 (<0.001)		
DA		+0.75 (0.02)	+0.73 (0.05)		

Table 1– R of mixed linear regression of μ -CT (rows) against DTS parameters (columns). Only those with $p < 0.05$ are shown.

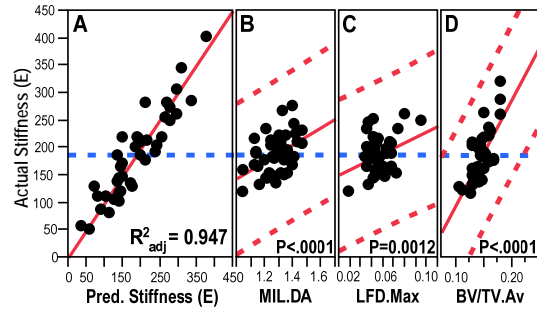


Figure 2 – [A] Actual vs. predicted stiffness plot of the multi regression model based on both DTS and BV/TV parameters. [B, C, D] The regression model's leverage plots for the individual effects (MIL.DA, LFD.Max and BV/TV.Av) with the associated p-values. The results show that stiffness prediction with the model is excellent ($R^2_{adj} = 0.947$).

Discussion: We demonstrated that correlates of the standard μ -CT stereological parameters can be obtained from DTS images using MIL and LFD methods. Also we were able to demonstrate that DTS images can be used to predict stiffness of human vertebral bone. In fact, DTS derived model performed equally well as the BV/TV-only model indicating that DTS alone is potentially as powerful a tool as those measuring BMD for predicting vertebral stiffness. When BV/TV.Av (a surrogate of bone mass) and DTS parameters were combined, the explained variability in E increased from 82% to 95%, suggesting that DTS contains trabecular structural information that is independent of BV/TV.Av and therefore it could be used as a complementary modality to DEXA and tomographic BMD measures. This in turn opens an exciting possibility that DTS can be used, not only as a qualitative imaging tool, but as a quantitative tool to assess bone fracture risk while subjecting patients with a relatively low radiation. Because cancellous bone stiffness is a strong correlate of bone strength, we expect that these methods will perform equally well for predicting bone strength. However, it remains to be determined to what extent DTS derived parameters can predict whole bone strength and fracture risk in vivo.

Significance: DTS generated images analyzed by MIL and LFD methods provided good to excellent predictions of in vitro vertebral trabecular bone stiffness and thus this technique could augment the current clinical imaging modalities (DXA and CT) to increase the prediction accuracy of the fracture risk in patients.

Acknowledgements: DOD PRMRP W81XWH-11-1-0769 and NIH AR059329.

References: [1] Nekkanty et al., 2011, 57th ORS, p. 670. [2] Geraets, W. 1998, Bone, 23(4): p. 383-388. [3] Yeni et al, 2011, Bone, 49: 886-94.

2013 Siemens Competition

Math : Science : Technology

Supplemental Form

(Please save to your hard drive, type in answers and print. Make three copies and attach one to each copy of your Research Project.)

STUDENT INFORMATION

Name of Individual or Team Leader:	Angela Xiao
Names of Parents of Individual or Team Leader:	Steve Xiao, Kathy Jin
Name of Individual's or Team Leader's High School:	Troy High School
High School City and State:	Troy, MI
Name of Team Member 2:	Ellen Yang
Names of Parents of Team Member 2:	George Yang, Mei Li
Name of Team Member 3:	
Names of Parents of Team Member 3:	
Research Project Title:	Topographical Measurements of Vertebral Endplate to Predict Bone Fragility: Comparison of Digital Tomosynthesis and High Resolution Computed Tomography with Microcomputed Tomography
Project Type:	<input type="checkbox"/> Individual <input checked="" type="checkbox"/> Two-person team <input type="checkbox"/> Three-person team

PUBLICATIONS

Has this research project been published, accepted, or submitted for publication?	<input type="checkbox"/> YES - published <input type="checkbox"/> YES - accepted <input type="checkbox"/> YES - submitted <input checked="" type="checkbox"/> NO
If YES, please name the journal(s)	

ACKNOWLEDGEMENTS

You must acknowledge all individuals who assisted or advised you in any way (i.e. mentor, teacher, family members, lab assistants, other students). Please include the person's name, title, and institution and describe their participation/contribution. You are required to complete the Acknowledgements section and must include the name, title, institution, and role of any individuals who assisted with the Research Project, including family members. Receiving assistance from family members does not affect the judging in any way, but you must acknowledge their support. **Failure to identify others who assisted you with any aspect of your research may result in disqualification.**

Name, Title, Institution, Participation/Contribution
<i>SAMPLE - Dr. John Smith, Professor of Biology, Sample University, Assisted with the collection of data</i>
Dr. Yener Yeni, Head of Biomechanics Section, Henry Ford Hospital, Provided project outlines Daniel Oravec, Research Engineer, Henry Ford Hospital, Assisted with collection of data, students were provided background information and extensive training on the use of ImageJ and application of established protocols for endplate topography measurement. Provided outline for interpretation of statistical results and contributed toward discussion.

Additionally, please identify the institutions (i.e. laboratory, university, etc.) where you performed your research, if not already acknowledged above.

Institution	City	State
Henry Ford Health System	Detroit	MI

Topographical Measurements of Vertebral Endplate to Predict Bone Fragility: Comparison of Digital Tomosynthesis and High Resolution Computed Tomography with Microcomputed Tomography

ABSTRACT

Bone mineral density measurements help determine strength of human vertebral bodies and their fracture potential, but BMD alone is not the most accurate predictor. Research indicates that surface topography measurements of vertebral endplates can increase the accuracy in assessment of bone fragility. Thus, to maximize prediction accuracy, clinical measurements with little radiation that include superior and inferior endplates would be useful. Our objective was to investigate the feasibility of measuring endplate topography using clinically available imaging methods: High resolution computed tomography (HRCT) and digital tomosynthesis (DTS), a scan with a small rotation angle that yields images of limited field depth, were examined in comparison with micro computed tomography (μ CT), the current gold standard for scanning non-living specimens. Topographical endplate measurements were recorded; five statistical parameters (average, standard deviation, coefficient of variation, kurtosis, and skewness) were calculated for each set of scans. After statistical analysis, a significant correlation was found in all parameters between DTS and μ CT, and HRCT and μ CT for the superior endplate. This demonstrates that DTS, a scan with double the resolution of CT scans in the plane of endplate measurement and less radiation exposure, is a potentially viable approach to quantify endplate topography in a clinical setting.

EXECUTIVE SUMMARY

Osteoporosis is a progressive disease where bone becomes more porous and less dense, making it weaker and more prone to breakage. It affects 9 million Americans putting them all at a risk of severe bone fracture. There are two major types of bone: cancellous bone is the inner, softer portion of the bone, and cortical bone is the outer, harder layer of bone. Areas with a higher ratio of cancellous bone to cortical bone such as the spine are closely associated with increased fracture risk, because cancellous bone undergoes turnover (removal and replacement of old bone) at a faster rate than cortical bone does. Vertebral endplates are composed of a layer of thickened cancellous bone, so increased osteoclast activity (removal of bone tissue) can result in endplate abnormality and dysfunction. Vertebral fractures can be detected based on the presence of endplate deformities and a lack of parallelism of endplates. Thus, to increase accuracy of diagnosis and reduce risk of fracture, scans should include superior and inferior portions of vertebral endplate. We investigated three types of scans: microcomputed tomography (μ CT), high resolution computed tomography (HRCT), and digital tomosynthesis (DTS); of the three, DTS administers the smallest radiation dose (1/5 that of HRCT). μ CT has the highest resolution, but is not feasible for clinical use due to high radiation, so it is used only as a standard of comparison for the other two scans, both of which have been approved for clinical use. In our study, a set of 117 vertebral bones were scanned using each of the three scanning mechanisms. Endplate topography measurements were statistically analyzed for each set and five parameters were calculated (average, standard deviation, coefficient of variation, kurtosis, and skewness). A correlation was discovered between both DTS and HRCT in relation to μ CT for the superior endplate. Because of this, we can infer that DTS is a potential alternative in predicting bone fracture, because of its accuracy in endplate topography measurement and its low radiation dose.

Topographical Measurements of Vertebral Endplate to Predict Bone Fragility: Comparison of Digital Tomosynthesis and High Resolution Computed Tomography with Microcomputed Tomography

I. INTRODUCTION

Osteoporosis is a bone disease that progresses silently, often with few symptoms; as time goes on, the risk of fracture significantly increases. Identifying and treating patients at risk of fracture can substantially reduce the long term burden of osteoporosis, reducing the risk of first fracture from 8% to 2% can reduce the 5-year fracture incidence from approximately 34% to 10% (Lindsay et al, 2005). Bone mineral density (BMD) is commonly used in assessment of bone quality and fracture risk (Cranney et al. 2007), but taken alone, BMD may not be the best single determinant of whole bone mechanical properties (Cheng et al., 1997; Singer et al., 1995).

Recent studies have shown that topographical features of human vertebral body endplates are associated with vertebral bone mechanical properties and may be important determinants of bone fragility (Eswaran et al., 2007; Langrana et al., 2006; Nekkanty et al., 2010). Nekkanty et al. found that kurtosis of the endplate topography statistical distribution, which captures topographical features such as peaks or deep valleys, are significantly correlated at the inferior endplate with finite element-derived mechanical parameters such as work to fracture, displacement at maximum load, and strain to maximum load. In such studies of bone microstructure, microcomputed tomography (μ CT) is typically used as a gold standard as it provides a high resolution 3-dimensional depiction of bone microarchitecture. However, μ CT is only suitable in a laboratory setting with in vitro specimens due to size limitations and high

radiation dose. To date, the use of clinical imaging modalities in assessment of endplate topography has not been studied.

Computed tomography (CT) is used clinically in assessment of bone structure, but in-plane reconstructed pixel size is typically on the order of 0.3-1 mm with a resolution of approximately 1 mm (Thornton et al, 2006). Recent advances in flat panel digital detectors have realized a technology called digital tomosynthesis (DTS), a scan that administers a significantly lower dose of radiation while maintaining high in plane resolution. Digital tomosynthesis is a tomographic imaging modality in which a series of projection images are acquired over a limited arc, with the x-ray source pivoting and translating opposite the direction of a flat panel detector encased in the scanning bed. DTS delivers approximately 1/5 the dose of CT and provides good resolution of cancellous texture and cortical bone geometry (Kim et al., 2013, Nekkanty et al., 2011). Tomosynthesis reconstructions are formed in the lateral-medial or anterior-posterior direction, in contrast with CT which produces an axial image with high slice thickness along the superior-inferior direction. Topographic features of the endplate surface are thus captured in-plane with a pixel size of approximately 0.3 mm in DTS, rather than out-of-plane with 0.75 mm slice thickness in an axial HRCT image.

In this study, endplate topography measurements of digital tomosynthesis (DTS) and high resolution computed tomography (HRCT) were compared to similar measurements from μ CT in order to assess the viability of endplate topography measurement in a clinical imaging modality. Due to better in-plane resolution of the vertebral endplate, we hypothesized that endplate

characteristics measured from tomosynthesis images would be better correlated with μ CT than measurements from HRCT (Figure 1).

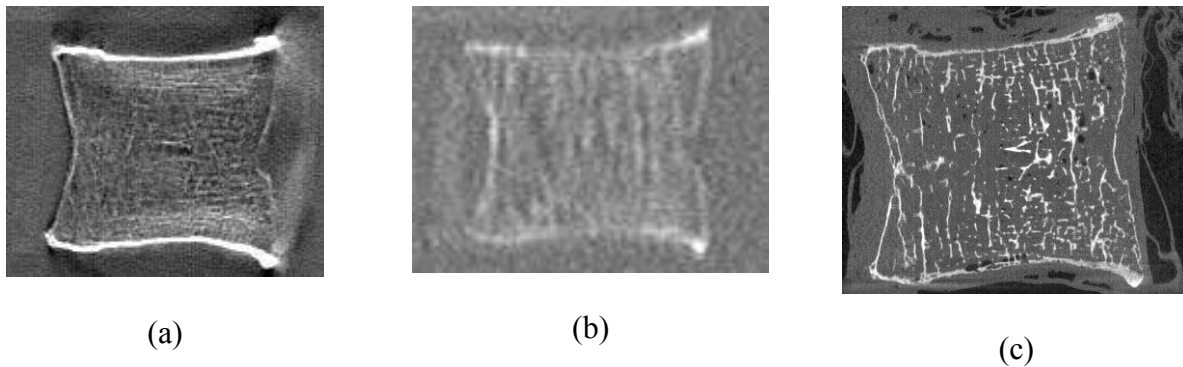


Figure 1: Comparison of images taken from sagittal plane in similar regions from (a) DTS, (b) HRCT, and (c) μ CT. Images are resized to show detail at comparable scale.

II. METHODS

2.1 Subjects

Human cadaveric thoraco-lumbar spines were acquired under local IRB approval from tissue banks, and four vertebral bodies (T10, T11, T12, L1) were harvested from 42 donors of varying gender and age. Donors with HIV, hepatitis or infectious diseases, cause of death involving trauma or a history of spine surgery, glucocorticoid use, or metabolic diseases known to affect bone were not included. Vertebral bodies were dissected, soft tissue and posterior elements were removed, and specimens were stored wrapped in saline-soaked gauze at -20° C until scanning was performed. The donor set consisted of 23 men and 19 women all between the ages of 36 and 100. Collectively, the vertebrae of these donors formed a set of 117 bones.

2.2 HRCT, DTS, and μ CT Scanning Procedures

Specimens were mounted and consistently aligned in a custom radiolucent scanning tank filled with 0.9% saline and scanned using DTS (Shimadzu Sonialvision Safire II) and high resolution CT (Siemens Sensation 64) (Figure 2). Alignment was ensured using a radiolucent clamping system such that the anterior-posterior and lateral-medial anatomical directions corresponded to the reconstruction x and y axes, respectively. The same specimens were scanned using a custom-built μ CT system and reconstructed at an isotropic voxel size of 40 micrometers. The μ CT system used in the study was home built based on the hardware, data acquisition, and reconstruction methods of the μ CT system have been previously described (Reimann et al., 1997). The presently operating system uses a Kevex 16-watt x-ray source with a 9-micron focal spot, a 1888x1408-pixel Varian PaxScan 2520 flat panel digital x-ray detector with 127-micron pitch, a Newport precision rotational stage, and control software running under Windows XP.



(a)



(b)



(c)

Figure 2: Vertebral bodies were mounted to trays via a precise clamping system contained within radiolucent boxes filled with saline. Boxes were scanned in digital tomosynthesis (a) and computed tomography systems (b). The same vertebral bodies were positioned in a radiolucent cylinder and scanned using microcomputed tomography (c).

2.3 HRCT, DTS, and μ CT Data Collection

For HRCT images, a single threshold value in Hounsfield Units was manually determined as the minimum value that delineates bone from soft tissue. The threshold value was used in a custom segmentation algorithm within an in-house image processing suite which produced a binarized volume (Zael et al., 2006). After thresholding, the disconnected voxels within the volume were removed via a continuity check algorithm. Volume masks separating cortical and cancellous bone were segmented using a previously-described semi-automatic method (Oravec et al., 2012, Buie et al. 2007). The segmentation algorithm consists of dilating the binarized vertebral image twice (closing porosity within and on the surface of the vertebra), applying a median filter (connecting surfaces and smoothing processing artifacts), and eroding back twice. The resulting volume, a solid mask image of the whole vertebral body, was further cropped into separate volumes representing superior and inferior endplates. TopoJ (Hovis, 2013), a plugin written for ImageJ (Rasband, 1997-2013), was used to analyze the topography of superior and inferior endplates separately. TopoJ calculates a 2D height map, with each pixel in the map representing the depth from a fixed plane (the first slice) of the first encounter of bone along the superior-inferior axis. The depth distribution (background and holes were eliminated from the analysis) was recorded into a text file in which each row represented a single pixel in 2D height map. Distribution statistics such as average (AV), standard deviation (SD), coefficient of variation (CV), skewness (Skew), and kurtosis (Kurt) were calculated from HRCT depth measurements.

A similar process was performed for DTS images. A global threshold value was manually determined to delineate bone from soft tissue and air. Due to a blurring effect in the highest and

lowest slices of the DTS reconstructions, a central substack of 25 slices (25 mm) was created and the image was binarized in ImageJ using the recorded threshold value. Binarized images were cropped into separate volumes representing superior and inferior endplates. TopoJ was again used to calculate depth distributions for DTS endplate images. The same distribution statistics were calculated from DTS depth measurements.

Threshold values for μ CT reconstructions were calculated from a 300x300x300 voxel central cube of cancellous bone using the Otsu method in ImageJ and the image was binarized using this global threshold value. A custom algorithm was used to produce a depth frequency distribution representing distances from the superior-most and inferior-most reference planes to the inner surfaces of the vertebral endplate. The same distribution statistics were calculated using the depth frequency distribution produced by this method for μ CT.

2.3 Statistical analysis

The main interest was in the relationship between similar measurements from the μ CT and DTS images and between those from the μ CT and high resolution CT (HRCT) images as determined using regression models. The analysis started with examination of interactions between vertebral level and the predictor of interest. Mixed models were constructed using one of μ CT variables as the outcome, the corresponding DTS or HRCT variable, vertebral level and the interaction of the latter two as the effect variables. The model also included a random subject variable to account for pseudoreplication due to using multiple vertebral levels from some subjects. If a significant interaction was found, the data were split by vertebral level and a separate simple regression analysis was performed between the μ CT and the DTS (or HRCT) variable. Nonsignificant

interaction terms were removed and the models were rerun with the main effects until no nonsignificant effect was present. If the data could be pooled through this elimination procedure and a significant positive relationship remained between the endplate variables from the two methods, such measurements were deemed most successful.

Paired t-tests were also run to assess differences in mean of statistical distribution parameters between superior and inferior endplates. All analyses were performed in JMP (SAS Institute Inc., Cary, NC).

III. RESULTS

Statistical Results are summarized in Table 1. Mixed models indicated significant interactions between μ CT and DTS for superior SD ($p<0.03$) and skewness ($p<0.02$), as well as between μ CT and HRCT for inferior AV ($p<0.05$). When vertebrae were separated by level, significant positive correlations were found for DTS superior SD and skewness at all four levels (T10, T11, T12, and L1), so the levels were pooled in a unified mixed model in which both SD and skewness were found to be significant ($p<0.0001$, $R^2_{Adj}=0.21$; $p<0.0001$, $R^2_{Adj}=0.53$). When separated by level, HRCT average for inferior endplate was significant only for T10-T12.

At the inferior endplate, only significant level effects were seen in DTS skewness ($p<0.04$) and HRCT kurtosis ($p<0.03$) and skewness ($p<0.04$). Neither level nor variable were significant for models of superior DTS CV ($p>0.3$) and inferior CT SD ($p>0.3$) and CV ($p>0.08$).

In the case that both variable and level were found to be significant, mixed models were rerun removing level as an effect. Superior DTS CV was significant without level ($p<0.0001$, $R^2_{Adj}=0.17$), as was HRCT SD ($p<0.0001$, $R^2_{Adj}=0.19$) and inferior DTS kurtosis ($p<0.02$, $R^2_{Adj}=0.03$). Variables which remained significant following the elimination procedure (no significant interaction or level effects) were superior DTS AV ($p<0.0001$, $R^2_{Adj}=0.21$) and kurtosis ($p<0.0001$, $R^2_{Adj}=0.25$), superior HRCT AV ($p<0.0001$, $R^2_{Adj}=0.37$), CV ($p<0.0001$, $R^2_{Adj}=0.41$), skewness ($p<0.002$, $R^2_{Adj}=0.58$) and kurtosis ($p<0.0007$, $R^2_{Adj}=0.41$), and inferior DTS AV ($p<0.0001$, $R^2_{Adj}=0.46$) and SD ($p<0.02$, $R^2_{Adj}=0.29$). There were no significant variables at the inferior endplate for CT without separation by level.

Paired t-test results indicated that the mean values of average, standard deviation, coefficient of variation and kurtosis of endplate topography distributions measured from μ CT images are significantly different between superior and inferior endplates. Average and Kurtosis were significantly higher at the superior endplate, while standard deviation and coefficient of variation were lower.

Table 1: Statistical results comparing μ CT to DTS and HRCT topography measurements at superior and inferior endplates. All significant parameters had positive correlations. If a model was rerun with a non-significant interaction term removed and both level and variable were significant, the model was rerun without level (signified as *Variable). In the case of a significant interaction, if all 4 levels were separated by level and found to be significant and positive, levels were pooled in a unified mixed model (signified as **Variable).

	Comparison		Result
	Y	vs X	
Superior	mCT_AV	DTS_AV	$p < 0.0001$, $R^2_{Adj} = 0.21$
	mCT_SD	DTS_SD	** $p < 0.0001$, $R^2_{Adj} = 0.27$
	mCT_CV	DTS_CV	* $p < 0.0001$, $R^2_{Adj} = 0.17$
	mCT_Skew	DTS_Skew	** $p < 0.0001$, $R^2_{Adj} = 0.53$
	mCT_Kurt	DTS_Kurt	$p < 0.0001$, $R^2_{Adj} = 0.25$
	mCT_AV	HRCT_AV	$p < 0.0001$, $R^2_{Adj} = 0.37$
	mCT_SD	HRCT_SD	* $p < 0.0001$, $R^2_{Adj} = 0.19$
	mCT_CV	HRCT_CV	$p < 0.0001$, $R^2_{Adj} = 0.41$
	mCT_Skew	HRCT_Skew	$p = 0.0014$, $R^2_{Adj} = 0.58$
	mCT_Kurt	HRCT_Kurt	$p = 0.0006$, $R^2_{Adj} = 0.41$
Inferior	mCT_AV	DTS_AV	$p < 0.0001$, $R^2_{Adj} = 0.46$)
	mCT_SD	DTS_SD	$p = 0.0136$, $R^2_{Adj} = 0.29$)
	mCT_CV	DTS_CV	N.S.
	mCT_Skew	DTS_Skew	N.S.
	mCT_Kurt	DTS_Kurt	* $p = 0.0174$, $R^2_{Adj} = 0.03$
	mCT_AV	HRCT_AV	T10 ($p = 0.0034$, $R^2_{Adj} = 0.23$), T11 ($p < 0.0001$, $R^2_{Adj} = 0.23$), T12 ($p = 0.0297$, $R^2_{Adj} = 0.15$)
	mCT_SD	HRCT_SD	N.S.
	mCT_CV	HRCT_CV	N.S.
	mCT_Skew	HRCT_Skew	N.S.
	mCT_Kurt	HRCT_Kurt	N.S.

Table 2: Paired t-test results comparing statistical distribution parameters between superior and inferior endplates in μ CT images. Average parameters for superior and inferior endplate are presented as \pm standard deviation.

Parameter	p-value	Superior Endplate	Inferior Endplate
AV (mm)	<0.0001	3.832 ± 1.367	2.956 ± 1.148
SD (mm)	<0.0001	1.205 ± 0.523	1.891 ± 0.908
CV	<0.0001	0.323 ± 0.086	0.734 ± 0.535
Skew	0.4358	-0.598 ± 0.589	-0.664 ± 1.022
Kurt	<0.0001	3.428 ± 1.288	2.226 ± 0.898

IV. DISCUSSION

To our knowledge, this is the first study to demonstrate the ability to measure vertebral endplate topography using clinical imaging modalities. The authors successfully prepared DTS and HRCT images for analysis, performed voxel-based endplate topography measurements, and analyzed the topographical distribution for comparison with similar measurements taken from μ CT.

The level of success was promising, in that both tested modalities showed statistically significant correlations with μ CT approaching a moderate level of agreement at the superior endplate for all measured parameters ($R^2_{Adj}=0.17-0.58$). However, at the inferior endplate, average and standard deviation were moderately correlated while higher order statistical moments such as skewness and kurtosis were not significantly correlated with μ CT.

The lack of ability to measure higher order statistical distribution parameters at the inferior endplate may be explained as a function of measurement resolution. Kurtosis of a topography distribution gives a measure of its sharpness and is defined by the presence of outliers. For example, analysis of a relatively flat endplate with a small number of deep valleys would yield a low kurtosis, while an endplate with a high sloped rim would yield a higher kurtosis. Likewise, characteristic features such as a high remnant of a posterior element or a bony spur are captured by higher order statistical distribution parameters. If measurement resolution is poor and unable to detect such outliers, measurement of values such as kurtosis and skewness would be grossly affected.

Paired t-tests indicated that average depth from the reference plane was significantly greater at the superior endplate. Provided that DTS has more than seven times lower measurement resolution than μ CT, ability to measure sharpness of the topography distribution will be potentially largely affected by average depth. With a greater average depth, there are more steps available at a given voxel size to define the characteristic features contributing to changes in higher order statistical parameters. Interestingly, while all measured parameters *in both modalities* were significantly correlated with μ CT at the superior endplate, only DTS parameters were significantly correlated with μ CT at the inferior endplate. This is consistent with the fact that CT has considerably poorer resolution in the measurement direction, approximately half that of DTS (superior-inferior pixel size of 0.75 mm vs 0.3 mm). The HRCT images used in this study were reconstructed using a high resolution protocol and typical musculoskeletal CT scans (slice thickness 1-3 mm) would yield a greater discrepancy in results.

The use of clinical imaging modalities, specifically DTS, is encouraging and should be explored further. We intend to look for options to enhance precision of endplate topography measurement in tomosynthesis. As mentioned previously, one unavoidable artifact in DTS imaging is the blurring of the lowest and highest slices in the acquisition, which limits analysis to a central slab of well-resolved slices. In this sense, the full vertebral endplate was not analyzed in the DTS image. Only lateral-medial acquisitions were assessed in this study. The extent to which anterior-posterior acquisitions can improve the correlations to μ CT results remains to be determined.

V. CONCLUSION

In this study, moderate correlations were found between μ CT and the two tested clinical imaging modalities (DTS and HRCT) at the superior endplate for five parameters (average, standard deviation, coefficient of variation, kurtosis, and skewness) derived from endplate topography measurements. In the statistical model, only DTS scans produced significant but poor to moderate correlations with μ CT at the inferior endplate for several parameters. Lack of correlation between μ CT and HRCT at the inferior endplate is likely due to a combination of poor resolution and a lack of characteristic deep features which higher order statistics would identify.

One of the goals of this study was to seek out a scanning modality safe for clinical use (limited radiation dosage), while maintaining high resolution images from which endplate surface topography measurements can be made. It was hypothesized that DTS, with approximately 1/5 the radiation dose and greater in-plane resolution than CT, would be an ideal clinical imaging modality for assessing endplate topography, which has been shown in μ CT studies to correlate

with mechanical parameters related to bone fragility. As measurements taken from DTS produced poor correlation with comparable measurements from μ CT (considered the gold standard for scanning), we conclude that further studies are warranted before employing DTS scans in a clinical setting for the purpose of endplate analysis.

Several limitations of the present study have been presented. Manual selection of threshold values produced visually acceptable segmentation, however methods may be refined to use adaptive thresholding techniques in order to optimize characterization of the endplate surface. In addition, including anterior-posterior scans in statistical models could provide missing information due to scanning limitations in a single direction.

This study demonstrated the ability to process DTS and HRCT images for the purpose of performing endplate topography measurements. Results are encouraging and point to the importance of continued investigation.

WORKED CITED

1. Buie HR, Campbell GM, Klinck RJ, MacNeil JA, Boyd SK. Automatic segmentation of cortical and trabecular compartments based on a dual threshold technique for in vivo micro-CT bone analysis. *Bone* 2007; 41(4):505-15.
2. Cheng XG, Nicholson PH, Boonen S, Lowet G, Brys P, Aerssens J, Van der Perre G, Dequeker J. Prediction of vertebral strength in vitro by spinal bone densitometry and calcaneal ultrasound. *Journal of Bone and Mineral Research* 1997; 12(10):1721–8.
3. Cranney A, Jamal SA, Tsang JF, Josse RG, Leslie WD. Low bone mineral density and fracture burden in postmenopausal women. *Canadian Medical Association Journal* 2007; 177(6): 575-580.
4. Eswaran SK, Gupta A, Keaveny TM. Locations of bone tissue at high risk of initial failure during compressive loading of the human vertebral body. *Bone* 2007; 41:733–9.
5. Hovis, D. Personal correspondence [email; July 22, 2013].
6. Kim W, Oravec D, Sander E, Divine GW. Digital Tomosynthesis-Derived Microstructural Parameters Predict Cancellous Bone Stiffness in Human Vertebrae. *Proceedings of the 59th Annual Meeting of the Orthopaedic Research Society*, San Antonio, TX. p. 0701.
7. Langrana NA, Kale SP, Edwards WT, Lee CK, Kopacz KJ. Measurements and analyses of the effects of adjacent end plate curvatures on vertebral stresses. *The Spine Journal* 2006;6(3):267–78.
8. Lindsay R, Pack S, Li Z. Longitudinal progression of fracture prevalence through a population of postmenopausal women with osteoporosis. *Osteoporos Int* 2005; 16(3):306-312.

9. Nekkanty, S., Divine, G. W., Flynn, M. J., and Yeni, Y. N. Digital Tomosynthesis-Based Textural Measures Predict Vertebral Strength. Proceedings of the 57th Annual Meeting of the Orthopaedic Research Society, 2011, Long Beach, CA. p. 670.
10. Nekkanty S, Yerramshetty J, Kim DG, Zael R, Johnson E, Cody DD, Yeni YN. Stiffness of the endplate boundary layer and endplate surface topography are associated with brittleness of human whole vertebral bodies. Bone 2010; 47(4):783-9.
11. Oravec DJ, Zael RR, Yeni YN. The role of endplates in strain distributions and microstructural organization within the vertebral shell and cancellous centrum of a rat T5 vertebra during loading. Proceedings of the 58th Annual Meeting of the Orthopaedic Research Society, 2012, San Francisco, California, p. 1142.
12. Rasband, WS, ImageJ, U. S. National Institutes of Health, Bethesda, Maryland, USA, <http://imagej.nih.gov/ij/>, 1997-2013.
13. Reimann DA, Hames SM, Flynn MJ, Fyhrie DP. A Cone Beam Computed Tomography System for True 3D Imaging of Specimens. Applied Radiation and Isotopes 1997; 48(10–12):1433–1436.
14. Singer K, Edmondston S, Day R, Breidahl P, Price R. Prediction of thoracic and lumbar vertebral body compressive strength: correlations with bone mineral density and vertebral region. Bone 1995; 17:167–74.
15. Thornton MM, Flynn MJ. Measurement of the spatial resolution of a clinical volumetric computed tomography scanner using a sphere phantom. Proceedings of SPIE, 2006. V.6142.
16. Zael R, Fyhrie DP, Yeni YN. Segmentation Algorithm With Improved Connectivity For Accurate 3D Representation Of Microcomputed Tomographic Images Of Human

Vertebral Bodies. Proceedings of the 51st Annual Meeting of the Orthopaedic Research Society, 2005, Washington, DC. p. 1260

2013 Siemens Competition

Math : Science : Technology

Qualification Questions for Vertebrate Animals/Human Subjects Form

(Form must be completed by the student(s). Please save to your hard drive, type in answers and print.
Make three copies and attach one to each copy of your Research Project.)

The Siemens Competition recognizes that laboratory research using animals and/or human subjects has led to important discoveries. Because this is a high school competition, however, the program has set guidelines as to what is and is not allowable for purposes of entering this competition. Students must understand and follow the competition guidelines **for Human Subjects and Other Vertebrate**.

If your research project uses human subjects or other vertebrates, you must respond to the questions below. Your response provides you an opportunity to describe your use of vertebrates to the judges. Like the Research Report, the responses should be written by the student(s) and **no** student names or reference to gender ("he" or "she"), high schools, school officials, advisors, mentors, affiliated research organizations, or acknowledgements of the entrants are to appear anywhere in the answers below.

1. Why was it necessary for you to use live animals and/or humans or fluids, cells, tissues, or organs from vertebrates in your research? Justify the species used.
Vertebrates were needed to compare results from 3 different scanning modalities - CT, DTS, and μ CT. Human cadaveric thoraco-lumbar spines were acquired under local IRB approval from tissue banks, and four vertebral bodies (T10, T11, T12, L1) were harvested from 42 donors of varying gender and age.
2. Describe how you used the animals and/or humans in the research. Further, describe whether the animals were euthanized before or after your experiments and for what purpose.
Human cadaveric thoraco-lumbar spines were acquired under local IRB approval from tissue banks, and then scanned using three scanning mechanisms: CT, DTS, and μ CT. No animal vertebrates were used.

Introduction: Clinical modalities currently available for the assessment of fracture risk in the spine largely rely on bone mineral density (BMD) measurements; however, their ability to provide information on the trabecular structure is limited. Digital tomosynthesis (DTS) is a relatively new imaging modality that has several advantages over the conventional CT and radiography, where DTS can generate stack images of a vertebra with an in-plane resolution superior to that of CT but with only 1/5th of the radiation. It has been recently reported that fractal dimension (FD), mean intercept length (MIL) and line fraction deviation (LFD [1]) parameters obtained from DTS images of human vertebrae are correlated to 3D microstructure and stiffness of trabecular bone as determined from microcomputed tomography (μ CT) [2, 3]. These correlations were achieved by using a single image slice selected at the center of a DTS stack (20 to 50 slices). The scan geometry was such that the movement of the x-ray source and the detector were transverse to the axis of the vertebra and DTS images were acquired in an anteroposterior (AP) view (resulting in a stack of coronal images). The objective of the current study was to investigate the extent to which scan orientation (transverse, parallel or oblique to the vertebral axis) and view (AP or lateral) affect the prediction of trabecular bone stiffness, independent from bone volume fraction. The results are expected to enable informed decisions about patient positioning during translation of DTS to in vivo applications.

Methods: Thoracic 6, T8, T11, and L3 vertebrae from 5 female and 5 male cadavers (age 63-90yr) were μ CT scanned and reconstructed at 45 μ m voxel size. In each trabecular bone region, mean bone volume fraction (BV/TV) was obtained. Cancellous bone apparent modulus (E_{FE}) was calculated from a finite element (FE) simulation of inferior-superior compression using heterogeneous material moduli scaled with μ CT gray levels [2]. The same bones were scanned using DTS (Shimadzu Sonialvision Safire II) in the AP (producing a stack of coronal plane images) and lateral (LM, producing a stack of sagittal plane images) views while aligned axially (0°), transversely (90°) or obliquely (23°) to the superior-inferior axis of the vertebrae (a total of 6 scans per spine). The vertebrae were immersed in water during scans to simulate soft tissue.

A cuboidal volume of interest was cropped out of each reconstructed DTS image-stack to include as much cancellous bone as possible, similar to the volumes of interests (VOIs) from the μ CT images used for the FE analysis (Fig. 1). Each cropped region was analyzed using the fractal, MIL and LFD methods. In fractal analysis, fractal dimension (FD), mean lacunarity (λ) and the slope of lacunarity vs. box size relationship (S_λ) were calculated [4, 5]. In MIL and LFD analyses, the mean (A_v), standard deviation (SD), maximum (Max) and degree of anisotropy (DA, ratio of the principal measurements of MIL or LFD) were recorded for each slice (Fig 2). The central slice from each stack was also analyzed separately for a comparison between the 2D and 3D approaches.

Stepwise forward regression method was used to construct mixed multiple regression models that examined the relationship of fractal, MIL and LFD parameters with E_{FE} . In all regression models, a subject variable was included as a random effect to account for pseudo-replication. BV/TV was introduced first and forced to stay in the model in order to examine the effect of DTS independently from bone mass. A separate analysis was performed for each scan configuration. Models with high multicollinearity (Variance Inflation Factor ≥ 5) were rejected.

Results: The models constructed using DTS parameters only (without BV/TV) ranged from nonsignificant to an explanatory capability (R^2_{adj}) of 0.89, with only the LM-oblique ($R^2_{adj}=0.85$) and the LM-transverse ($R^2_{adj}=0.89$) cases reaching a value above that is explained by BV/TV alone ($R^2_{adj}=0.82$). When BV/TV was present, all scan configurations provided parameters that increased the explained variability (R^2_{adj}) in cancellous bone stiffness over that is explained by BV/TV (Table 1). An exception is the oblique scans in the lateral view in which case the DTS parameters were either nonsignificant (central slice) or did not improve R^2_{adj} compared to BV/TV alone. Models from transverse scans and the LM view appeared to perform better than those from the other configurations. Parameters related to cancellous bone anisotropy ($A_v(MIL.DA)$ or, similarly, $A_v(MIL.SD)$) were persistently present in the models from axial and transverse scans. When improvement in R^2_{adj} was observed compared to the single-slice case, the model included a term representing the slice-to-slice heterogeneity of the microstructure.

Discussion: By using the entire image stack, we were able to calculate parameters that represent the 3D heterogeneity of the microstructure. Most explanatory models of stiffness had one or more of these heterogeneity parameters, demonstrating a major advantage of DTS over 2D projection methods. A predictor set that contains BV/TV, a measure of anisotropy and a measure of heterogeneity is consistent with results from laboratory-scale high resolution imaging studies (μ CT) [6]. Overall, the results are encouraging for further development of bone assessment tools using DTS.

The most explanatory model from each scan configuration included different predictor parameters. Different parts of the cancellous bone in the analysis volume and the dependence of DTS resolution on the orientation of structural features relative to the scan orientation [7] may explain these differences. The findings that DTS parameters derived from the LM views could outperform BV/TV in predicting bone stiffness and that the transverse scans from the LM view resulted in more explanatory models in the presence of BV/TV suggest that the transverse orientation in the LM view is the preferred configuration for the best assessment of cancellous bone if a single DTS scan is to be considered. However, it is likely that scans in additional orientations or views will provide information complementary to that from the LM-transverse scan and increase prediction accuracy for the fracture risk of a whole vertebra under a more complex loading than uniaxial compression.

It is not feasible in the current Safire system to position a human subject with a tilt more than 23 with respect to the scan table. However, a multi-orientation DTS scan with high resolution can be obtained (without sacrificing the low-radiation advantage) using a cone-beam system in a limited angle tomography with appropriate modifications to acquisition and reconstruction protocols. Current efforts are devoted to realization of such modifications.

Significance: DTS generated image stacks analyzed by fractal, MIL and LFD methods provided good to excellent predictions of in vitro vertebral trabecular bone stiffness, independent from bone mass. An orientation perpendicular to the axis of the spine in an LM view is the preferred configuration if a single scan is to be considered. Complementary microstructural information can be obtained by scanning in multiple orientations. Further development for a multidirectional DTS is feasible and may be necessary.

Acknowledgements: DOD PRMRP W81XWH-11-1-0769 and NIH AR059329.

References: [1] Geraets, W. 1998, Bone, 23(4): p. 383-8. [2] Nekkanty et al., 2011, 57th ORS, p. 670. [3] Kim et al., 2013, 59th ORS, 0701. [4] Fazzalari and Parkinson (1996). J Pathol 178(1): 100-5. [5] Plotnick et al. (1996). Phys Rev E Stat Phys Plasmas Fluids Relat Interdiscip Topics 53(5): 5461-8. [6] Yeni et al, 2011, Bone, 49: 886-94. [7] Notohara et al, 2009, Proc. SPIE 7258.

Table 1 - Summary of the most explanatory mixed multiple regression models ($E = BV/TV + DTS$) for each scan and analysis combination. Each cell shows R^2_{adj} followed by the predictor(s) in the model (p-value). Only those with $p < 0.05$ are shown. BV/TV is present in all models ($p < 0.0001$) and therefore not shown on the predictor list for clarity.

		Single central slice (1 slice / bone)	3D image stack (15-49 slices / bone)
AP (Anterior-posterior coronal plane)	Oblique (23°)	0.86 $S_{\lambda} (< 0.02)$	0.87 Mean FD (< 0.008) SD (MIL.SD) (< 0.04)
	Axial (0°)	0.88 MIL.DA (< 0.002) $S_{\lambda} (0.0328)$	0.85 SD (S_{λ}) (< 0.02)
	Transverse (90°)	0.87 MIL.DA (< 0.002)	0.90 Mean (MIL.DA) (< 0.0001)
LM (Lateral-medial sagittal plane)	Oblique (23°)	NS	0.83 SD (MIL.DA) (0.01) SD (FD) (< 0.005)
	Axial (0°)	0.84 MIL.DA (< 0.03)	0.88 Mean (MIL.DA) (< 0.0002)
	Transverse (90°)	0.90 LFD.Av (< 0.002) MIL.DA (< 0.0001)	0.94 Mean (MIL.SD) (< 0.0001) SD (LFD.SD) (< 0.03) SD (λ) (< 0.005) SD (FD) (< 0.04)

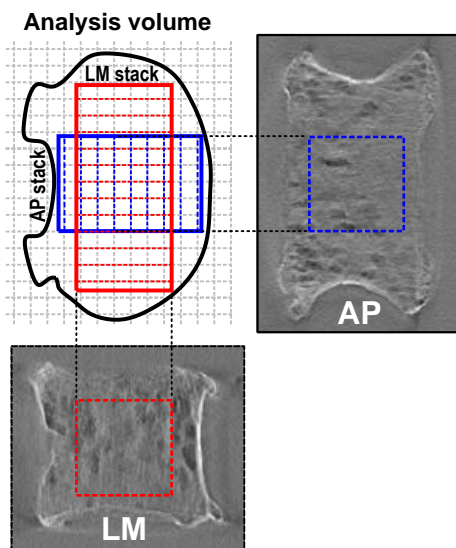


Figure 1 – Illustration of AP and LM VOIs in a vertebra. The red and the blue lines represent the image stacks for the LM and the AP view, respectively.

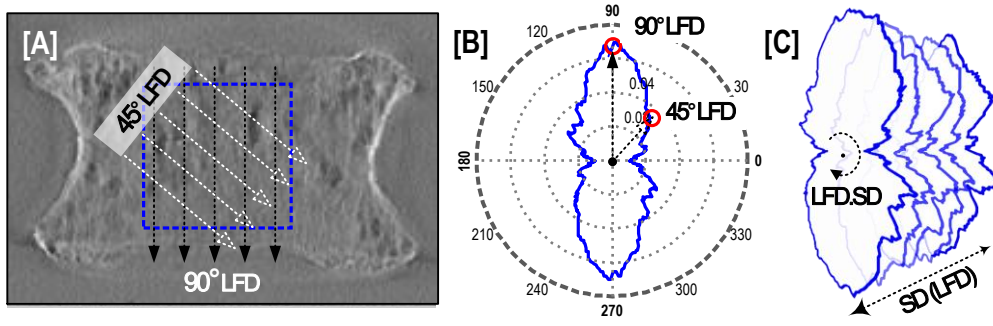


Figure 2 - [A] A square region cropped out of the DTS image is analyzed using the fractal, MIL and LFD analysis methods. MIL and LFD are calculated in all directions in the image. [B] A typical polar plot representation of the LFD data, from which an average, standard deviation, max and anisotropy (LFD at 90° / LFD at 0°) can be calculated for each slice. [C] Each slice in the stack is analyzed. Stack average and standard deviation (e.g. SD (LFD.SD)) are calculated as measures of 3D microstructure within the bone.

Digital Tomosynthesis for Prediction of Human Whole Vertebral Stiffness

Kim, Woong; Oravec, Daniel; Maatman, Thomas; Divine, George W; Flynn, Michael J; Yeni, Yener N

Bone and Joint Center, Henry Ford Hospital, Detroit, MI, United States.

Introduction: Digital tomosynthesis (DTS) has been proposed as an imaging approach capable of providing information on cancellous bone microstructure and thus as a potential means for an accurate assessment of vertebral bone strength and fracture risk [1, 2]. Although associations of DTS derived parameters with cancellous bone stiffness have been demonstrated, the extent to which DTS parameters are associated with whole vertebral mechanical properties is unknown. The objective of the current study was to determine relationships of DTS derived cancellous bone and vertebral geometry properties with vertebral stiffness. Large scale finite element (FE) estimations of vertebral stiffness based on high resolution microcomputed tomography (μ CT) images are used as a nondestructively determined surrogate for vertebral strength due to strong correlations between vertebral stiffness and strength.

Methods: T6, T8, T11, and L3 vertebrae from 5 female and 5 male cadavers (age 63-90yr) were μ -CT scanned and reconstructed at 45 μ m voxel size. In each trabecular bone region, bone volume fraction (BV/TV) was obtained and stiffness of whole bone (S) was calculated from a finite element (FE) simulation of inferior-superior compression using procedures described previously [3, 4]. The same bones were scanned using DTS (Shimadzu Sonialvision Safire II) in anterior-posterior (AP, producing a stack of coronal plane images) and lateral-medial (LM, producing a stack of sagittal plane images) views while aligned axially (0°), transversely (90°) or obliquely (23°) to the superior-inferior axis of the vertebrae (a total of 6 scans per spine). The vertebrae were immersed in water during scans to simulate soft tissue.

The central slices from AP-transverse and LM-transverse (corresponding to coronal and sagittal views) were analyzed for the vertebral heights and widths (**Fig 1**). A cuboidal volume of interest (VOI) was cropped out of each reconstructed DTS image-stacks to include as much cancellous bone as possible (**Fig .2**). Each cropped region was analyzed using the fractal, mean intercept length (MIL) and line fraction deviation (LFD) methods as previously described [2]. In fractal analysis, fractal dimension (FD), mean lacunarity (λ) and the slope of lacunarity vs. box size relationship (S_λ) were calculated [5, 6]. In MIL and LFD analyses, the mean (A_v), standard deviation (SD), maximum (Max) and degree of anisotropy (DA, ratio of the principal measurements of MIL or LFD) were recorded for each slice (**Fig 3**).

Stepwise forward regression method was used to construct mixed multiple regression models that examined the relationship of fractal, MIL and LFD parameters with stiffness. In all regression models, a subject variable was included as a random effect to account for pseudo-replication. Separate analyses were performed to examine contribution of DTS derived cancellous bone parameters and geometry to stiffness with and without the presence of bone mass information. Each scan configuration was examined separately. Models with high multicollinearity (Variance Inflation Factor ≥ 5) were rejected.

Results: There were at least two DTS derived cancellous bone parameters for each scan configuration that had a univariate association with vertebral stiffness, stronger ($R^2_{adj} = 0.68-0.79$) than that between stiffness and BV/TV ($R^2_{adj} = 0.65$). Explained variability in stiffness was improved when cancellous bone parameters were used in multiple regression models (Table 1), with the axial scans in the LM view providing highest R^2_{adj} . Inclusion of BV/TV in the cancellous-only models improved R^2_{adj} for the models from transverse scans but not from other orientations. Addition of geometric information to cancellous-only models slightly improved the models from the oblique and axial scans but not from the transverse scans. The most explanatory DTS-only model (cancellous bone and vertebral geometry) was from axial scans in the LM view, reaching an R^2_{adj} value of 0.90. When both cancellous and geometry information were available from DTS, addition of BV/TV improved the models for transverse scans in the AP view only. In general, a measure of vertebral size (LM or AP width), a measure of trabecular anisotropy (MIL.DA or, similarly, MIL.SD) and a measure of trabecular heterogeneity (inter-planar SD parameters), all measured from DTS were present in models with highest R^2_{adj} .

Discussion: We have demonstrated that DTS derived cancellous bone microstructural and vertebral geometry parameters are strongly associated with whole vertebral stiffness. DTS alone was more explanatory for vertebral stiffness than BV/TV. An axial scan in the LM view appears to be the optimum configuration for a model of vertebral stiffness with the highest explanatory capability, if DTS is to be used alone. Addition of BV/TV did not improve the explanatory capability of the models in this case, suggesting that additional bone mass information may not be necessary when assessment of a whole vertebra is made using DTS in the LM-axial configuration.

Previous studies reported an association of cancellous bone stiffness and DTS derived cancellous bone microstructural parameters for the AP-transverse configuration [1, 2]. BV/TV is a strong predictor of cancellous bone stiffness and was present in the multiple regression models for cancellous bone stiffness. Consistent with the previous results from cancellous bone, models of whole vertebral stiffness from the AP-transverse configuration reached their highest R^2_{adj} when BV/TV was included in the model. It is possible then that cancellous bone can be assessed using DTS alone if scan configurations other than the AP-transverse are considered.

Previous results from laboratory-scale high resolution imaging studies (μ CT) suggested that cancellous bone microstructural heterogeneity is associated with cancellous bone stiffness, independent from average measures of microstructure [7]. By using the entire image stack, we were able to calculate parameters that represent the 3D heterogeneity of the microstructure. Most explanatory models of stiffness had one or more of these heterogeneity parameters, demonstrating a major advantage of DTS over imaging methods that quantify average properties.

The predictor variables were different in models from different scan configurations, suggesting that complementary information may be obtained from different scan configurations. This may be due to a sensitivity of DTS to the orientation of the scanned features relative to the orientation of the scans [8]. This feature may be developed in to a method to analyze the microstructure in selected orientations with DTS.

Significance: DTS generated images analyzed by fractal, MIL and LFD methods provided good to excellent predictions of in vitro vertebral whole bone stiffness. This can be further improved by the inclusion of vertebral width data in the model.

Acknowledgements: DOD PRMRP W81XWH-11-1-0769 and NIH AR059329.

References:

[1] Nekkanty et al., 2011, 57th ORS, p. 670. [2] Kim et al., 2013, 59th ORS, 0701. [3] Kim et al., 2006, J Biomech Eng, 128: 161. [4] Nekkanty et al., 2010, Bone 47: 783-9. [5] Fazzalari and Parkinson (1996). J Pathol 178(1): 100-105. [6] Plotnick et al. (1996). Phys Rev E Stat Phys Plasmas Fluids Relat Interdiscip Topics 53(5): 5461-5468. [7] Yeni et al, 2011, Bone, 49: 886-94. [8] Notohara et al, 2009, Proc. SPIE 7258.

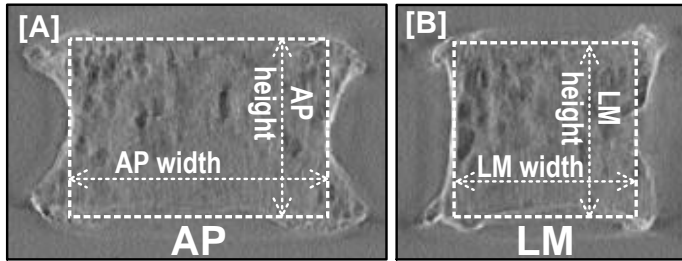


Figure 1 – Central slice from anterior-posterior (AP) coronal and lateral-medial (LM) sagittal scans were used to measure waist-to-waist width and endplate-to-endplate height.

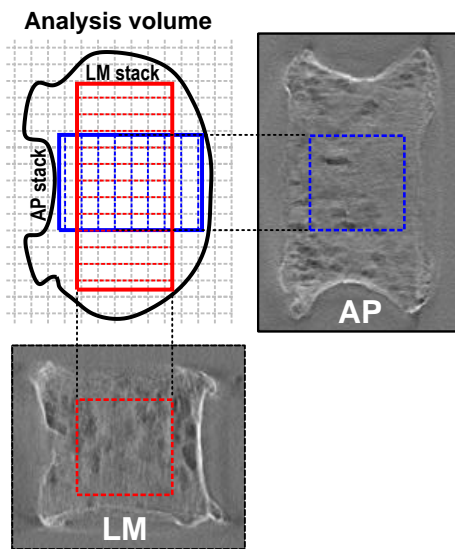


Figure 2 – Illustration of AP and LM VOIs in a vertebra. The red and the blue lines represent the image stacks for the LM and the AP view, respectively.

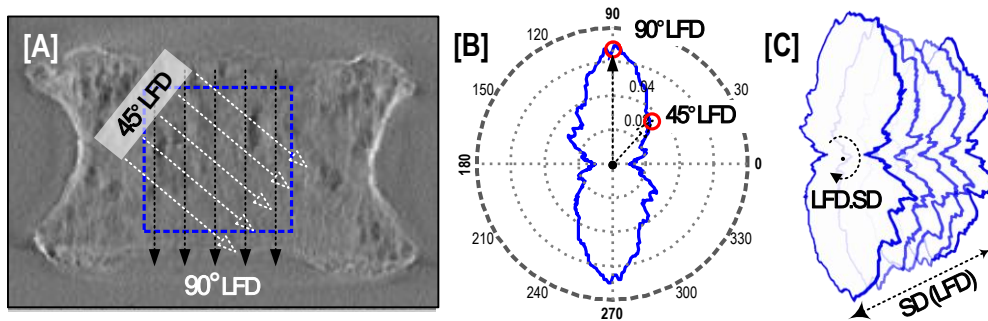


Figure 3 - [A] A square region cropped out of the DTS image is analyzed using the fractal, MIL and LFD analysis methods. MIL and LFD are calculated in all directions in the image. [B] A typical polar plot representation of the LFD data, from which an average, standard deviation, max and anisotropy (LFD at

90° / LFD at 0°) can be calculated for each slice. [C] Each slice in the stack is analyzed. Stack average and standard deviation (e.g. SD (LFD.SD)) are calculated as measures of 3D microstructure within the bone.

Table 1 - Summary of the most explanatory mixed multiple regression models for vertebral stiffness for each scan and analysis combination. Each cell shows R^2_{adj} followed by the predictor(s) in the model (p-value). Only those with $p < 0.05$ are shown. BV/TV is not shown for clarity.

		DTS cancellous only	DTS only (cancellous + geometry)	DTS + BV/TV (without geometry)	DTS + BV/TV (with geometry)
AP (Anterior-posterior coronal plane)	Oblique (23°)	0.81 Av(FD) (<0.02) SD(LFD.SD) (<0.0002) Av(MIL.SD) (<0.0004) SD(MIL.Av) (<0.02) Av(MIL.DA) (<0.04)	0.84 AV(FD) (<0.04) SD(LFD.SD) (<0.0001) AP Height(<0.002) Av(MIL.Av) (<0.002) SD(MIL.Max) (<0.004)	0.79 Av(FD) (<0.004) SD(LFD.SD) (<0.0009) Av(MIL.SD) (<0.02)	0.84 AP Width (<0.0001) SD LFD.SD (<0.006)
	Axial (0°)	0.79 SD(S_x) (<0.0001)	0.79 SD(S_x) (<0.0001)	0.78 SD(S_x) (<0.0001)	0.82 AP Width (<0.007) SD(S_x) (<0.05)
	Transverse (90°)	0.82 Av(MIL.SD) (<0.0001) SD(MIL.DA) (<0.0002) Av(MIL.Av) (<0.002) SD(MIL.SD) (<0.03)	0.82 Av(MIL.SD) (<0.0001) SD(MIL.DA) (<0.0002) Av(MIL.Av) (<0.002) SD(MIL.SD) (<0.03)	0.89 Av(MIL.SD) (<0.0001) SD(MIL.DA) (<0.0001) Av(MIL.Av) (<0.0001) SD(MIL.SD) (<0.004)	0.91 Av(MIL.SD) (<0.002) SD(MIL.DA) (<0.0001) Av(MIL.Av) (<0.0004) AP Width (<0.009) SD(MIL.SD) (<0.02)
LM (Lateral-medial sagittal plane)	Oblique (23°)	0.76 SD(LFD.SD) (<0.002)	0.79 LM Width (<0.03) SD(LFD.SD) (<0.003)	0.77 SD(LFD.SD) (<0.0004)	0.85 LM Width (<0.0001) SD(LFD.SD) (<0.0003)
	Axial (0°)	0.88 Av(FD) (<0.0002) SD(LFD.SD) (<0.0001) Av(MIL.SD) (<0.0001) Av(MIL.DA) (<0.002) SD(MIL.Av) (<0.004)	0.90 Av(FD) (<0.0001) SD(LFD.SD) (<0.0001) Av(MIL.SD) (<0.0001) Av(MIL.DA) (<0.005) SD(MIL.Max) (<0.008) LM Width (<0.007)	0.83 Mean (S_x) (<0.004) SD(LFD.SD) (<0.0004)	0.83 LM Width (<0.006) SD(LFD.Max) (<0.007) Av (S_x) (<0.05)
	Transverse (90°)	0.70 Av(MIL.SD) (<0.02)	0.70 Av(MIL.SD) (<0.02)	0.75 Av(MIL.SD) (<0.006)	0.76 LM Width (<0.0001)

		DTS cancellous only	DTS only (cancellous + geometry)	DTS + BV/TV (without geometry)	DTS + BV/TV (with geometry)
AP (Anterior-posterior coronal plane)	Oblique (23°)	0.81 Av(FD) (<0.02) SD(LFD.SD) (<0.0002) Av(MIL.SD) (<0.0004) SD(MIL.Av) (<0.02) Av(MIL.DA) (<0.04)	0.84 AV(FD) (<0.04) SD(LFD.SD) (<0.0001) AP Height(<0.002) Av(MIL.Av) (<0.002) SD(MIL.Max) (<0.004)	0.79 Av(FD) (<0.004) SD(LFD.SD) (<0.0009) Av(MIL.SD) (<0.02)	0.84 AP Width (<0.0001) SD LFD.SD (<0.006)
	Axial (0°)	0.79 SD(S _z) (<0.0001)	0.79 SD(S _z) (<0.0001)	0.78 SD(S _z) (<0.0001)	0.82 AP Width (<0.007) SD(S _z) (<0.05)
	Transverse (90°)	0.82 Av(MIL.SD) (<0.0001) SD(MIL.DA) (<0.0002) Av(MIL.Av) (<0.002) SD(MIL.SD) (<0.03)	0.82 Av(MIL.SD) (<0.0001) SD(MIL.DA) (<0.0002) Av(MIL.Av) (<0.002) SD(MIL.SD) (<0.03)	0.89 Av(MIL.SD) (<0.0001) SD(MIL.DA) (<0.0001) Av(MIL.Av) (<0.0001) SD(MIL.SD) (<0.004)	0.91 Av(MIL.SD) (<0.002) SD(MIL.DA) (<0.0001) Av(MIL.Av) (<0.0004) AP Width (<0.009) SD(MIL.SD) (<0.02)
LM (Lateral-medial sagittal plane)	Oblique (23°)	0.76 SD(LFD.SD) (<0.002)	0.79 LM Width (<0.03) SD(LFD.SD) (<0.003)	0.77 SD(LFD.SD) (<0.0004)	0.85 LM Width (<0.0001) SD(LFD.SD) (<0.0003)
	Axial (0°)	0.88 Av(FD) (<0.0002) SD(LFD.SD) (<0.0001) Av(MIL.SD) (<0.0001) Av(MIL.DA) (<0.002) SD(MIL.Av) (<0.004)	0.90 Av(FD) (<0.0001) SD(LFD.SD) (<0.0001) Av(MIL.SD) (<0.0001) Av(MIL.DA) (<0.005) SD(MIL.Max) (<0.008) LM Width (<0.007)	0.83 Mean (S _z) (<0.004) SD(LFD.SD) (<0.0004)	0.83 LM Width (<0.006) SD(LFD.Max) (<0.007) Av (S _z) (<0.05)
	Transverse (90°)	0.70 Av(MIL.SD) (<0.02)	0.70 Av(MIL.SD) (<0.02)	0.75 Av(MIL.SD) (<0.006)	0.76 LM Width (<0.0001)